

CHARACTERIZATION OF ACTIN-BASED MOTILITY ON MODIFIED SURFACES FOR
IN VITRO APPLICATIONS IN NANODEVICES

By

KIMBERLY A. INTERLIGGI

A DISSERTATION PRESENTED TO THE GRADUATE SCHOOL
OF THE UNIVERSITY OF FLORIDA IN PARTIAL FULFILLMENT
OF THE REQUIREMENTS FOR THE DEGREE OF
DOCTOR OF PHILOSOPHY

UNIVERSITY OF FLORIDA

2007

© 2007 Kimberly A. Interliggi

To my encouraging parents, Denni and Vicki Interliggi,
my siblings, Jen and Tom, and my boyfriend, Matt Crim,
for their continued support.

ACKNOWLEDGMENTS

I thank my advisor, Dr. Richard B. Dickinson, for his support over the past four years. His guidance and encouragement have helped me succeed in many aspects of my graduate experience. I appreciate Dr. Yiider Tseng for always expressing his interest in my research and career and encouraging me along the way. I thank Dr. Spyros Svoronos for his dedication as a committee member. I acknowledge Dr. Anuj Chauhan for his guidance and helpful advice from the very beginning of my graduate career. I also thank Dr. Jennifer Curtis for her dedication to the graduate students in this department. Finally, I acknowledge the faculty and staff in the Department of Chemical Engineering for continuously supporting my efforts in many aspects of my graduate school career.

I am grateful to have had the opportunity to work with Dr. Daniel Purich in the Department of Biochemistry. Dr. Purich was involved on a daily basis with my lab work and was constantly teaching me new skills and sharing new ideas with me. I also thank Dr. William Zeile, who taught me many experimental and research techniques, and was always willing to listen to my research problems and help me work through them. Dr. Joseph Phillips and Dr. Fangliang Zhang are greatly appreciated for their companionship and knowledge in the lab. I also thank Dr. Suzanne Ciftan-Hens and Dr. Gary McGuire at International Technology Center in Raleigh, NC for their collaboration on this project.

I thank Dr. Adam Feinberg, who was instrumental in helping me start my project. I thank the members of my group, who were consistently helping me to understand and work through daily problems and always provided good company: Dr. Luzelena Caro, Dr. Colin Sturm, Gaurav Misra, Dr. Jeff Sharp, Dr. Huilian Ma, and Adam Wulkan. I also thank Andre Baran for his assistance and constant support.

TABLE OF CONTENTS

	<u>page</u>
ACKNOWLEDGMENTS	4
LIST OF FIGURES	8
LIST OF ABBREVIATIONS.....	11
ABSTRACT.....	12
CHAPTER	
1 INTRODUCTION.....	14
1.1 Actin.....	15
1.1.1 Filament Growth	15
1.1.2 Actomyosin	16
1.1.3 Actin-Associated Proteins.....	17
1.2 Experimental Methods for Actin Polymerization on Modified Substrata	18
1.2.1 Total Internal Reflection Fluorescence Microscopy	18
1.2.2 Microcontact Printing	21
1.3 Actin-Based Motility.....	22
1.3.1 <i>Listeria</i> and Particle Motility	22
1.3.2 Mechanisms	25
1.4 Bionanodevices	26
1.4.1 Sliding Filament Assay	27
1.4.2 Immobilized Filament Assay	28
1.4.3 Material Transport.....	29
2 GUIDANCE OF ACTIN FILAMENT ELONGATION ON FILAMENT-BINDING TRACKS.....	32
2.1 Introduction.....	32
2.2 Materials and Methods.....	32
2.2.1 Protein Preparation.....	32
2.2.2 Microcontact Printing	34
2.2.3 Actin Polymerization	35
2.2.4 TIRF Microscopy and Data Analysis.....	36
2.3 Results.....	38
2.3.1 Filament Binding to Stamped Surfaces.....	38
2.3.2 Alignment of Filaments.....	39
2.3.3 NEM-Myosin Concentration.....	41
2.3.4 Control of Actin Polymerization.....	42
2.4 Discussion	43
2.4.1 Mechanism for Filament Alignment	43
2.4.2 Potential and Applications	45

3	SIMULATING ACTIN FILAMENT ELONGATION ON MODIFIED SURFACES	63
3.1	Introduction	63
3.2	Methodology	63
3.3	Results	66
3.3.1	Description of Simulated Filament Elongation	66
3.3.2	Probability of Filament Rebinding	67
3.3.3	Alignment of Filaments	70
3.4	Discussion	71
4	ACTIN-BASED MOTILITY OF LISTERIA AND PARTICLES ON MODIFIED SURFACES	86
4.1	Introduction	86
4.2	Materials and Methods	86
4.2.1	<i>Listeria monocytogenes</i> Growth and Protein Purification	86
4.2.2	Bead Preparation	88
4.2.3	Motility Assay	89
4.2.4	Fabrication of Channel Devices	89
4.2.5	Microscopy and Analysis	90
4.3	Results	91
4.3.1	Confining Particle Propulsion to the Surface	91
4.3.2	Effectiveness of NEM-Myosin Surfaces	92
4.3.3	Particle Velocity and Tail Characterization	93
4.3.4	Guiding Particle Propulsion	95
4.4	Discussion	96
4.4.1	Mechanics of Actin Rocket Tails on Surfaces	96
4.4.2	Biochemical Considerations	97
4.4.3	Considerations for Bionanotechnology	98
5	SINGLE FILAMENT ACTIN-BASED MOTILITY OF PARTICLES	113
5.1	Introduction	113
5.2	Materials and Methods	114
5.2.1	Protein Preparations	114
5.2.2	Bead Functionalization	114
5.2.3	Motility Assays	115
5.2.3.1	Attached beads	115
5.2.3.2	NEM-myosin surfaces	116
5.2.4	Microscopy and Analysis	116
5.3	Results	116
5.3.1	Actin Asters	116
5.3.2	Single Actin Filaments	118
5.4	Discussion	119

6	SUMMARY AND FUTURE WORK	133
6.1	Single Actin Filaments	133
6.2	Actin-Based Motility	135
6.3	Recommendation for Future Work	136
6.3.1	Filament-Binding Tracks	136
6.3.2	Three-Dimensional Surfaces for Larger Structures	137
6.3.2	Use of End-Tracking Motors	138
	APPENDIX: MATLAB CODE	140
	LIST OF REFERENCES	145
	BIOGRAPHICAL SKETCH	154

LIST OF FIGURES

<u>Figure</u>	<u>page</u>
1-1 Treadmilling of an actin filament	30
1-2 Experimental set-up for binding filaments to a surface.....	30
1-3 Schematic of microcontact printing protein on glass.....	31
2-1 Images of microcontact-printed myosin tracks on a glass coverslip	47
2-2 Time-lapse image of actin filaments on a BSA-stamped surface.....	48
2-3 Total internal reflection fluorescence microscopy images of elongating actin filaments on NEM-myosin tracks	49
2-4 Filaments in BSA region undergo large thermal undulations.....	49
2-5 Total internal reflection fluorescence microscopy images of undulating ends of elongating filaments.....	50
2-6 Filament elongating passed the track edge at small θ	50
2-7 Filament alignment as a function of filament density on tracks.....	51
2-8 Effect of track width on filament alignment.....	52
2-9 Histogram showing the fraction, f , of filament ends that rebind to tracks after their elongating ends cross track boundaries.....	54
2-10 Scatter plot showing each segment alignment with the track edge as a function of the distance from the track edge	55
2-11 Dependence of filament alignment and elongation rate on the concentration of NEM-myosin.....	56
2-12 Scatter plots showing the alignment of individual filament segments	57
2-13 Filaments accumulate in the BSA region of the stamped surface.	59
2-14 Incubation time of lyophilized rhodamine actin	59
2-15 Increasing the concentration of profilin visibly decreases the density of actin filaments on NEM-myosin treated surfaces.....	60
2-16 Elongation rate of actin filaments as a function of profilin concentration	61

2-17	Illustration of the likely mechanism for actin filament alignment on NEM-myosin tracks	62
3-1	The x- and y-positions of elongating filament ends as a function of time.....	75
3-2	Effect of change in length (step-size of simulation) on the filament rebinding probability	77
3-3	Effect of the number of modes on filament rebinding probability	78
3-4	Effect of total filament length on filament rebinding probability.....	79
3-5	Effect of binding probability constant, K_p ($\mu\text{m}^{-1}\times\text{sec}^{-1}$), on filament rebinding probability.....	80
3-6	Effect of persistence length on filament rebinding probability.	81
3-7	Effect of track width and number of modes on the alignment of filaments	82
3-8	Effect of track width and binding probability constant on the alignment of filaments	83
3-9	Effect of binding probability on the alignment of filaments.....	84
3-10	Effect of track width and persistence length on the alignment of filaments.....	85
4-1	<i>Listeria</i> and 500-nm diameter bead propelled by actin rocket tails.....	100
4-2	Rotation of a helical actin rocket tail in solution	100
4-3	<i>Listeria</i> rocket tails on NEM-myosin and BSA-treated surfaces.....	101
4-4	500-nm diameter beads attached to rocket tails bound on NEM-myosin and BSA-treated surfaces	101
4-5	Fields-of-view with large percentage of tails bound to surface.....	102
4-6	Fraction of actin rocket tails bound to NEM-myosin and BSA-treated surfaces.	103
4-7	Change in x- and y-position over time for beads on NEM-myosin and BSA surfaces ...	104
4-8	Helical actin rocket tail confined to NEM-myosin-treated surfaces.....	104
4-9	Actin rocket tails in total internal reflection fluorescence microscopy	105
4-10	Magnified image of actin rocket tail with protruding filaments.....	106
4-11	Actin tail elongation on NEM-myosin and BSA surfaces.....	107
4-12	Average tail elongation rates determined from the slope of a best-fit line.....	108

4-13	NEM-myosin surface effect on persistence of tail.....	109
4-14	Stamped surfaces with 500-nm diameter beads attached to actin tails.....	110
4-15	Actin tails bound to NEM-myosin-treated exposed glass of fabricated device.....	111
4-16	Actin rocket tail encounters CYTOP wall	112
5-1	Growth of actin filaments/bundles on 50-nm diameter beads	123
5-2	Fluorescent intensity of actin filaments/bundles.....	124
5-3	Actin asters recovery after photobleaching.....	125
5-4	Enlarged image of asters reappearing after photobleaching	126
5-5	Fluorescent intensity of photobleached filaments.....	127
5-6	Recovery rates and equilibrium intensities of photobleached filaments	128
5-7	50-nm diameter beads bound to surface with single filaments or bundles.....	130
5-8	50-nm diameter beads in solution on NEM-myosin surfaces.....	131
5-9	Actin motility assay with and without beads on NEM-myosin surfaces.....	132

LIST OF ABBREVIATIONS

ADF	Actin depolymerizing factor
ADP	Adenosine diphosphate
AFM	Atomic force microscopy
APES	3-aminopropyltriethoxysilane
Arp2/3	Actin related proteins 2/3
ATP	Adenosine triphosphate
BHI	Brain-heart infusion media
BS ³	Bis(sulfosuccinimidyl suberate)
BSA	Bovine serum albumin
DMSO	Dimethyl sulfoxide
DTT	Dithiothreitol
EDTA	Ethylenediamine tetraacetic acid
EGTA	Ethylene glycol tetraacetic acid
EM	Electron microscopy
HMM	Heavy meromyosin
NEM	N-ethylmaleimide
PDMS	Polydimethylsiloxane
PMSF	Phenylmethanesulphonyl fluoride
TIRF	Total internal reflection fluorescence
VASP	Vasodilator-stimulated phosphoprotein

Abstract of Dissertation Presented to the Graduate School
of the University of Florida in Partial Fulfillment of the
Requirements for the Degree of Doctor of Philosophy

CHARACTERIZATION OF ACTIN-BASED MOTILITY ON MODIFIED SURFACES FOR
IN VITRO APPLICATIONS IN NANODEVICES

By

Kimberly A. Interliggi

December 2007

Chair: Richard Dickinson
Major: Chemical Engineering

The cytoskeletal protein actin generates forces for various processes by polymerizing into filaments. *In vivo*, actin works with the motor protein myosin to produce muscle contractions and with proteins acting as end-tracking motors responsible for cell and bacterial motility, such as the motility of *Listeria monocytogenes*. End-tracking proteins bind the polymerizing end of an actin filament to a motile surface, creating persistent attachment during filament elongation. Both types of motors use the energy from ATP hydrolysis and can be exploited *in vitro* in bionanodevices, which require forces to transport objects on a micro- or nano-scale, possibly against flow or diffusion gradients.

Our study has focused on the guidance of single-filament elongation and filament bundles (rocket tails) to orient elongation *in vitro*. Microcontact printing, a technique that stamps protein patterns onto glass surfaces through adsorption, was used to create filament-binding tracks of modified myosin (void of its motor activity), which successfully bound and guided single actin filament elongation in a manner dependent on track width and surface conditions. These results confirm the capability of this method to be used for the motility of objects attached to single actin filaments and for the creation of immobilized tracks of actin filaments for myosin-mediated

transport. Simulations were used to characterize the system further and have the ability to help make predictions for other types of filaments and systems.

Modified myosin surfaces also confined actin rocket tails attached to particles and bacteria, reducing the Brownian motion of the motile objects. Channels formed through photolithographic techniques on glass surfaces were used to attempt to guide these particles. Single actin filaments attached to smaller particles were also characterized to determine the potential for single-filament propulsion in nanodevices. We conclude that actin filament-binding proteins can be applied to surfaces using adsorption and microcontact printing and that this technique is effective in binding and guiding filaments in various systems, including single and bundled filaments. We predict this technique can be applied to other systems undergoing actin-based motility, making it a versatile method for bionanotechnology.

CHAPTER 1 INTRODUCTION

Muscle contraction, cell movement, intracellular bacteria motility and cell division are all processes that involve biomolecular motors, a group of proteins that utilize the energy from adenosine triphosphate (ATP) hydrolysis to do work on a system (1). These biomolecular motors can be exploited for the *in vitro* transport of nano-cargo (e.g. beads, bacteria, DNA) (2-7), as well as in biosensors, microfluidic devices, and micro- and nanoelectromechanical systems (MEMS and NEMS) (8-15). One approach has been to pattern surface regions with a high-affinity for the adsorption of the molecular motors kinesin and myosin to guide transport of pre-assembled microtubules and actin filaments, respectively (8, 15-21). Other methods rely on surface-immobilized microtubules and actin filaments to create tracks for kinesin-mediated (3, 5, 22) and myosin-mediated particle transport (6, 23, 24).

Current research has been aimed toward understanding another type of biomolecular motor that couples force-producing, polymerizing filaments to a motile object (25-27). These motors, known as filament end-tracking proteins, are thought to take part in the formation of lamellapodia and filopodia during cell crawling, propulsion of bacteria, such as *Listeria monocytogenes* (28, 29), and chromosome separation during cell division (30). End-tracking motors provide a versatile mechanism for force generation *in vitro*, including the potential to be used as micro- and nano-scale actuators that can transport objects against obstacles, including opposing forces.

Both myosin and end-tracking motors provide many advantages to bionanotechnology. Nanofluidics is one method for high-throughput analysis of biological material, but due to the high surface to volume ratio, friction can cause significant losses. Molecular motor systems can transport material without flow, therefore eliminating friction losses (10, 31). Other applications

of biomolecular motors in nanodevices are broad and include biomaterials that no longer depend on equilibrium conditions for effectiveness (10), extremely sensitive and fast single-molecule detection (32), and nano-scale information storage and processing through surface-probing (33). Both surface modifications and biochemical parameters play a key role in the exploitation of biomolecular motors. We have focused on using suitably patterned surfaces to place and guide elongating actin filaments or bundles of filaments attached to particles.

1.1 Actin

Globular actin (G-actin), a 43,000 Da protein with a radius of 2.7 nm, is a cytoskeletal protein found in eukaryotic cells. It has a deep cleft for binding ATP or adenosine diphosphate (ADP) and an associated cation (Ca^{2+} or Mg^{2+}) (34-37). G-actin can polymerize into filaments (F-actin) under conditions of high ionic strength *in vitro*, producing a 7-nm diameter semi-flexible, double-helical filament with repeats every 37 nm (1, 38). Within the filament, actin monomers align with all of their clefts pointing in the same direction (toward the (-)-end). This asymmetrical orientation causes polarity in the filament, with a faster-polymerizing (+)-end and a slower polymerizing (-)-end.

1.1.1 Filament Growth

Actin polymerization includes a nucleation step, followed by filament elongation and treadmilling (39). Nucleation requires that three ATP-actin monomers come together to form a polymerization nuclei. *In vivo* and in cell extract systems, actin-related protein 2/3 (Arp2/3) complex has been experimentally confirmed to be located at the site of actin filament assembly and assumed to serve as a polymerization nuclei (40, 41). As its name implies, Arp2/3 has two subunits with similar structures to actin (42). Elongation occurs when ATP-actin monomers add to the filament (+)-end, followed by hydrolysis of the monomer-bound ATP molecule during or slightly after the addition of the next monomer, creating ADP- P_i -actin monomers within the

filament. The P_i is released, forming ADP-actin monomers near the (-)-end. The hydrolysis results in a (+)-end rich in ATP-actin and a (-)-end rich in ADP-actin (36). *In vitro*, the (+)-end has a lower critical concentration than the (-)-end (0.1 and 0.6 μM , respectively (43)), and when the concentration of free G-actin in solution is between these two values, a behavior known as treadmilling occurs (Figure 1-1). During treadmilling, the filament polymerizes at the (+)-end by the addition of ATP-G-actin and depolymerizes at the (-)-end. Once free from the filament (-)-end, ADP-actin releases its nucleotide and binds to ATP, replenishing the monomer pool for (+)-end elongation and starting the cycle over (44-46).

In vitro solutions of F-actin have been found to contain filaments with lengths of tens of microns (47). Filaments undergo Brownian motion in solution, which can be modeled based on filament length, L , and persistence length, λ , which is the characteristic length over which thermal undulations cause the filament orientation to be uncorrelated. For actin, λ has been found to be between approximately 10 and 20 μm , depending on the conditions (48, 49). Because λ and L are on the same length scale, F-actin is considered to be a semi-flexible polymer. The thermal motion of phalloidin-stabilized filaments has been quantitatively described by using the bending energy of a rod with both ends free and then performing a normal mode analysis of the bending excitations (49).

1.1.2 Actomyosin

The actin/myosin complex (actomyosin) is a type of biomolecular motor that is mainly responsible for the contraction of muscles but also plays a role in actin filament dynamics in the cytoskeleton. Myosin, a 500 kDa dimeric protein, has two heads that interact with an actin filament and through the hydrolysis of myosin-bound ATP, move along the length of the filament. The hydrolysis of ATP to ADP causes the entire head region to bend in a hinge-like

manner due to local conformational changes near the nucleotide binding site (50). ATP first binds to myosin attached to an actin filament, causing the actin filament to immediately dissociate. The ATP hydrolyzes to form ADP-bound myosin, changing the structure of the myosin head from bent to extended and allowing for the myosin to rebind to the actin filament. The ADP is released, causing the myosin head to bend at the hinge (known as a power stroke), moving the actin filament 110 Å (51, 52). Myosin then binds to a new ATP molecule and the cycle repeats.

1.1.3 Actin-Associated Proteins

The cytoplasm of cells contains approximately a concentration of actin 600 to 1200 times the (+)-end critical concentration of purified actin. Therefore, the cell uses various actin-binding proteins to regulate actin polymerization and depolymerization (53). Two of these proteins include thymosin-β4 (5 kDa) and profilin (15 kDa), which both bind with higher affinity to ATP-G-actin than ADP-G-actin (54, 55). Thymosin-β4 sequesters actin monomers and prevents them from adding to filament (+)-ends while profilin aids in polymerization by catalyzing the exchange of ADP to ATP on G-actin and ushering ATP-G-actin to filament (+)-ends (56). Profilin also prevents G-actin from forming nuclei, which can control the density of filaments (57).

Arp2/3 complex, as mentioned previously, increases the nucleation rate of filaments. In addition, it plays a key role in the development of actin networks. Arps are responsible for branching of filaments by binding to the side of actin filaments or filament (-)-ends to nucleate daughter filaments that extend from the mother filament at 70° (58). Another important group of proteins is actin cross-linking proteins, such as α-actinin, which help to create various actin structures and networks by connecting filaments (59). Actin depolymerizing factor (ADF)/cofilins (15-20 kDa) bind with high affinity to ADP-F-actin, causing an acceleration of

the depolymerization of filaments from the (-)-ends and an increase of the free monomer concentration (60). Capping proteins are also present in cells to cap filament ends, inhibiting elongation (61). These proteins regulate the dynamics of the actin network by controlling the length of filaments, preventing an excess of filaments, and ensuring G-actin concentrations are sufficient for various cellular activities.

1.2 Experimental Methods for Actin Polymerization on Modified Substrata

Several previous experimental methods have been used to measure the extent of F-actin elongation and calculate the elongation rate *in vitro*. These include capillary viscometry, difference spectra, and fluorescence with pyrene-labeled actin monomers (62). The major drawbacks of these methods are that filament lengths can not always be determined, and elongation can be monitored, but not visualized, in real-time. Since single actin filaments are 7 nm in diameter, the only ways to observe these filaments are through fluorescent labeling or electron microscopy (63, 64). Previous experiments used phalloidin, a toxin that binds to and fixes actin filaments to prevent them from depolymerizing, in order to measure the length and structure of actin filaments with fluorescent microscopy (63, 65-67). Recently, polymerization assays have been enhanced by total internal reflection fluorescence (TIRF) microscopy, which allows for real-time visualization of elongating actin filaments bound to or near a surface. Manipulation of the substrata through microcontact printing, a technique used for a wide variety of applications, including confinement of cell growth and proteins to a specific pattern, can provide spatial control over filament binding to surfaces.

1.2.1 Total Internal Reflection Fluorescence Microscopy

Until recently, fluorescently-labeled phalloidin was the best method for visualization of filaments in fluorescence because fluorescently-labeling actin monomers directly caused a high background signal from the solution, flooding out the resolution of filaments. Because both EM

and phalloidin-labeling fix the filaments at a static point, these techniques still prevent visualization of filament elongation in real-time. The development of TIRF microscopy allows for filaments bound to surfaces to be visualized in a solution of fluorescently-labeled monomers by only illuminating the 200 nm near the surface of the sample, thus minimizing background fluorescence. Therefore, any fluorophores within the bulk of the sample are not excited, and signals from the excited fluorophores that do emit light are not obscured by any out-of-focus fluorophores (68).

The basis of TIRF microscopy is the evanescent wave created when the light is totally internally reflected at an interface between two mediums with different refractive indices. Specifically, the light travels from a medium with a high refractive index to one with a low refractive index. The evanescent wave is created when light is reflected at an angle equal to or lower than the critical angle, θ_c , and has the same frequency as the incident light but propagates parallel to the interface (Figure 1-2). The critical angle is calculated from Snell's law (Equation 1-1) and is dependent on the refractive indices of the two mediums at the interface.

$$n_1 \sin \theta_1 = n_2 \sin \theta_2 \quad (1-1)$$

The refractive index of the aqueous buffer phase is n_2 , and n_1 is the refractive index of the glass phase. At the critical angle, refraction occurs at an angle of 90° ; therefore $\sin \theta_2 = 1$, and the critical angle is defined by Equation 1-2.

$$\sin \theta_c = n_2/n_1 \leq 1 \quad (1-2)$$

Typically, a laser beam travels through a glass medium first ($n = 1.52$). Contacting this layer is an aqueous buffer phase containing the specimen to be observed. This solution phase has a lower refractive index ($n = 1.33$ - 1.37 for typical aqueous mediums) than the solid phase.

The intensity of the evanescent wave decreases exponentially from the surface to approximately 200 nm, at which point it disappears (Equation 1-3).

$$I(z) = I(0)e^{-z/d} \quad (1-3)$$

The intensity at any position, $I(z)$ is exponentially decreased from the initial intensity $I(0)$ by a function of the ratio of the position from the interface and the penetration depth, d (Equation 1-4).

$$d = \frac{\lambda_o}{4\pi} (n_1^2 \sin^2 \theta - n_2^2)^{-1/2} \quad (1-4)$$

The penetration depth is dependent on the refractive indices, the angle of incidence, and the wavelength of the incident light in a vacuum, λ_o (68).

Actin filaments containing fluorescently-labeled monomers bound to a surface are clearly resolved in TIRF. One way to attach filaments is by adsorbing N-ethylmaleimide (NEM)-myosin to glass (69, 70). NEM binds to thiol groups on myosin, irreversibly inactivating the catalytic site for ATP hydrolysis (71, 72). This allows an actin filament to remain attached to the myosin molecule (Figure 1-2). Amann and Pollard directly observed individual filaments formed from a solution of G-actin partially labeled with rhodamine by using NEM-myosin to bind the filaments to the surface. Their experiments confirmed the elongation rate constants of the (+)-ends of actin filaments as previously found by EM. They also determined that rhodamine-labeled actin was a kinetically inactive label, making it useful for visualizing elongating filaments (73). They showed that Arp2/3 branching in solution occurred at random sites along the filament length, confirming previously published results that used phalloidin stabilization (73). Kuhn and Pollard studied both polymerization and depolymerization rates

further using TIRF to visualize filament (+)- and (-)-end elongation in real-time under a variety of conditions (70).

1.2.2 Microcontact Printing

In our experiments, we patterned NEM-myosin on glass coverslips using microcontact printing to bind actin filaments to the surface and guide their elongation (Figure 1-3).

Microcontact printing is part of a group of techniques known as soft lithography, which uses a patterned elastomer as a stamp, mold, or mask in replacement of a rigid photomask associated with photolithography to create micropatterns (74). Polydimethylsiloxane (PDMS) elastomers are most commonly used for microcontact printing because of a number of advantages, including chemical and thermal stability and durability. This technique was initially used to form self-assembled monolayers (SAMS), or monolayers that form due to the spontaneous aggregation and organization of molecules into a stable structure without the use of covalent bonds (74). Kumar and Whitesides first demonstrated this technique by inking patterned PDMS with feature sizes 1 to 100 μm with hexadecanethiol and then stamping it onto a gold surface (75). The applications of microcontact-printed SAMS were furthered by the selective deposition of other materials onto the monolayers, creating the same pattern with a different exposed material. These materials included conducting polymers, inorganic salts, metals, and proteins (74).

Microcontact printing has more recently expanded to transfer metals, electromagnetic particles, electrochemical particles, and proteins directly. Kind, et al. demonstrated the inking of a solution of Palladium(II) onto a Titanium-coated silicon wafer (76). Iron dots patterned onto a magnetic slave-film have successfully duplicated magnetic signals (77, 78). Applications have also moved toward biology, with Renault, et al. showing that microcontact printing fluorescently-labeled antibodies could provide a method for studying single protein molecules on

surfaces (79). Xu, et al. used a PDMS stamp to transfer patterns of *E. coli* onto an agarose substrate (80). Furthermore, microcontact printing collagen-like proteins has been shown to restrict cell growth to specified regions of surfaces (81).

Microcontact printing can be used for a broad span of applications, however, there are still problems associated with this technique. Distorted patterns may occur due to structural deformation during contact of the surfaces and are enhanced as the dimensions of the stamp become submicron (82). These deformations are inherent due to the elastomeric nature of the polymer. Additionally, an excess of ink and the diffusion of non-covalently bound molecules to unprinted regions of the surface may cause dimensions of the printed pattern to become larger than those on the stamp (82).

1.3 Actin-Based Motility

Actin-based motility occurs when actin filaments elongate against the surface of a motile object, propelling the object forward to make space for the addition of new monomers. *Listeria*, a classic example of actin-based motility, forms an actin rocket tail consisting of thousands of filaments cross-linked into a bundle. Filaments in the tail elongate near the surface of the bacteria, pushing against the bacteria and propelling it forward. Many proteins have been shown to be involved in various types of actin-based motility, including the *Listeria* transmembrane protein ActA and vasodilator-stimulated phosphoprotein (VASP), which may act together as an end-tracking motor (25, 26). These and another group of proteins (formins) have been used *in vitro* to replicate actin-based motility with bacteria and various types of particles.

1.3.1 *Listeria* and Particle Motility

Motility of bacteria in cells, such as *Listeria*, occurs through the recruitment of actin monomers from the host cell's cytoskeleton and the subsequent generation of force through the formation and polymerization of many bundled, cross-linked actin filaments (actin rocket tail) at

the rear of the bacterium (28, 29). *Listeria* motility has been successfully reconstituted *in vitro* in various cell extracts and conditions (83, 84). Although the exact mechanism is unclear (25, 26, 85, 86), it is well-known that the surface protein ActA bound to the membrane of motile *Listeria* is a key protein required for the actin rocket tail formation (87). Current experimental results support the role of ActA and VASP as an end-tracking motor, providing persistent attachment between the filaments and the motile object.

By extracting ActA protein from *Listeria*, polystyrene beads can be functionalized with ActA to mimic *Listeria* motility *in vitro* (88, 89). Beads provide the opportunity to study the mechanism and optimize motility by controlling important parameters, such as diameter and protein surface density of the motile object. Cameron, et al. (1999) successfully used an extraction and purification of histadine-tagged ActA from *Listeria* that was incubated on carboxylated polystyrene beads to coat their surfaces to replicate actin-based motility systems. They found that particle diameter affected the fraction of particles with tails and the velocity of the particles (90).

Experimentally, Cameron, et al. (2001) discovered a single actin filament attached to a 50-nm bead with 37.5% surface coverage of ActA. No average velocity was reported due to thermal fluctuations of the bead and limitations of the imaging equipment (89). However, EM images showed that no 50-nm bead had more than one actin filament attached to it. The length of the actin filament attached to the 50-nm bead indicates that the (+)-end of the filament must have been attached to the bead persistently during elongation, otherwise the bead would have diffused away from the actin filament during fluctuations from the surface for monomer addition (25).

Other studies have supported end-tracking motors as the mechanism for ActA/VASP mediated actin-based motility while also demonstrating the ability of the ActA/VASP complex to support *in vitro* actin-based motility of bacteria and vesicles. Kuo and McGrath were able to track the trailing ends of *Listeria* using an optical trapping and laser particle tracking system. They showed that *Listeria* moves with 5.4 nm steps with pauses in between each step. During the pauses, the bacteria fluctuated 1.31 ± 0.004 nm parallel to and 0.94 ± 0.03 nm perpendicular to the stepwise movement. This was 20-fold less fluctuation than seen by lipid droplets placed next to the bacterium in the same solution, indicating that the actin tail must be coupled to the motile surface (91).

Lipid vesicles undergoing deformation and motility due to actin polymerization was first induced by Upadhyaya, et al. (92). By incubating fluorescently-labeled ActA on the surface of the vesicles, ActA polarized to the end of the vesicle where the actin tail formed. Data showing the vesicle trailing end velocity to be 2.5 $\mu\text{m}/\text{min}$ (six times faster than the vesicles initial velocity) at a “snapping point”, caused by a release of the vesicle, led to the conclusion that the actin was persistently attached to the ActA on the motile surface (92).

Formins, multi-domain proteins that have been found to regulate polymerization of unbranched actin filaments, have also been used to reconstitute actin polymerization *in vitro*. The FH1 domain of formins binds profilin (93) while the FH2 domain binds the (+)-end of the actin filament (27, 94-96). Romero, et al. adsorbed the FH1-FH2 domain from the formin mDia1 onto polystyrene beads and demonstrated a tight coupling between the polymerization and ATP hydrolysis on filaments attached to FH1-FH2 (27). *In vitro*, both ActA- and formin-induced motility provide consistent results for actin-based motility of particles, bacteria, and vesicles, all of which can be exploited in bionanodevices.

1.3.2 Mechanisms

The proteins ActA and VASP are responsible for actin-based motility of *Listeria*, but currently, the mechanism as to how they produce forces is under debate. In the Brownian Ratchet model (97, 98), force is generated by actin polymerization of free-ended filaments impinging on a surface or object. The free energy of ATP-actin monomer addition to the filament (+)-ends is converted into the driving force for the motility (99). The actin filaments are assumed not to be attached to the surface but are stabilized in the cytoplasm through branching and cross-linking.

Thermal fluctuations of the filament (+)-end away from the surface allow the time and space needed for a monomer to add onto the end of the filament. Because the filament cannot diffuse backwards due to the cross-linked network, it pushes forward against the motile surface as it elongates. Based on thermodynamics, the work done on the motile surface can not exceed the free energy released upon monomer addition, given by Equation 1-5.

$$\Delta G_{(+)\text{add}} = -kT \ln \left(\frac{[A_T]}{[A_T]_{(+)\text{crit}}} \right) \quad (1-5)$$

The Boltzmann constant and the absolute temperature, kT , represents the thermal energy, $[A_T]_{(+)\text{crit}}$ is the (+)-end critical concentration of ATP-actin, and $[A_T]$ is the total concentration of G-actin. When depolymerization at the (-)-end of the filament is occurring, the concentration of actin monomers must be less than the critical concentration at the (-)-end. Based on this concentration estimation and the length per monomer addition of 2.7 nm, the maximum force that a filament can apply to a surface by monomer addition alone is 2 pN. This theoretical force is smaller than previously published force estimations used for steady-state elongation (86, 100).

In the actoclampin model, elongating filaments are persistently attached to the surface through a multivalent surface-bound protein that interacts with high affinity for ATP-actin

monomers. The free energy released upon hydrolysis of ATP is assumed to drive affinity modulations between the end-tracking proteins and the filament (+)-end in a way that converts the hydrolysis energy into the mechanical work used for inserting new monomers and pushing on the motile surface. End-tracking motors may also provide some protection of elongating filament ends from capping proteins while transferring a profilin-actin complex into the filament (26). In addition to the 2 kT of energy available from the addition of one subunit, actoclampin can utilize as much as 14 kT per subunit of free energy from ATP hydrolysis (25).

Experimental results, including the dependence on profilin and ATP hydrolysis, show that formins behave like “actoclampin” filament end-tracking motors (25-27, 101, 102). In the case of *Listeria*, the putative actoclampin motor includes both VASP and ActA (26). VASP contains an EVH2 domain, which binds both G-actin and F-actin, and an EVH1 domain, which has binding sites on ActA. VASP also contains a proline-rich domain which is thought to recruit profilin-actin for subsequent addition onto the filament (+)-ends (103). Supporting this proposed role of profilin in actin-based motility by actoclampin, fluorescently-labeled profilin has been observed to localize to *Listeria*'s surface during motility, with the speed of *Listeria* directly proportional to the fluorescent intensity (104).

1.4 Bionanodevices

Both actomyosin and a similar system using kinesin with associated microtubules have been exploited to transport material *in vitro*. Two different methods exist for the mechanism of transport. The first is the sliding filament assay which relies on immobilized myosin or kinesin to transport actin filaments or microtubules, respectively. The second assay is the immobilized filament assay, which binds actin filaments or microtubules to a surface to create a path for myosin or kinesin to walk along. Both have been shown to transport cargo in a directive manner.

1.4.1 Sliding Filament Assay

The sliding filament assay is more commonly used than the immobilized filament assay because it is easier to set up and execute experiments (32). Typically, surfaces contain a region with high affinity for protein adsorption and a region with low affinity. Bunk, et al. found that the photoresist materials MRL-6000.1XP and ZEP-520 both efficiently adsorbed heavy meromyosin (HMM) and subsequently bound and moved actin filaments in contrast to PMMA-200, PMMA-950, and MRI-9030, which exhibited poor motility. For this reason, they created 100 to 200 nm grooves in a material layer exhibiting low motility (PMMA-950) to expose an underneath layer with high motility behavior (MRL-6000.1XP) to efficiently guide actin filaments (8). Another method for surface modification includes the use of high-resolution e-beam patterning exposure of a poly[(tert-butyl-methacrylate)-co-(methyl methyl methacrylate)] to make hydrophobic (high-energy exposure) and hydrophilic (low-energy exposure) regions, the latter with a low affinity for HMM adsorption and subsequent filament binding (19). Microcontact printing was used to create SAMs on gold surfaces and attach biotinylated myosin to the patterned region. This method ensured the orientation of the myosin would be optimal for gliding actin filaments (18).

Clemmens, et al.(2003) tested kinesin adsorption and the guidance of microtubule motility on three different designs: a chemical border between ppPEO (low affinity for kinesin) and glass, a channel with floors and walls made from polyurethane, and a combination of the two, using SU8-PEO photoresist to make non-adhesive walls with channel floors made of SiO₂ for adsorption of kinesin. The most efficient design was the latter, which combined both chemical definition and topographical boundaries (105). This design was further optimized by using AZ5214 as the non-adsorbing photoresist on glass and creating channel walls with an undercut to prevent microtubules from climbing over the sides of the channels (17).

Sliding assays have also allowed for the exploration of many different track shapes, which may be beneficial for sorting the direction of the moving filaments. Suzuki, et al. observed actin filaments moving in concentric circles, letters, and figure eights on PMMA surfaces (21). Paths of microtubules have been studied in channels using different crossing junctions, including tangent circles and crosses, as well as concentric circles (16). Additionally, the sorting of microtubules has been examined by using arrow heads or tangent, straight channels shooting off of circular paths (12, 13, 16). These types of devices are designed to catch any microtubule traveling in an opposite direction in these “traps” and allow for the filament to turn around. The ultimate goal is for all filaments to be moving in the same direction.

1.4.2 Immobilized Filament Assay

Fewer attempts have been made to immobilize filaments for myosin- or kinesin-mediated cargo transport. Glass particles attached to kinesin have successfully traveled along gluteraldehyde-immobilized, isopolar microtubule arrays (3). Nanocrystals have also been shown to travel along microtubule arrays fixed to the surface by poly-L-lysine (5). Reuther, et al. has biotemplated microtubules into single-molecule tracks, which bind kinesin. These immobilized filaments successfully guided another microtubule along the path by binding kinesin to the immobilized microtubules (22). Actin paracrystal structures formed in lipid bilayers have been shown to guide myosin-coated glass beads (6). Immobilized-filament assays have the potential to guide myosin (or kinesin)-mediated cargo unidirectionally by orienting the filament (+)-ends to point in the same direction (32). One attempt to align filament polarity successfully used electrostatic condensation of F-actin/gelsolin to create an unidirectional track for myosin-bound bead transport (19).

1.4.3 Material Transport

An important aspect of all of these techniques is that they are able to transport material in a controlled manner. In bionanotechnology, particles have the advantage of being functionalized to not only move by actin-based motility but also to bind to specific proteins or molecules that need to be transported against flow or diffusion gradients. As mentioned above, guidance of various particles bound to kinesin and myosin have been attempted. Quantum dots (7.6 nm diameter) functionalized with kinesin were observed moving along microtubule tracks at an average velocity of 0.28 $\mu\text{m}/\text{sec}$, for distances ranging from 1 to 5 μm , with the number of events falling exponentially as the distance increased (5). Larger kinesin-coated spherical particles (1.8 to 2.8 μm) made from glass, polystyrene, and paramagnetic polystyrene traveled along isopolar microtubules for 1 to 2.5 μm at a rate of approximately 0.5 $\mu\text{m}/\text{sec}$. Suda and Ishikawa found that myosin-bound particles with 65 μm diameters slide at rates of 338 $\mu\text{m}/\text{sec}$ on actin filament paracrystal structures (6).

Sliding actin filaments and microtubules have also been shown to carry attached cargo. Bachand, et al. showed the transport of quantum dots attached to microtubules along a kinesin-coated surface (2). Similarly, Mansson, et al. showed transport of quantum dots attached to actin filaments on a myosin-coated surface (4). This same technique has been used for motile microtubules labeled with antibody sandwiches, i.e. the microtubule can selectively bind a target antigen and then a secondary antibody for detection (14). Suzuki, et al. successfully transported a gelsolin-coated polystyrene bead (1 μm diameter) attached to the (+)-end of an actin filament on a myosin surface (7). All of these examples demonstrate the ability to successfully transport cargo against flow and diffusion gradients through a variety of mechanisms, all using biomolecular motors.

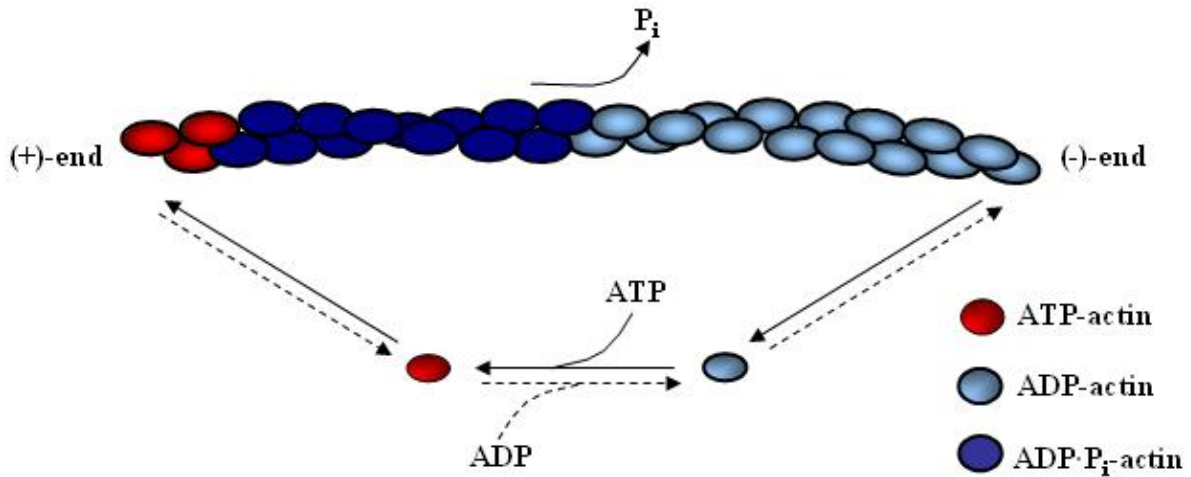


Figure 1-1. Treadmilling of an actin filament. ATP-actin binds to the (+)-end of the filament. The ATP hydrolyzes, forming an intermediate monomer in the filament, ADP·P_i-actin. The phosphate is eventually released, leaving the remaining monomers in the filament as ADP-actin. The monomers at the (-)-end dissociate from the filament and are released back into the solution, where the ADP molecule is exchanged for an ATP molecule, and the cycle repeats.

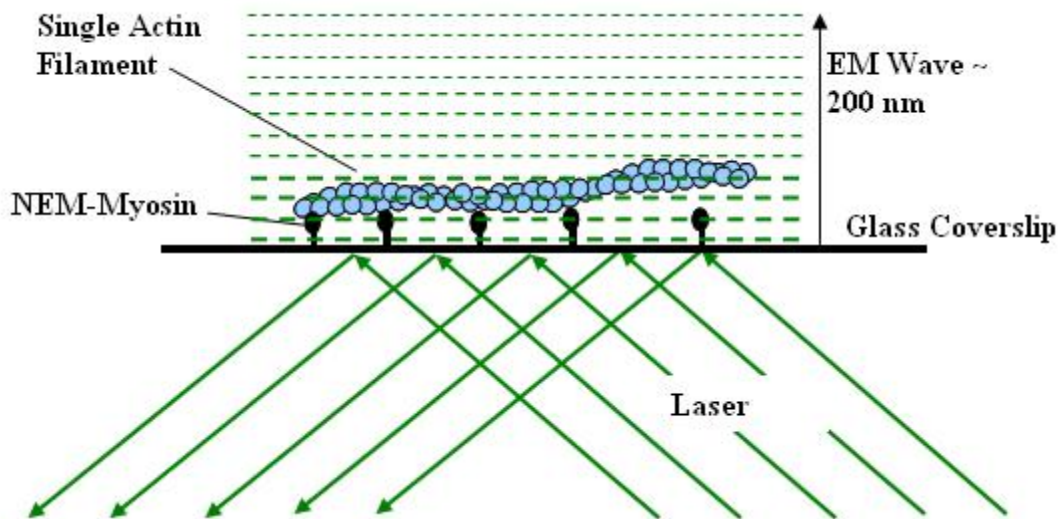


Figure 1-2. Experimental set-up for binding filaments to a surface. NEM-myosin is adsorbed to a glass coverslip, where it binds a polymerizing actin filament. A laser beam is totally internally reflected at the interface of the glass coverslip and the sample solution. This creates the electromagnetic (EM) wave, known as the evanescent wave, which excites any fluorescently-labeled molecules attached to monomers that have incorporated into the actin filament.

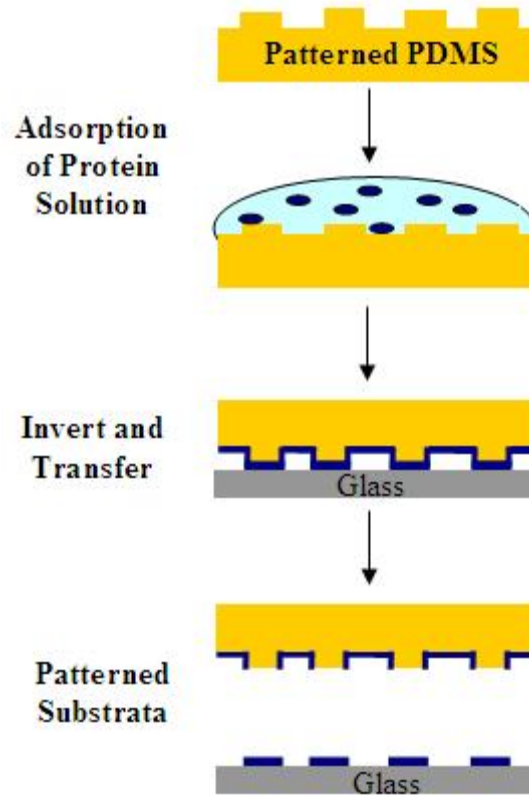


Figure 1-3. Schematic of microcontact printing protein on glass. A patterned piece of PDMS is incubated with a solution of protein. The stamp is dried and placed in contact with the glass surface. When the stamp is removed from the glass, the protein that was directly contacting the glass is transferred onto the glass in the corresponding pattern.

CHAPTER 2
GUIDANCE OF ACTIN FILAMENT ELONGATION ON FILAMENT-BINDING TRACKS

2.1 Introduction

Guidance of single actin filament elongation is a simplified system to study the potential of actin-based motility for applications in nanotechnology. By directing single actin filament elongation, controlled tracks of actin filaments for cargo-carrying myosin can be created. In addition, single-filament propulsion of small particles (~50 nm in diameter) is predicted to behave in a similar way on filament-binding tracks as elongating actin filaments without particles. We developed and characterized the ability of microcontact-printed tracks of immobilized filament-binding proteins (NEM-modified myosin) to guide the direction of filament elongation. The direction and rate of polymerization of individual surface-bound filaments were directly observed and quantified using TIRF microscopy (69, 70). Printed NEM-myosin tracks were found to capture nascent filaments from solution and guide their subsequent elongation to a degree that was dependent on the track width and myosin density. These findings suggest a mechanism whereby the myosin track can recapture the tips of undulating filaments that cross track boundaries at sufficiently small glancing angles.

2.2 Materials and Methods

2.2.1 Protein Preparation

Actin was polymerized from a mixture of unlabeled and fluorescently-labeled G-actin. To prepare unlabeled actin, we resuspended commercial G-actin that was lyophilized as a 10 mg/mL actin solution in 5 mM Tris-HCl pH 8.0, 0.2 mM CaCl₂, 0.2 mM ATP, 5% sucrose and 1% dextran (Cytoskeleton, Inc., Denver, CO) in 25 μ L deionized H₂O and incubated the sample on ice for at least 2 h to dissolve the protein thoroughly. After 24-h dialysis against G-buffer (5 mM Tris-HCl pH 8.0, 0.01% NaN₃, 0.1 mM CaCl₂, 0.5 mM Dithiothreitol (DTT), 0.2 mM ATP),

with three buffer exchanges, actin was collected and clarified by centrifugation at $107,000 \times g$ for 2 h at 4 °C in a TLA100.2 rotor (Beckman Coulter, Inc., Fullerton, CA). G-actin was stable at 4 °C for up to two weeks. Lyophilized actin with random surface lysine residues covalently bound to an activated ester of rhodamine (Cytoskeleton, Inc., Denver, CO) was used (without dialysis) at a stock solution concentration of 23 μM after the powder was resuspended in deionized water for three days at 4 °C.

To prepare Alexa 488-labeled actin (73), purified rabbit muscle G-actin (106) was polymerized at a concentration of 60 μM by dialysis against polymerization buffer (2 mM 3-morpholinopropanesulfonic acid (MOPS) pH 7.5, 50 mM KCl, 1 mM MgCl_2 , 0.2 mM ATP). A 5-fold molar excess (300 μM) of Alexa Fluor 488 carboxylic acid, succinimidyl ester (Invitrogen, Molecular Probes, Carlsbad, CA) in dimethyl sulfoxide (DMSO) was added to the polymerized actin and left overnight at 4 °C. Labeled F-actin was then centrifuged at $288,000 \times g$ for 30 min at 4 °C in the TLA100.2 rotor. G-actin was prepared from this pellet by resuspension and 48-h dialysis against G-buffer. Monomeric actin was collected and centrifuged at $107,000 \times g$ for 2 h at 4 °C to remove oligomers. The monomer-rich supernatant was collected, aliquoted, rapidly frozen in liquid nitrogen, and stored in -70 °C for up to six months.

For actin filament binding in the absence of myosin-mediated motility, myosin II ATPase activity was inactivated by N-ethylmaleimide (NEM) treatment, as described elsewhere (70). The contents of five tubes of commercial lyophilized 95%-pure myosin II (Cytoskeleton, Inc. Denver, CO) was resuspended in 250 μL deionized H_2O , yielding a 20 mg/mL myosin solution. After 2-h dialysis at 4 °C against 10 mM Imidazole, pH 7.0, 10 mM ethylene diamine tetraacetic acid (EDTA), and 500 mM KCl (myosin dialysis buffer), the protein was diluted to 10 μM in the same buffer, and reacted with 1 mM of NEM for 1 h on ice. DTT (1 mM) was used to quench

the unreacted NEM for an additional 1 h on ice. After overnight dialysis at 4 °C against 10 mM Imidazole, pH 7.0, 500 mM KCl, 10 mM EDTA, and 1 mM DTT, with one additional buffer exchange, NEM-myosin was aliquoted, rapidly frozen in liquid nitrogen, and stored at -70 °C for up to six months.

Purified, precipitated profilin expressed from *Escherichia coli* and stored in lysis buffer (20 mM Tris-HCl pH 8.0, 1 mM EDTA, 1 mM DTT, and 1 mM phenylmethanesulphonyl-fluoride (PMSF)) in the presence of 40 mM NaCl was generously donated by Dr. William Zeile. Profilin precipitate was spun at 16,000 × g for 20 min in an Eppendorf 5415C microcentrifuge, resuspended in 4× polymerization buffer (20 mM Imidazole pH 7.0, 200 mM KCl, 4 mM MgCl₂, and 4 mM ethylene glycol tetraacetic acid (EGTA)), and dialyzed for 48 h against the same buffer at 4 °C.

2.2.2 Microcontact Printing

NEM-myosin was microcontact-printed as parallel tracks on glass coverslips with the aid of a polydimethylsiloxane (PDMS) stamp. A silicon wafer mold of desired pattern was created by light exposure of SU8 photoresist (Microchem Corporation, Newton, MA) using a Karl Süss MA-6 photoresist microlithographer. A mixture of 10:1 prepolymer to catalyst of Sylgard 184 (Dow Corning Corporation, Midland, MI) was degassed and poured onto the surface-fluorinated silicon wafer, after which PDMS was polymerized in the mold at 60 °C for 1 h (107). The PDMS stamps were generously made and donated by Dr. Suzanne Ciftan-Hens (International Technology Center, Raleigh, NC).

The resulting hydrophobic PDMS stamps (with tracks ranging from 3 - 20 µm wide) were inked for 40 min with a NEM-myosin solution, washed three times with myosin dialysis buffer, three times with deionized H₂O, and dried under nitrogen (79, 107). After acid-washing and treatment as described elsewhere (70), glass coverslips (No. 1, Fisher Scientific, Waltham, MA)

were pressed and left in contact with a stamp's inked-surface for 20 min. The resulting stamped coverslips were either examined by atomic force microscopy (AFM Dimension 3100, Veeco, Woodbury, NY) or used in hand-fabricated flow-cells constructed by adhering the inverted coverslip onto a microscope slide with double-sided Scotch tape. Until use, flow-cells were stored in myosin dialysis buffer for up to 6 h.

2.2.3 Actin Polymerization

Actin filaments were polymerized according to a previously published protocol (70). Actin monomer solution was combined with a 10× magnesium-exchange buffer (10 mM EDTA, 1 mM MgCl₂) and incubated on ice for 5 min to convert Ca-ATP-actin to Mg-ATP-actin. The Mg-ATP-actin was then mixed with a 2× concentrated polymerization buffer (20 mM Imidazole pH 7.0, 100 mM KCl, 2 mM MgCl₂, 2 mM Ethyleneglycol-bis(β-aminoethyl)-N,N,N',N'-tetraacetic Acid (EGTA), 20 mM DTT, 0.4 mM ATP, 1% methylcellulose, 30 mM glucose, 40 μg/mL catalase and 200 μg/mL glucose oxidase) for a final concentration of 0.75 to 1.5 μM actin (15-30% fluorescently-labeled). This solution was immediately transferred into the flow-cell.

Prior to experiments, flow-cells containing cleaned glass coverslips were treated according to Kuhn and Pollard (70), with 0.2 μM NEM-myosin for 1 min followed by 1% bovine serum albumin (BSA) in 50 mM Tris-HCl, pH 7.6, 600 mM NaCl (HS-TBS) to remove any unbound NEM-myosin, followed by washing with 1% BSA in 50 mM Tris-HCl, pH 7.6, 50 mM NaCl (LS-TBS) to remove any unbound NEM-myosin, lower the salt concentration in the flow chamber, and to passivate any exposed glass (70). The volume of each wash was approximately twice the chamber volume. Flow-cells possessing NEM-myosin-stamped coverslips were washed with the 1% BSA in 50 mM Tris-HCl, pH 7.6, 600 mM NaCl and 1% BSA in 50 mM Tris-HCl, pH 7.6, 50 mM NaCl before actin solution was added.

2.2.4 TIRF Microscopy and Data Analysis

To observe our samples, we used a commercial objective-based TIRF consisting of a Nikon Eclipse TE1200 inverted microscope fitted with TIRF optics (Nikon Instruments, Melville, NY) and an Argon 488-nm or a Helium-Neon 532-nm laser (Melles Griot, Carlsbad, CA). Images were acquired using a digital charge-coupled device (CCD) camera (QImaging, Burnaby, BC, Canada) and analyzed using MetaMorph software (Molecular Devices Corporation, Sunnyvale, CA). Time-lapse images of each field-of-view were taken at 5-sec intervals.

To quantify filament orientation, the filament images were first discretized into segments by selecting points spaced 0.1 - 3 μm apart along the filament length. We only analyzed those filaments that were elongating during the observation time. Filaments that spanned the NEM-myosin track border were discretized up until the track edge. Furthermore, to eliminate the possibility that interacting filaments might bias the data, images containing a high density of elongating and non-elongating filaments near the surface were excluded. The minimum number of independent tracks for each track width was ten, while each track width contained measurements from at least 84 filaments. The minimum number of independent tracks for one NEM-myosin treatment concentration was ten, while each condition contained measurements from at least 86 filaments.

Taking θ as the angle between the segment and the track direction, the mean of $\cos(2\theta)$ (weighted by segment lengths) for each filament was calculated. A mean of $\cos(2\theta)$ equal to one corresponds to perfect alignment, and a value of zero indicates random alignment. An overall $\cos(2\theta)$ for each track width was calculated by averaging the $\cos(2\theta)$ values of the filaments, weighted by the filament length. Data were collected from samples run on different days, but a one-way ANOVA between the samples for each track width concluded that no statistical

differences were present between days. Therefore, each individual track was considered an independent sample and was used to determine the standard error for each condition.

The weighted mean $\cos(2\theta)$ was plotted against both track widths and NEM-myosin treatment concentrations with error bars representing the \pm standard error (SE) based on a weighted standard deviation (SD). To determine if the alignment of the filaments was significant, a one-sample t-test was used to calculate a one-tailed p-value by comparing the average $\cos(2\theta)$ for each track width and NEM-myosin concentration with a $\cos(2\theta)$ value of zero for random alignment. The highest and lowest NEM-myosin treatment concentrations were compared using a two-sample t-test. Filaments within 1.5 μm of the track edge were pooled to obtain alignment near the edge of the track. In addition, the average distance of each filament segment from the edge of the track was estimated based on positions obtained manually from MetaMorph, and the distances were plotted against the alignment for each segment to create scatter plots for all samples.

Changes in filament length were measured for a minimum of three time-points per filament, allowing us to calculate the elongation rate of filaments for each NEM-myosin and profilin concentration from a line-fit of filament length versus time (with each 0-time intercept set to 0). Instantaneous elongation rates, with subunits/sec values (based on 370 subunits per μm filament length), were pooled from at least 12 filaments for each NEM-myosin concentration and at least 13 filaments for each profilin concentration. Elongation was observed and measured at filament (+)-ends only. Elongation rates for the four NEM-myosin treatment concentrations were tested for statistical differences using a one-way ANOVA.

2.3 Results

2.3.1 Filament Binding to Stamped Surfaces

Using the microcontact-printing procedure, we produced and characterized filament growth on myosin tracks of six different average widths \pm SD (3.3 ± 0.3 , 4.3 ± 0.5 , 5.7 ± 0.2 , 10.7 ± 1 , 15.1 ± 0.8 , 20.2 ± 0.5 μm). Fluorescence and AFM images were taken to assess the uniformity of NEM-myosin coverage. As shown in Figure 2-1A, the NEM-myosin regions were clearly delineated by the preferential non-specific adsorption of fluorescent actin monomers or oligomers with the NEM-myosin regions relative to the BSA regions. The magnified three-dimensional AFM image (Figure 2-1B) of a representative track edge shows a confluent protein layer, with thickness shown in Figure 2-1C. The measured thickness variation of the protein layer is comparable to the 7-nm diameter of a single actin filament, implying that the peaks and valleys of the layer should have little effect on the guidance of the filaments.

The microcontact-printed surfaces were exposed to the actin solution, allowing capture of nascent filaments from solution by the NEM-myosin-coated regions with the majority of captured filaments continuing to elongate on the surface. (Surfaces stamped with 0.5 mg/mL BSA showed little evidence of filament binding, as shown in Figure 2-2.) We were able to monitor (+)-end filament elongation on the NEM-myosin tracks in real-time using TIRF microscopy (Figure 2-3). Notably, the tips of myosin-bound filaments clearly undulate during elongation, and the filaments continue to bind to NEM-myosin along their length as they extend. While filament segments were found both on the tracks and on the BSA-coated regions, filament segments on the BSA regions underwent larger thermal undulations (observed in the x- and y-direction) than those confined on the NEM-myosin track, indicating that filaments were tightly bound only to the NEM-myosin tracks (Figure 2-4). Filaments initially bound to the track either remained in the NEM-myosin region or elongated beyond the track edge, with the filament end

continuing to elongate and undulate over the BSA-coated region (Figure 2-5). In many cases, these undulations allowed a filament which had crossed the boundary of the NEM-myosin track at a glancing angle to rebind to the track, now with the filament end often aligned with the track edge (Figure 2-6).

2.3.2 Alignment of Filaments

To determine the effect of the NEM-myosin tracks on the filament alignment, we first eliminated samples containing a high density of actin filaments on the surface in the track region (Figure 2-7). The high density of filaments near the surface may increase filament-filament interactions, which could then increase the alignment of the filaments with each other. Also, the dense samples were difficult to analyze because individual filaments were not always distinguishable.

The resulting alignment of the filaments with the track edge was quantified by measuring the angle θ for segments along each of several filaments for each track width (Figure 2-8A) and calculating the mean of $\cos(2\theta)$. Filament alignment on the narrower track widths was found to be significant and the degree of alignment increased as the track width decreased (Figure 2-8B, solid squares). To determine whether alignment resulted primarily from interactions with track boundaries, the mean of $\cos(2\theta)$ was re-calculated for the subset of filaments within approximately $1.5 \mu\text{m}$ of the track edge on tracks wider than $3.3 \mu\text{m}$ (Figure 2-8B, open squares). The filaments near the track boundaries had a similar degree of alignment independent of the track width. These observed trends are consistent with the interpretation that filaments in tracks with widths comparable to the filament persistence length ($\sim 10 \mu\text{m}$ (48, 49)) take random walk trajectories within the boundaries of the track and only become aligned when encountering the track boundary. On the other hand, filaments in tracks that are small relative to the filament

persistence length encounter the track boundary and become realigned before significant changes in direction occur (Figure 2-8C).

The probability of realignment of a filament with the track edge is also dependent on the alignment of the filament immediately before crossing the NEM-myosin track edge. The histogram in Figure 2-9 demonstrates that at smaller alignment angles, these rebinding events were more frequent, ranging from ~90% recapture-probability for angles less than 15° decreasing to zero probability at angles greater than 60°. From this result, we surmise that the bending energy at large angles required to recapture a filament is too large to be achieved by thermal undulations. To confirm that thermal undulations caused this bending, we estimated the bending energy of several filaments from Equation 2-1 (108).

$$E_{\text{bend}} = k_B T \frac{\lambda}{2} \int \left(\frac{d\theta}{ds} \right)^2 ds \quad (2-1)$$

The thermal energy is $k_B T$ (Boltzmann constant multiplied by temperature), λ is the filament persistence length ($\sim 10 \mu\text{m}$ (48, 49)), and s is the arc length of a filament that crossed the boundary and then bent back to be captured by the track. In each case, E_{bend} was on the order of $k_B T$, suggesting that changes in filament direction were driven by thermal energy (49).

A scatter plot shows all of the filament segments and their alignment as a function of distance from the edge of the track (Figure 2-10). Segments seem to be concentrated near the edge at both aligned ($\cos(2\theta) = 1$) and unaligned angles ($\cos(2\theta) = -1$). This suggests when filaments reach the edge of the track, they tend to realign at small angles, increasing alignment, or they leave the track completely at large angles, making the distribution of segment angles near the track edges at the extremities.

2.3.3 NEM-Myosin Concentration

We also investigated the effect of NEM-myosin concentration used to treat the PDMS stamps on the alignment of elongating filaments. As shown in Figure 2-11A, the degree of alignment, again quantified by the mean $\cos(2\theta)$, trended upward with NEM-myosin treatment concentration, with the degree of alignment on tracks prepared with the highest concentration tested (2 μM) significantly greater than that of the lowest (0.1 μM), the latter of which failed to generate statistically significant alignment. These results suggest that lower NEM-myosin surface densities are less efficient at recapturing undulating filament ends that have elongated off the track edge. Finally, we anticipated that at higher densities, myosin might bind at or near the filament (+)-ends and thereby hinder monomer incorporation. To determine the effect of myosin concentration, we measured the elongation rate of filaments on the protein tracks prepared with varying NEM-myosin concentrations used in Figure 2-11A. As shown in Figure 2-11B, the elongation rate decreased only slightly for the highest myosin concentration, implying that the NEM-myosin had little effect on actin polymerization.

Scatter plots of segment distance from the track edge versus filament alignment for each NEM-myosin concentration are shown in Figure 2-12. The 0.1 μM NEM-myosin treated sample has the least bias of filament segments aligned near the edge of the track, presumably due to the low concentration of myosin available to rebind and realign filaments. The 0.5 and 2 μM samples show a slight bias toward aligned filament segments. The 1 μM sample, which had the most segments available for analysis, is the subset of the filaments in Figure 2-10 that were on a 5 μm wide track. Therefore, the 1 μM sample shows the same trend as Figure 2-10, again indicating that the alignment of filament segments closer to the track edges is independent of track width.

2.3.4 Control of Actin Polymerization

Figure 2-13 shows a sample in which filaments accumulated within the BSA regions (spaces where NEM-myosin was not stamped). Although these filaments undergo large thermal undulations, unlike those that are bound onto the NEM-myosin tracks, their accumulation seems to prevent filaments from binding to the NEM-myosin track. These interactions could be due to NEM-myosin molecules that adsorbed onto an area that was not within the stamp, interactions between actin filaments, nonspecific interactions between actin filaments and BSA or glass, or a combination of all three effects. The density of filaments in these regions is observed to increase over time, presumably because of the strong effects actin filaments have on each other. In addition, if the filaments are diffusing to the surface as long filaments (lengths greater than the track width), the filaments at most may lay across the track at some angle rather than align with the track.

One way to potentially prevent this behavior is to control actin polymerization through nucleation to prevent filaments from accumulating near the surface within a short time frame. Protein samples may contain small oligomers that cause the density of filaments to increase at much higher rates than other samples. Also, the lyophilized rhodamine actin used contains groups of actin monomers that have not completely dissolved, causing them to behave as potential nuclei. Figure 2-14 shows how the actin filament density is decreased by increasing the resuspension time of the lyophilized rhodamine actin, allowing for the breakdown of the aggregates of actin monomers.

In an attempt to control the polymerization further, profilin was mixed in with the polymerization assay at concentrations between 1 and 20 μM . On surfaces treated with NEM-myosin, profilin clearly had an effect on the filament density near the surface (Figure 2-15). The elongation rate of filaments exposed to varying levels of profilin decreased only

slightly as the profilin concentration increased (Figure 2-16). This indicates that the decrease in filament density near the surface is mostly due to the sequestering of monomers of actin, thus preventing nuclei from forming. The decrease in elongation rate may have only a slight effect on the density. Although the decrease in density was apparent on NEM-myosin surfaces, when attempting to use profilin in an assay with stamped surfaces, the amount of labeled actin monomers that did not incorporate into filaments created a high background on the surface, making visualization of elongating filaments over time difficult to achieve.

2.4 Discussion

The data presented demonstrates that microcontact printing can be used as an effective way for guiding the polymerization of actin filaments. By printing NEM-myosin tracks on glass surfaces, actin filament binding was confined to certain regions of a substratum and aligned by controlling the path of filament elongation. Smaller track widths provided the greatest degree of alignment by increasing the frequency of elongating ends encountering the track boundaries, whereupon the filament elongation direction tended to preferentially align with the edge of the NEM-myosin tracks, and alignment appeared to be confined primarily to the track boundaries. The degree of alignment, but not the polymerization rate, depended on the concentration of NEM-myosin used to prepare the stamp, with the lowest concentration (0.1 μM) generating little, if any, alignment. Notably, this lower value is near the minimum concentration needed to provide a monolayer on the PDMS stamp (20), hence it is likely that, in this case, less than a confluent layer was transferred upon printing.

2.4.1 Mechanism for Filament Alignment

Taken together, our results can be explained by the following alignment mechanism (Figure 2-17). Nascent filaments are captured on the track surface and elongate on the NEM-myosin. As a filament elongates, the newly polymerized portion is quickly captured by

the myosin surface until the filament end reaches the NEM-myosin track boundary. The filament continues to grow across the boundary while unattached to the substratum and becomes capable of undergoing larger thermal undulations. These undulations allow the filament to be recaptured to the track in a more aligned direction, provided the angle at which the filament encounters the track boundary is sufficiently small, and the myosin surface density is sufficiently large to allow NEM-myosin in the track to rebind the undulating filament end.

Clemmens, et al. previously demonstrated a similar tendency of microtubules gliding along a kinesin-coated surface to align at a chemically-defined border (105). They found that microtubules began to undulate as they crossed a border from kinesin-rich to kinesin-poor surface regions and that their fluctuations were sufficient to re-align the gliding microtubules at small approach angles. Furthermore, Sundberg, et al. observed a comparable trend when analyzing the guidance of gliding actin filaments with respect to their approach angle on myosin tracks with a chemically-defined border (15). While similar, the mechanism in our study differs in that the filament lengths are bound and do not slide relative the substratum, and the elongating filament end moves by undulating about a fixed mean position determined by orientation and position of the immobilized portion of the filament.

Our findings suggest that at narrower track widths than measured here, even greater alignment would be achieved, with greatest alignment occurring when the myosin track widths approach the filament width, similar to what was previously observed with sliding microtubules on kinesin tracks (provided that the track of kinesin was no wider than the microtubule itself) (22). Also similar to our observed effect of track edges on elongation direction, Nicolau, et al. observed an increased alignment of (non-elongating) actin filaments gliding by ATP-dependent myosin translocation near the boundary of regions with different myosin density (19).

2.4.2 Potential and Applications

Our results indicate that filament-binding tracks are a viable method for guiding the direction of filament elongation on surfaces *in vitro*. A potential application is laying single-filament tracks for myosin-based transport of nano- or microparticles (i.e., “molecular shuttles”) (10). One advantage of this technique over other methods for depositing filaments on patterns (e.g. electrophoresis and flow) is that the polymerization of individual filaments could be potentially guided to follow tracks with complex patterns (e.g., with curves and bends, without sharp angles), thereby achieving more complex systems and networks of myosin-mediated transport. Moreover, after the initial segment is deposited (perhaps with position and orientation controlled by flow or electrophoresis (23, 32, 109)), the polarity of the generated filament track would be controlled by its (+)-end-only elongation, thereby ensuring the proper orientation for unidirectionally-guided myosin-based shuttles.

F-actin binding tracks can potentially guide elongation of individual long filaments or multiple interconnected shorter filaments over long distances (hundreds of microns) for long-distance transport of nano- and micro-scale cargo. The filament density depends on the filament nucleation rate and can be controlled biochemically (e.g., by adding profilin). We have shown that profilin reduces the density of actin filaments near the surface with little effect on the elongation rate. Optimization of the microcontact printing procedures and actin filament polymerization assay can provide control over not only filament density, but also filament elongation rates, total length per filament, and non-specific interactions between filaments and the low-affinity surfaces (BSA and glass).

A second class of potential applications for oriented filament elongation could be the guidance of molecular shuttles bound to the elongating filament (+)-ends, rather than relying on myosin-based transport of gliding filaments bound to cargo (4, 7). End-tracking proteins are

capable of linking the elongating actin filament end to a particle and facilitating insertional polymerization of the tethered end (25-27). Because elongation is guided by filament undulations and filament binding to the track, we would expect similar guidance of elongating filaments with or without particles bound to the filament ends, provided the particles are small enough not to interfere with the undulating end.

In summary, guided elongation of free filament (+)-ends represents an additional tool for transporting molecular shuttles, either by laying tracks in specific patterns for myosin-based shuttles, or by guiding propulsion of particles bound to filament (+)-ends. Further investigation of surface properties, including other methods of binding filaments, density of filament-binding molecules, and varying track shapes, may provide additional control over the alignment and guidance of polymerizing actin filaments. This approach, which relies on filament elongation rather than filament transport, should complement other published methods for actin alignment and actin-based molecular shuttles (6, 23-24) and broaden the methods available for transport in bio-based nano-devices.

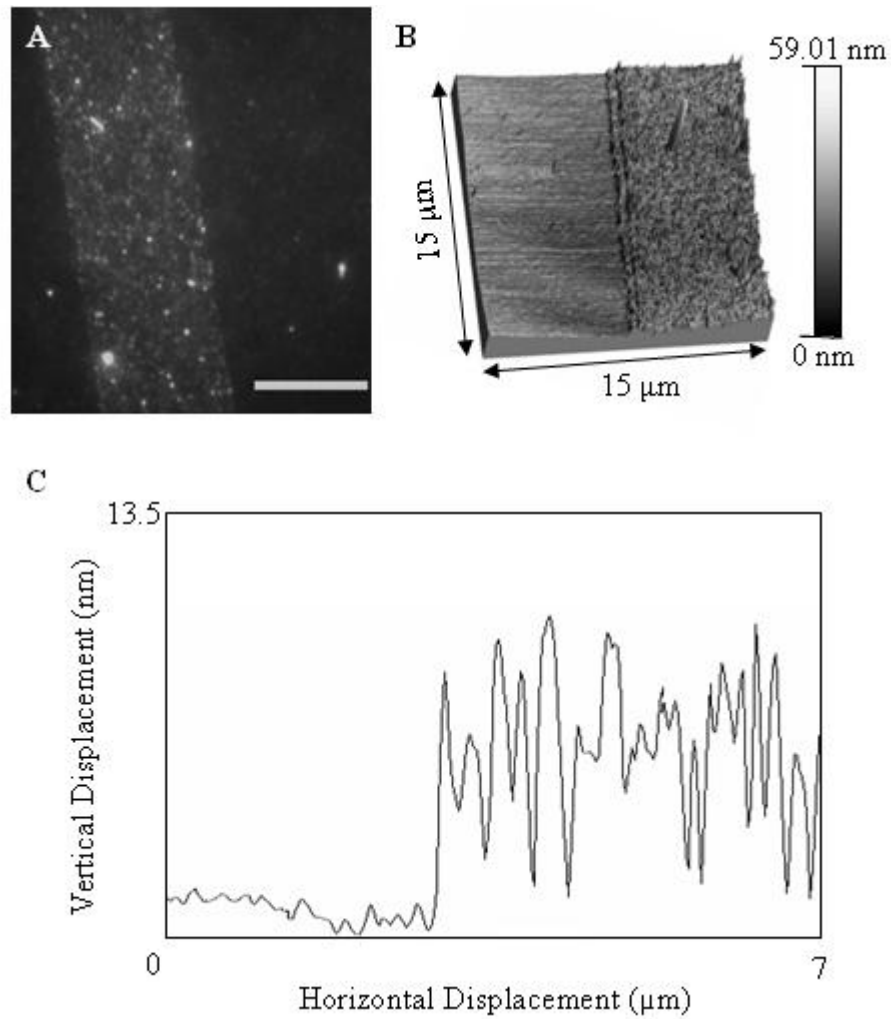


Figure 2-1. Images of microcontact-printed myosin tracks on a glass coverslip. A) TIRF image of NEM-myosin track (brighter region slightly right of center) delineated by nonspecific adsorption of fluorescently-labeled actin monomers to adsorbed NEM-myosin (scale bar = 10 μm). B) Topographic AFM image of track edge showing uniformity of NEM-myosin coverage. C) Line-scan of vertical displacement versus horizontal displacement from plot B. The height of the step-edge was found to be approximately 8 nm and the peak-to-valley height variations in the NEM-myosin region were found to be on the order of 4.4 nm.

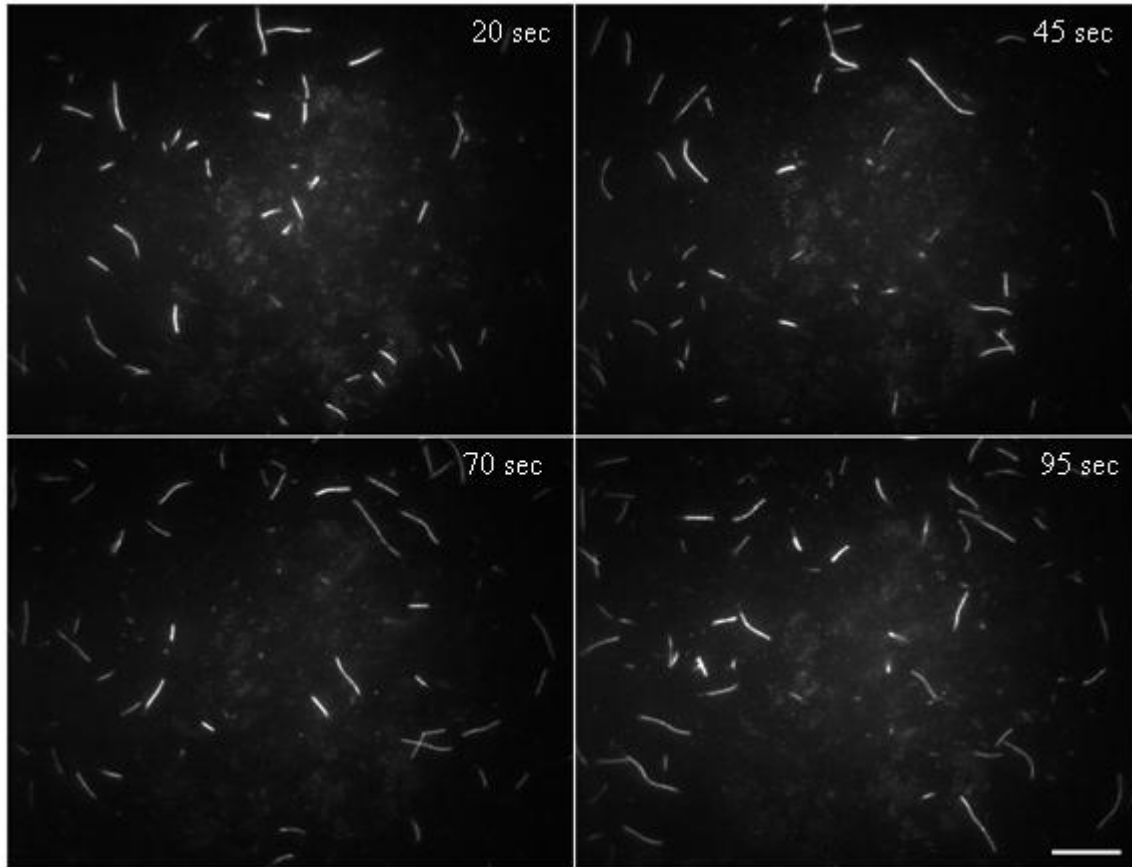


Figure 2-2. Time-lapse image of actin filaments on a BSA-stamped surface containing no pattern. Filaments did not bind to the surface, and many fluctuated into and out of the 200 nm TIRF region. The first frame is 20 seconds after the time-lapse began, which was approximately 1 to 2 minutes after polymerization was initiated (0.75 μ M actin, 30% rhodamine-labeled actin, scale bar = 10 μ m).

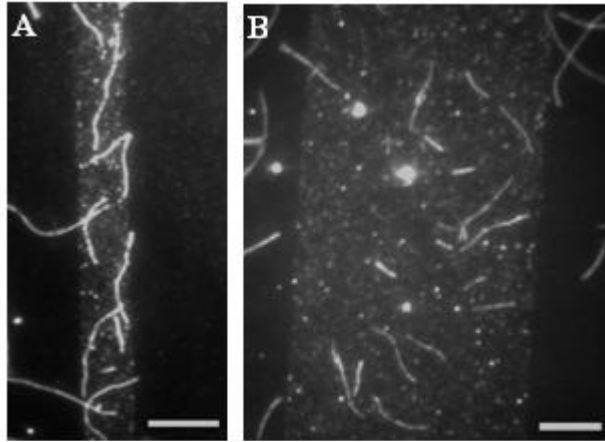


Figure 2-3. Total internal reflection fluorescence microscopy images of elongating actin filaments on NEM-myosin tracks of approximately 3.7 μm (A) and 19.5 μm (B) widths. Images were taken approximately 48 min and 22 min after initiation of polymerization, respectively (1.5 μM actin, 15% Alexa 488-labeled actin, scale bars = 5 μm).

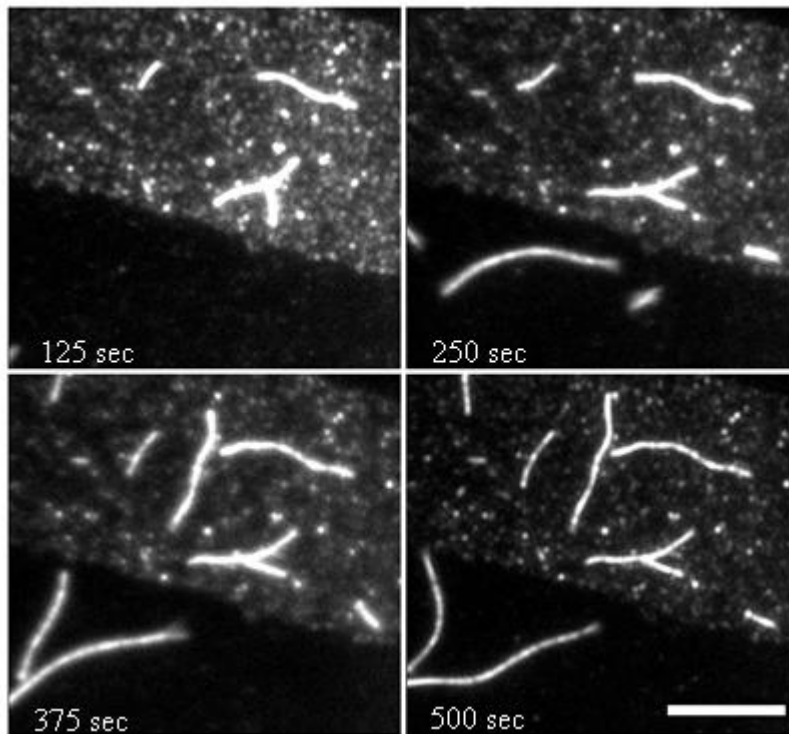


Figure 2-4. Filaments in BSA region undergo large thermal undulations compared to filaments bound to NEM-myosin region. The NEM-myosin region, located in the top half of the field-of-view as indicated by the brighter background, binds filaments to the surface as they elongate, while filaments in the BSA-passivated region (bottom half) continue to leave and enter the field-of-view, indicating that they are not bound to the surface (scale bar = 5 μm).

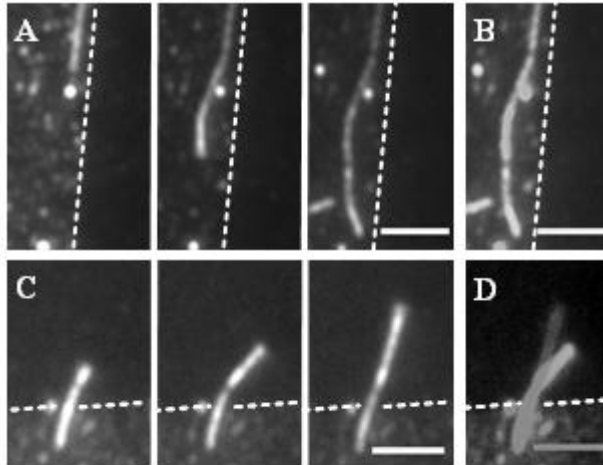


Figure 2-5. Total internal reflection fluorescence microscopy images of undulating ends of elongating filaments. A) Images from a time-lapse sequence for a filament end elongating within a NEM-myosin track (time interval = 195 sec; dashed-line indicates track edge). B) Composite of images from A, indicating small undulations away from the ultimate filament trajectory when elongating on NEM-myosin. C) Images from a time-lapse sequence for a filament elongating across the track edge and into the BSA region (time interval = 100 sec). D) Composite of images from C, indicating larger undulations of the filament end over the non-binding BSA surface (scale bars = 2 μm).

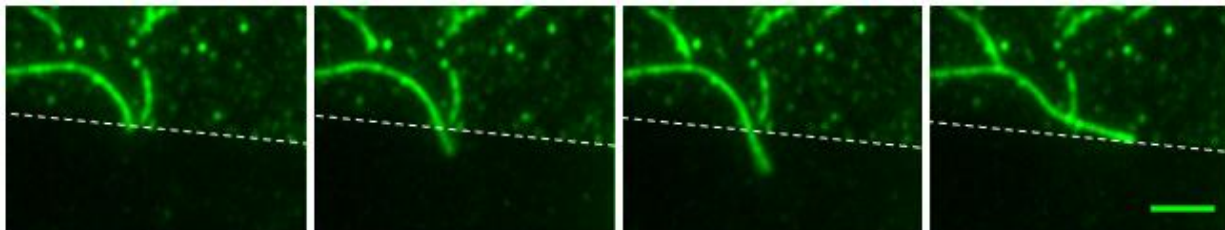


Figure 2-6. Filament elongating passed the track edge at small θ . A filament binds initially to the NEM-myosin track (top half of field-of-view) and begins to undulate, binding down as it elongates, until it eventually approaches the track edge. The filament leaves the track edge at small θ and undulates over the BSA-passivated region (bottom half). The undulations are eventually large enough that the filament encounters the NEM-myosin track and rebinds in a way that aligns the filament with the track edge (scale bar = 2 μm).

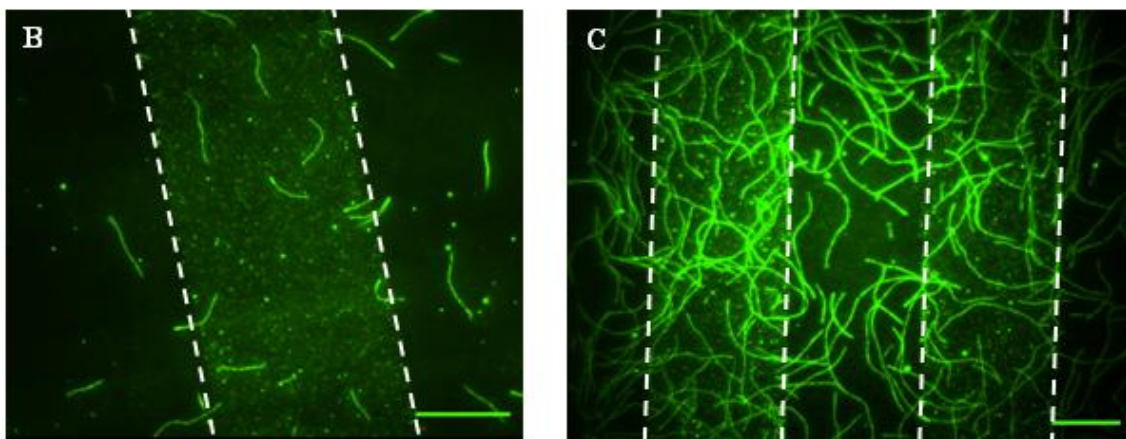
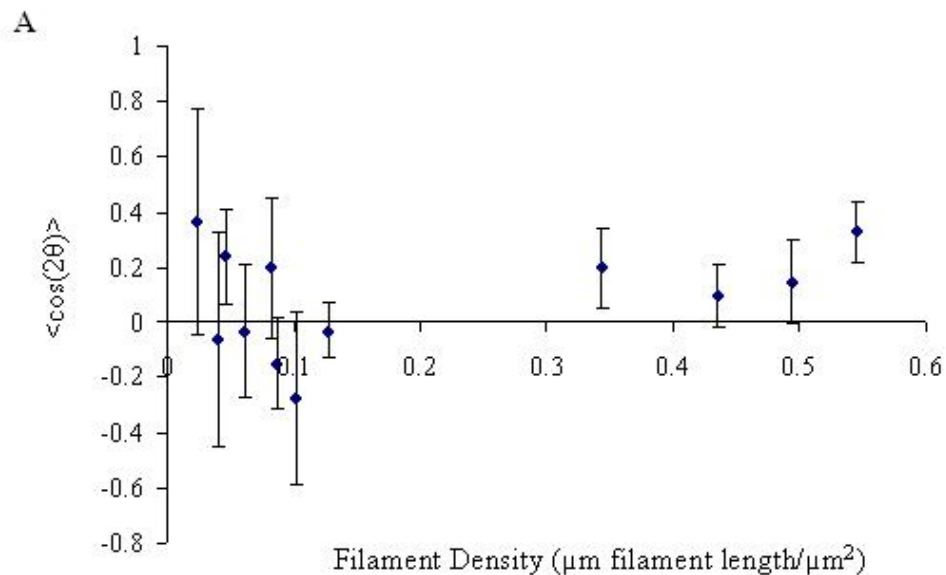


Figure 2-7. Filament alignment as a function of filament density on tracks. Each data point on the graph represents the average alignment of each field-of-view for the 20 μm wide tracks as a function of the density of all filaments within the track boundaries. Any density higher than 0.4 $\mu\text{m filament length}/\mu\text{m}^2$ was eliminated due to the potential of filament-filament interactions interfering with the alignment of the filaments on the tracks. B) A field-of-view with a low density of filaments allows observation of interactions between filaments and the modified surfaces only. C) A field-of-view with a high density of filaments (density > 0.5) inhibits analysis of the sample and may include other interactions. The tracks in the high density sample are between the first two lines and the second two lines (scale bars = 10 μm).

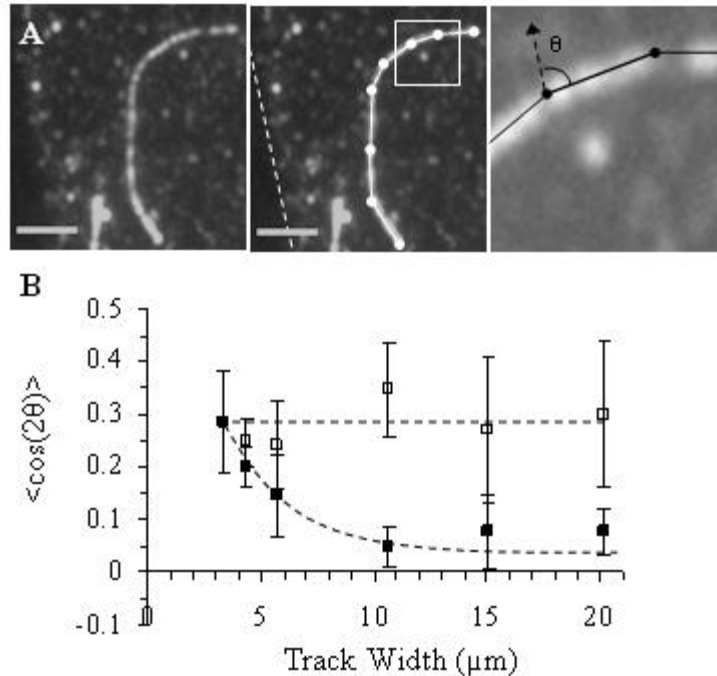


Figure 2-8. Effect of track width on filament alignment. A) Example of filament segmentation to estimate orientation angle θ with track edge. Left: Original TIRFM image; Middle: Same image showing filament segments; Right: Enlargement of boxed region in middle image showing how θ was determined for each individual segment. Scale bar = 2 μm . B) Solid squares represent the degree of filament alignment with NEM-myosin tracks versus track width. The error bars represent the weighted standard error among independent samples for each track width. Significant filament alignment was present in the three narrowest track widths (3.3 μm : $n = 16$, $p = 0.005$; 4.3 μm : $n = 36$, $p < 0.0001$; 5.7 μm : $n = 14$, $p = 0.042$; 10.7 μm : $n = 17$, $p = 0.11$; 15.1 μm : $n = 19$, $p = 0.14$; 20.2 μm : $n = 10$, $p = 0.051$). Open squares represent the alignment of filaments within approximately 1.5 μm of the track edge (4.3 μm : $n = 36$, $p < 0.0001$; 5.7 μm : $n = 14$, $p = 0.006$; 10.7 μm : $n = 14$, $p = 0.001$; 15.1 μm : $n = 13$, $p = 0.036$; 20.2 μm : $n = 7$, $p = 0.038$). C) Time-lapse sequence showing the alignment process for an elongating filament (+)-end at the track edge (scale bar = 2 μm).

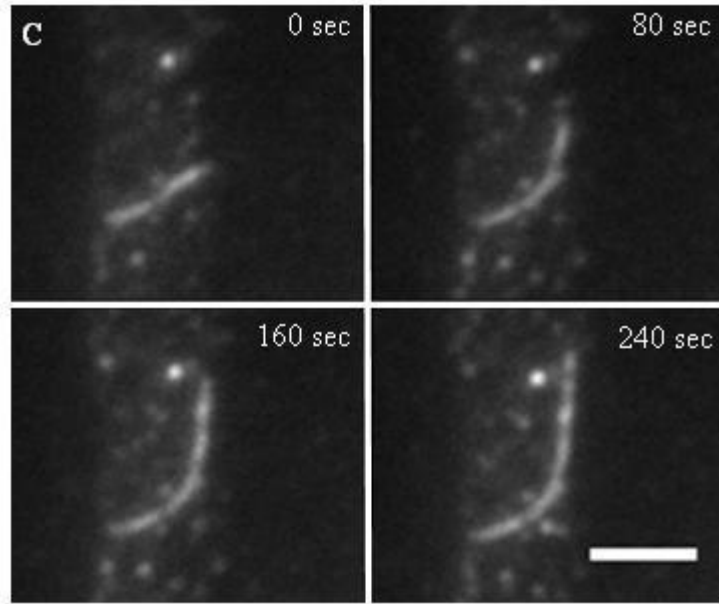


Figure 2-8. Continued

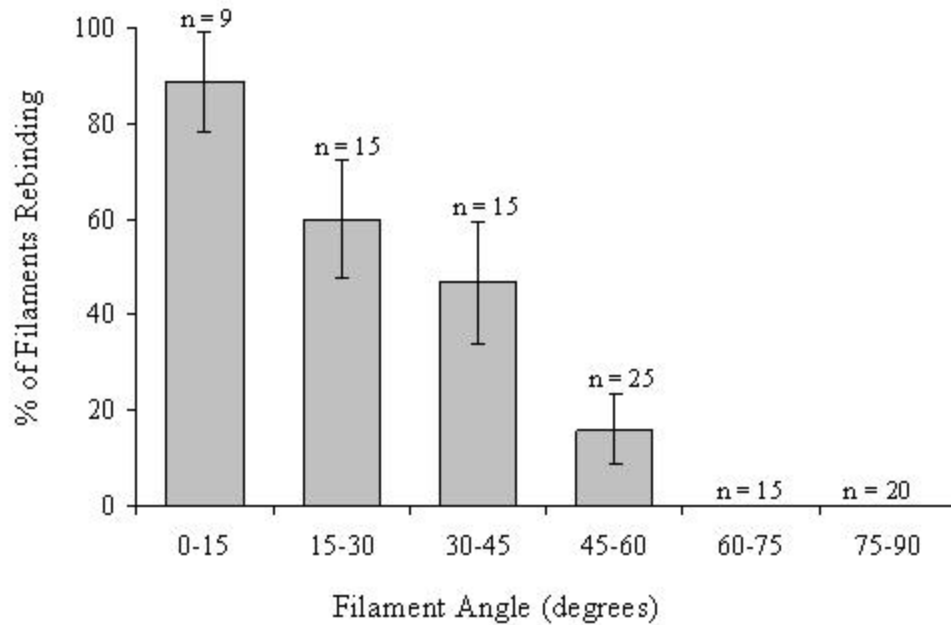


Figure 2-9. Histogram showing the fraction, f , of filament ends that rebind to tracks after their elongating ends cross track boundaries with varying initial angle of incidence with track edge. Error bars represent \pm standard error = $(f(1-f)/N)^{1/2}$, for N total filaments observed within each range of angles (105). Note: No filaments crossing the track at $\theta > 60^\circ$ were observed to rebind to the NEM-myosin track.

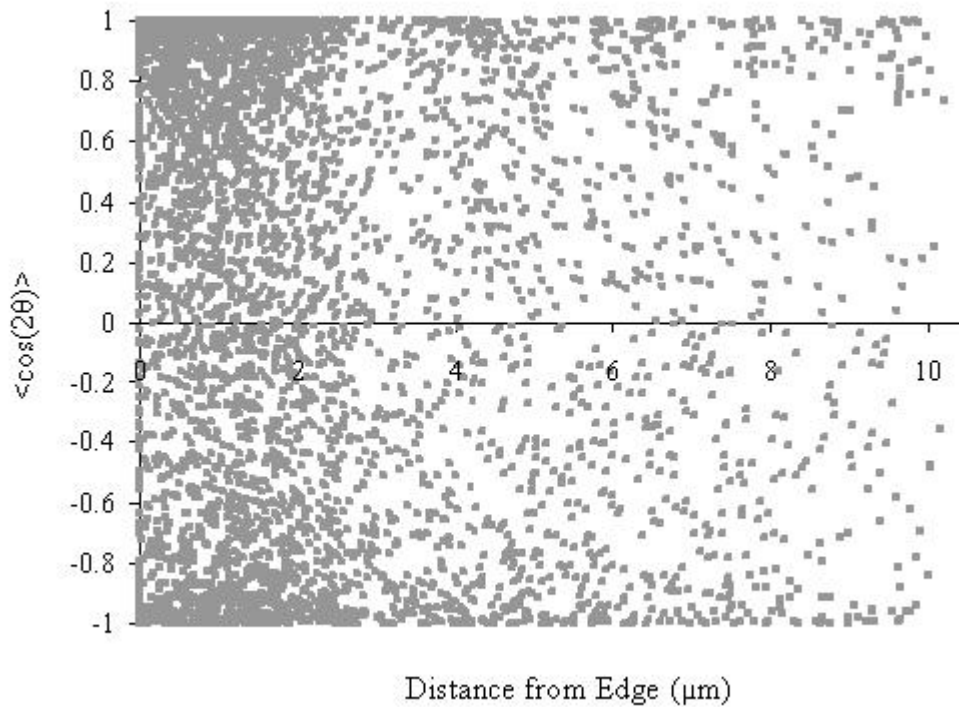


Figure 2-10. Scatter plot showing each segment alignment with the track edge as a function of the distance from the track edge. The distance of each segment was estimated by taking the midpoint of the segment and calculating its distance from the track edge. The distribution of alignment is bimodal at the edge, indicating that the filaments tend to align at the track edge if their alignment angle is sufficiently small. Note that the highest concentration of segments occurs between 0 and 3 μm of the track edge ($n = 4374$ segments for all track widths at 1 μM NEM-myosin concentration).

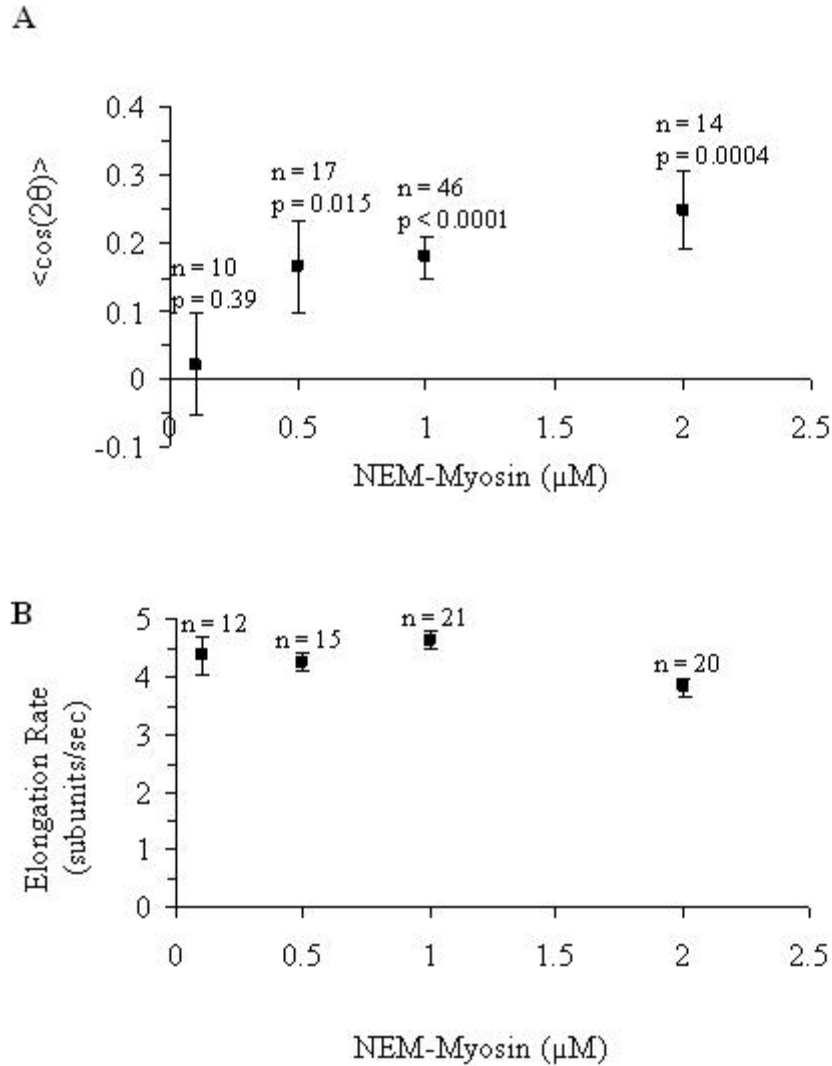


Figure 2-11. Dependence of filament alignment and elongation rate on the concentration of NEM-myosin used for microcontact printing (average track width = $4.6 \pm 0.6 \mu\text{m}$). A) Alignment appears to decrease for 0.1 μM NEM-myosin treatment condition. The error bars represent the standard error among independent samples for each myosin concentration. All treatments except 0.1 μM NEM-myosin provided significant alignment of filaments (n = number of tracks, p = one-tailed p-value). Additionally, the 2 μM and 0.1 μM samples were statistically different from each other (p = 0.021). B) Filament elongation rate is insensitive to changes in NEM-myosin concentration used in printing (0.75 μM actin, 15% rhodamine-labeled actin; n = number of filaments that instantaneous velocities were measured, p-value = 0.17 from a one-way ANOVA). The error bars represent the standard error from a least squares regression analysis.

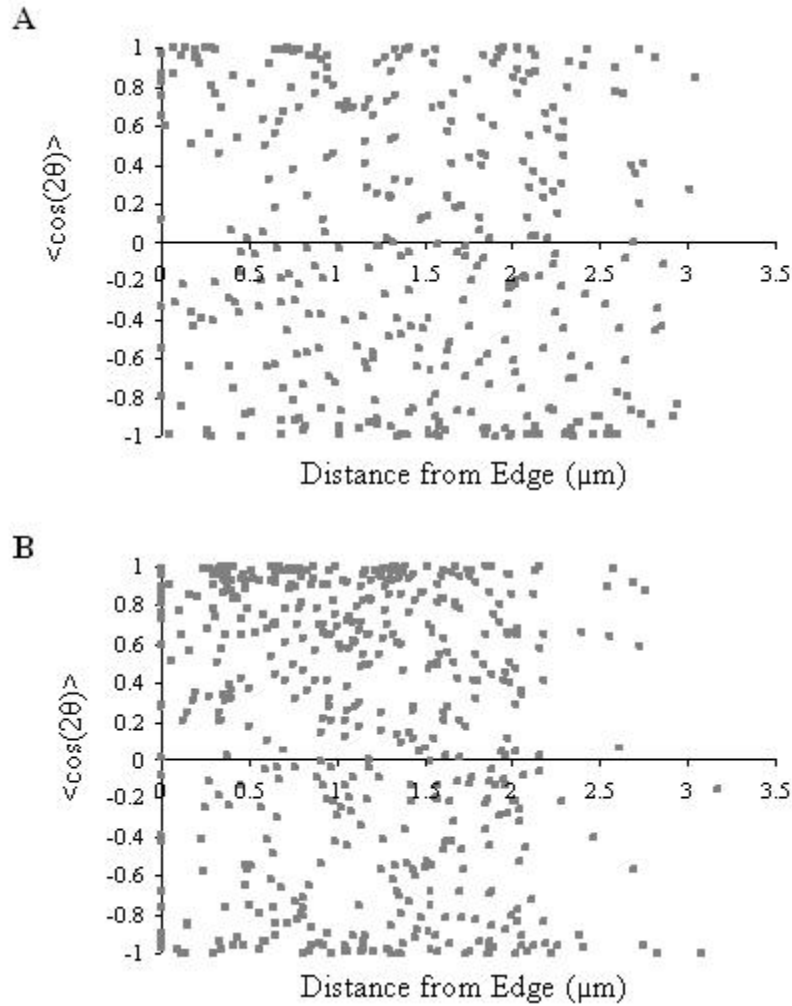


Figure 2-12. Scatter plots showing the alignment of individual filament segments (independent of length) at varying NEM-myosin concentrations as a function of the distance from the track edge. A) The 0.1 μM NEM-myosin treatment had the least number of segments, and the alignment does not seem to have a strong dependence on the edge of the track ($n = 365$ segments). B) NEM-myosin concentration of 0.5 μM has a slightly higher density of aligned filaments ($n = 524$). C) 1 μM NEM-myosin has a similar trend to Figure 2-10 ($n = 1583$). D) A majority of segments near the edge are highly aligned in the 2 μM NEM-myosin concentration sample ($n = 487$).

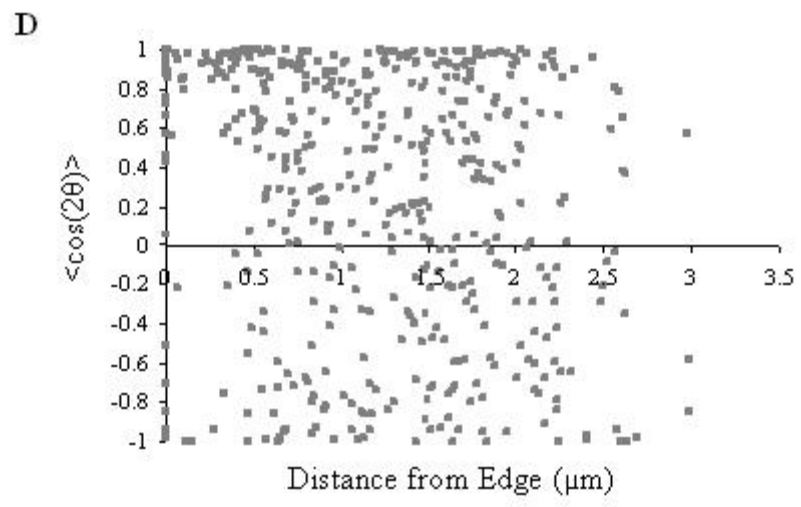
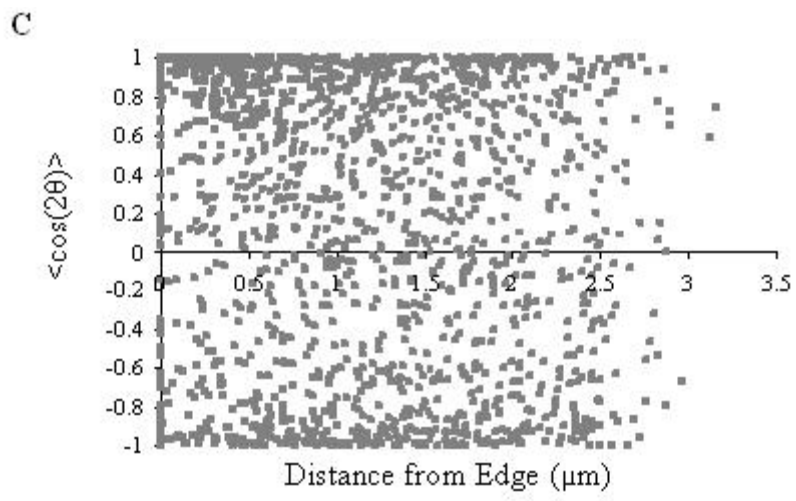


Figure 2-12. Continued

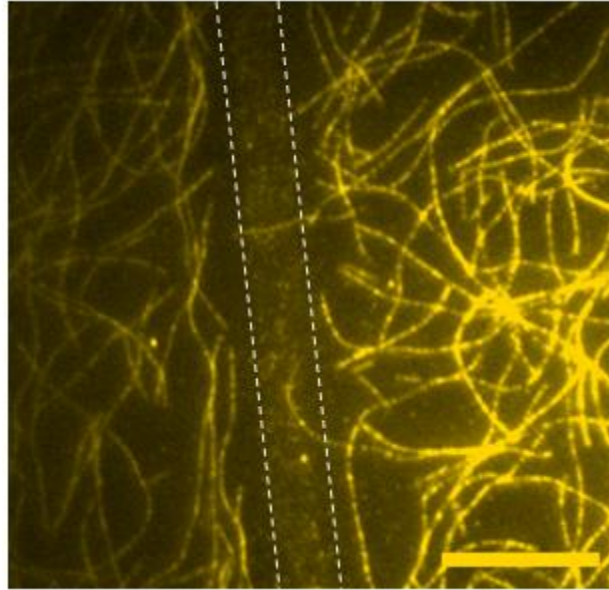


Figure 2-13. Filaments accumulate in the BSA region of the stamped surface, preventing binding from occurring in the track region. Surface stamped with 2 μM NEM-myosin treated PDMS stamp. Image taken 11.5 min after initiation of polymerization (scale bar = 10 μm).

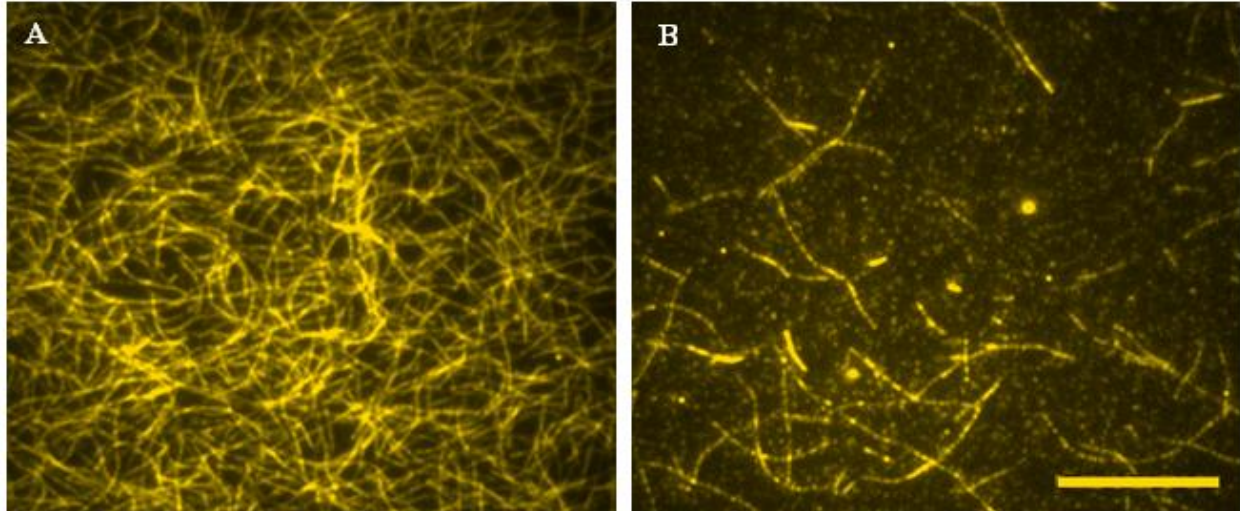


Figure 2-14. Incubation time of lyophilized rhodamine actin can help to control the density of filaments on the surface. Surfaces have been incubated with NEM-myosin for 1 min (no stamping) followed by BSA. A) Lyophilized rhodamine actin resuspended and incubated for 3 hours produces a large network of filaments within 2.5 min of polymerization. B) Resuspension and incubation of lyophilized rhodamine for 3 days before used in a polymerization assay visibly decreases the filament density on an NEM-myosin surface (time = 6.5 min). Both samples contain 1 μM actin with 15% labeled (scale bars = 10 μm).

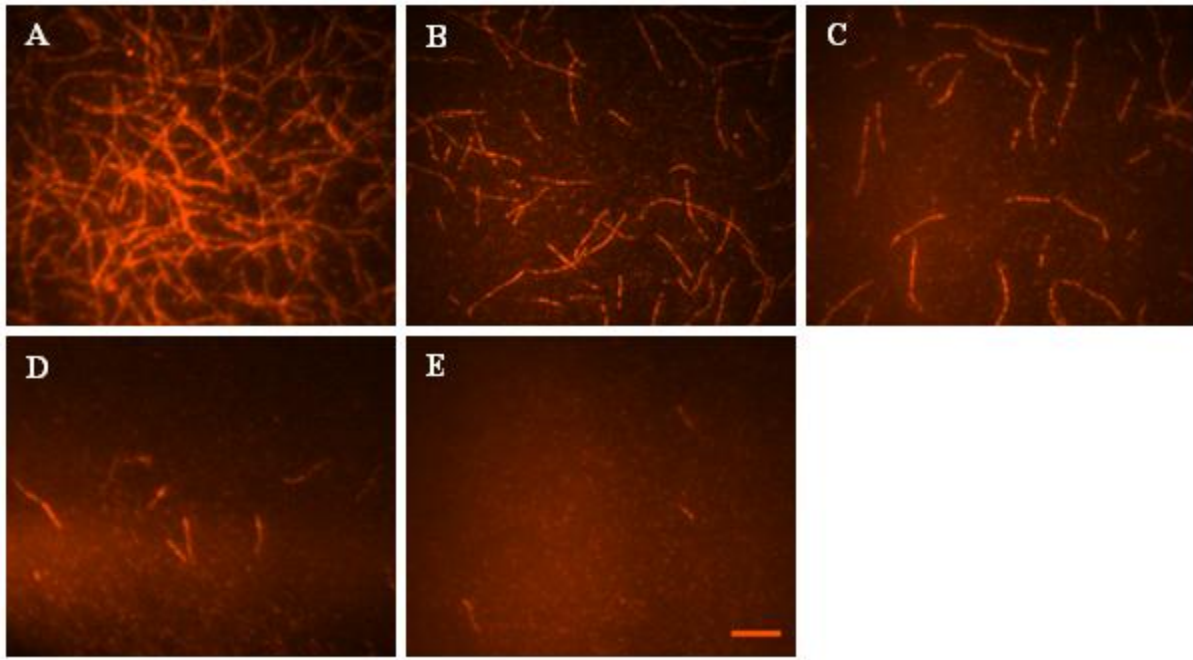


Figure 2-15. Increasing the concentration of profilin visibly decreases the density of actin filaments on NEM-myosin treated surfaces. A) 0 μM , B) 1 μM , C) 5 μM , D) 10 μM , and E) 20 μM profilin added to the polymerization assay before initiation of polymerization. Images were taken approximately 15 minutes after initiation of polymerization (scale bar = 5 μm).

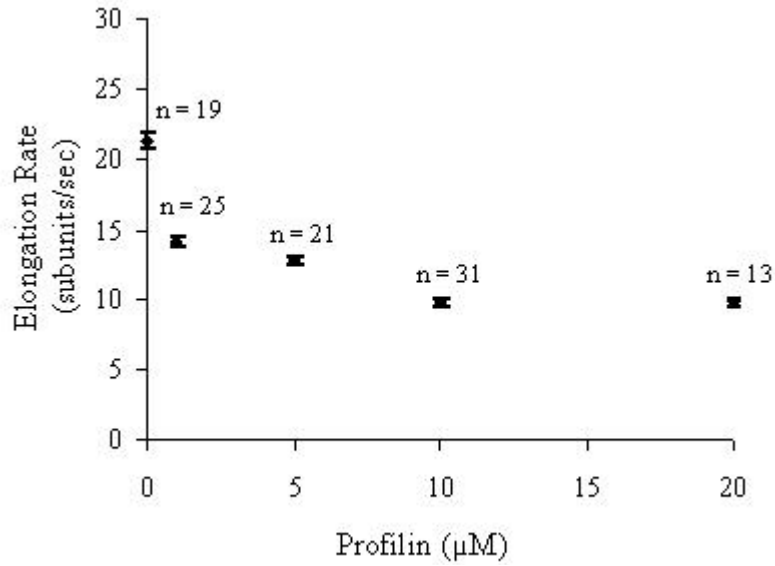


Figure 2-16. Elongation rate of actin filaments as a function of profilin concentration. Elongation rate of filaments decreases slightly with increasing profilin concentration. Error bars represent standard error based on a least squares analysis, and n refers to the number of filaments for each concentration observed. Elongation rates were obtained for each condition from a best-fit line of change in length versus change in time.

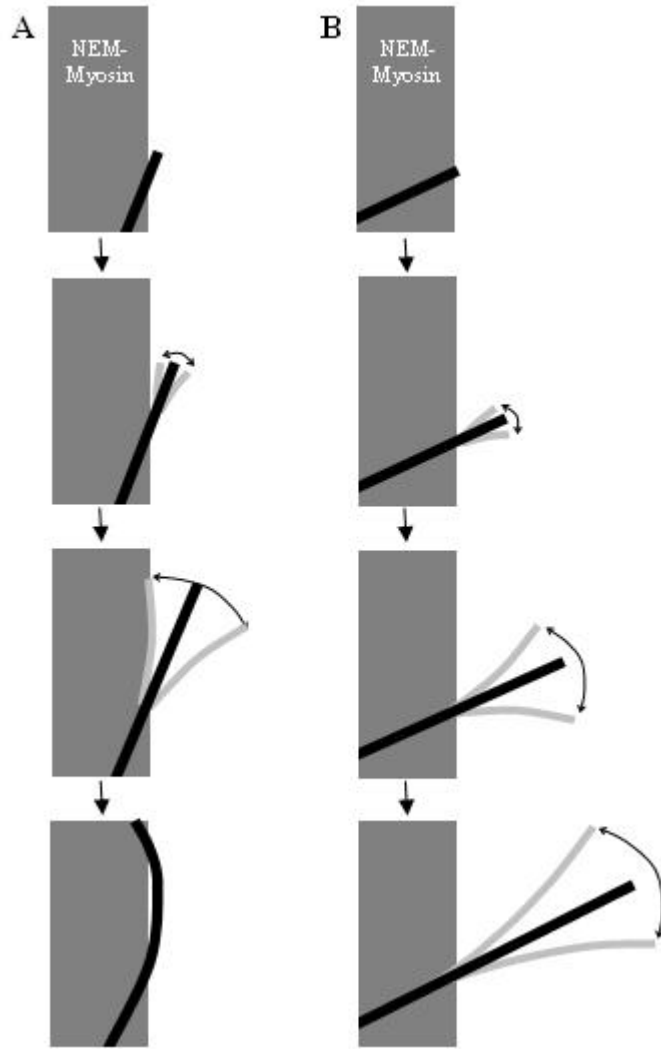


Figure 2-17. Illustration of the likely mechanism for actin filament alignment on NEM-myosin tracks. Elongating filament ends first encounter and then undulate over the track edge. The increase in filament length over the track causes larger undulations to occur. Finally, the filament either is recaptured by the track for smaller θ (A), or continues to elongate away from the track for larger θ (B).

CHAPTER 3
SIMULATING ACTIN FILAMENT ELONGATION ON MODIFIED SURFACES

3.1 Introduction

We have developed a simulation that allows us to predict the effect specific actin and surface parameters (filament length, filament persistence length, myosin surface binding probability, and patterned surface track width) have on filament alignment. These simulations complement our experimental results and aid in designing patterns to guide actin filament elongation in applications. Mathematical modeling of thermal undulations of actin filaments in solution (with both ends free) has been previously reported (49). We simulated the thermal excitations of the bending modes of the undulating unbound elongating filament end (with a fixed (-)-end) to generate realizations of the filament shape (49, 108). These simulations allowed us to examine the effects of total filament length, binding probability, and persistence length on the probability of filaments rebinding after crossing a track boundary. We further investigated the effect of NEM-myosin track width, binding probability, and persistence length on the overall alignment of filaments.

3.2 Methodology

The bending energy, E , of a filament undulating around a straight shape is used to determine the fluctuations of the filament by calculating the shape of the filament at an instantaneous point (Equation 3-1) (108).

$$E = \frac{\lambda kT}{2} \int_0^L (\theta'(s))^2 ds \quad (3-1)$$

Bending energy is a function of the persistence length of an actin filament, λ , the length of the filament segment, L , the Boltzmann constant, k , the temperature, T and the tangent angle, θ , at position s on the filament. The tangent angle can be written as a Fourier series (49), with each

mode obeying the boundary conditions: $\theta(0)=0$ (fixed end) and $\theta'(L)=0$ (free end) (Equation 3-2).

$$\theta(s) = \sum_{n=0}^N a_n \sin\left(\left(n + \frac{1}{2}\right)\pi \frac{s}{L}\right) \quad (3-2)$$

where N is the number of modes, a_n is the amplitude of the wave function for modes n . The integral of $(\theta'(s))^2$ from $s = 0$ to $s = L$ was solved for from Equation 3-2 and substituted in Equation 3-1 resulting in Equation 3-3.

$$E = \frac{\lambda k T \pi}{4L} \sum_{n=0}^{\infty} a_n^2 \left(n + \frac{1}{2}\right) = \sum_{n=0}^{\infty} E_n \quad (3-3)$$

According to the equipartition theorem, the average energy for each mode is equal to $kT/2$, allowing us to set the energy equal to this value (Equation 3-4).

$$\langle E_n \rangle = \frac{\lambda k T \pi}{4L} \left(n + \frac{1}{2}\right) \langle a_n^2 \rangle = \frac{kT}{2} \quad (3-4)$$

Rearranging Equation 3-4, we solved for the mean square amplitudes as a function of n , L and λ (Equation 3-5).

$$\langle a_n^2 \rangle = \frac{2L}{\lambda \pi \left(n + \frac{1}{2}\right)} \quad (3-5)$$

Undulations of the free end of a filament were simulated by providing random values for the amplitudes a_n from a Gaussian distribution (MATLAB function RANDN) with mean zero and variance given by Equation 3-5. The instantaneous filament tangent angles, $\theta(s)$, were then determined by substituting the generated amplitudes into Equation 3-2. The realized function $\theta(s)$ was converted into x - and y -coordinates by Equations 3-6 and 3-7.

$$\frac{\Delta x}{\Delta s} = \cos(\theta(s)) \quad (3-6)$$

$$\frac{\Delta y}{\Delta s} = \sin(\theta(s)) \quad (3-7)$$

The coordinates $x(s)$ and $y(s)$ were finally obtained by numerical integration (trapezoid rule) of Equations 3-6 and 3-7.

Elongation and binding of the filament on a filament-binding surface was simulated as follows. The free end of the filament, with the initial length taken as 0, increased in length by Δs over each time increment, Δt (unless otherwise specified, $\Delta s = 0.01 \mu\text{m}$ and $\Delta t = 1 \text{ s}$). The probability of attachment along the unbound undulating segment length was assumed uniform along the filament length and constant in time, such that the probability of binding was $K_p L \Delta t$, where the parameter K_p is the binding probability per unit length, per unit time ($\mu\text{m}^{-1} \times \text{sec}^{-1}$). Therefore, within the simulation, binding of a filament with length L occurred in time increment Δt when MATLAB function RAND, which generates uniformly distributed random numbers on $[0,1]$, generated a random number $< K_p L \Delta t$. If the filament binds, the position of binding s_1 is then determined from a uniform distribution (again using MATLAB function RAND) along the length of the free end $[0, L]$, and the resulting shape of the newly bound filament segment is assumed to be fixed and is taken as the instantaneous filament shape for that region $[0, s_1]$ (based on Equations 3-6 and 3-7). After binding, the bound position on the filament resets as $s = 0$ and L is reset to the new length of the unbound filament end.

Filaments were simulated on patterned surfaces with binding and non-binding regions by allowing binding to occur only on the filament-binding regions of the surface. The filament was assigned an initial position within the track, an initial angle between 0° and 90° , and a final total length between 1 and $16 \mu\text{m}$, all based on a random number generator (MATLAB function RAND, unless otherwise specified). In addition, the track width of the NEM-myosin, the

number of modes, the binding probability, K_p ($\mu\text{m}^{-1}\times\text{sec}^{-1}$), and the persistence length, λ (μm) was set by the user. The Appendix contains the MATLAB code with comments.

3.3 Results

3.3.1 Description of Simulated Filament Elongation

To first confirm that the simulations agree qualitatively with our experimental observations of undulating filament ends near track boundaries, we looked at the alignment of elongating filaments restricted to the track edge (see Figure 2-9 for the experimental results). Filaments were initially bound at their (-)-end 0.01 μm from the edge of the track, and the initial angle was determined to be between 0° and 90° by a random number generator in MATLAB (function RAND). The initial position of 0.01 μm from the track edge was used to ensure that filaments crossed the track edge at some point during their elongation, even at small angles. The initial angle of the filament was assumed to be the angle of incidence, or the angle at which the filament crossed the track boundary. Filaments were then set to elongate at a rate of 0.01 $\mu\text{m}/\text{sec}$.

The position of the filament (+)-end with respect to time shows the fluctuations of the filament as it was elongating (Figure 3-1). Figure 3-1A clearly shows the decrease in fluctuations of an elongating filament end due to the decrease in the length of the free filament. The position at which the decrease in fluctuations occurred corresponds to the position on the final filament where binding occurred (Figure 3-1B). Figure 3-1C shows the fluctuations of a filament that never rebinds to the track. These fluctuations continued to increase in magnitude. Figure 3-1D shows the unbound filament's instantaneous position at the end of the simulation.

We analyzed the persistence length of filaments using Equation 3-8 (48) to confirm that the measured value of the persistence length, λ , was comparable to the input value.

$$C(s_i) = \langle \cos(\theta(s_i + s_j) - \theta(s_j)) \rangle = \exp\left(\frac{-s_j}{2\lambda}\right) \quad (3-8)$$

To do so, we pooled data from 240 simulated filaments and estimated the angle between points at distances 0.01 μm apart on the filament. Because we had a large sample of filaments to analyze, we only used the case where $s_j = s_{i+1}$. We then plotted the average $\ln(\langle \cos(\theta(s_i + s_j) - \theta(s_j)) \rangle)$ versus s_j (for $s_j = 0.01$ to 2 μm) and found the slope of the best-fit line with an intercept set to 0. The calculated persistence length of approximately 12 μm ($R^2 = 0.996$), matched reasonably well to our input value of 10 μm . At a lower resolution (0.1 μm segments) with the same conditions, the persistence length for 1750 filaments was approximately 14 μm ($R^2 = 0.998$). Both of these values correspond to filament shapes calculated with 2 modes. When the number of modes was increased to 10, the persistence length was calculated (at the lower resolution) to be approximately 13.5 μm , showing little effect of the number of modes on the persistence length of the filament.

3.3.2 Probability of Filament Rebinding

From our experiments (cf. Chapter 2), we expected filaments with smaller angles of incidence to have a higher probability of rebinding to the track edge (Figure 2-9). Experimentally, many characteristics of the filaments were not constant, including the lengths of filaments, the angles that the filaments crossed the track edge, and the position of the filaments with respect to the position of the track edge. For our first set of simulations, we kept the initial filament position the same for every filament and then calculated the probability of the filament rebinding once it crossed the track edge as a function of the angle of incidence. Error bars on graphs showing the probability of rebinding were calculated as described in Figure 2-9 (\pm standard error = $(f(1-f)/N)^{1/2}$).

Figure 3-2 shows the effect of decreasing the time, Δt , of the simulation from 1 to 0.5 seconds with a constant elongation rate on the probability of the rebinding of 3.2 μm long filaments (average length of filaments for our experiments). As expected, there was little variation in the dependence of the rebinding probability on the incidence angle. The largest difference occurs between 20° and 30°, which is most likely a region of higher variability, based on the larger error bars. We next looked at the effect of the rebinding probability as a function of the number of modes used to simulate the filament shape. Figure 3-3 shows very little variation and no apparent trend between the rebinding probabilities for filaments with shapes determined by 1, 2, 3, 5 or 10 modes. For this reason, we set the number of modes to 2 for all other simulations.

Consistent with expectations, we found that the probability of rebinding increased with the final filament length (Figure 3-4A). We looked at three filament lengths representing values similar to the minimum (1.6 μm), the average (3.2 μm), and the maximum (6.4 μm) lengths from our experiments. Filaments with angles less than 70° had a chance of rebinding if they were allowed to elongate to 6.4 μm , and filaments with angles less than 30° rebound to the track 100% of the time. Similarly, filaments that were allowed to elongate 3.2 μm and 1.6 μm had a probability of rebinding to the tracks at angles of incidence less than 40° and 30°, respectively. Every filament that elongated past the track at an angle of 10° or less and was allowed to elongate 3.2 μm , rebound to the track. Each filament length had the same decreasing probability trend with increasing angle of incidence, but the final length determined at what angles the decrease of probability began and ended. Binding probabilities were similar for the 60° at 6.4 μm , 40° at 3.2 μm , and 30° at 1.6 μm filament lengths as well as at 40°, 20°, and 10°, respectively.

We also combined all of the data for all three filament lengths, which contained 300 filaments for each length, creating an average filament length of 3.7 μm for 900 total filaments (Figure 3-4B). The trend and values for the combined data is very similar to that found in our experiments. Experimentally, no filament over 60° was found to rebind. In our simulations, that value was one iteration higher at 70° , most likely due to the larger number of longer filaments in the simulations.

Variations in the binding probability constant, K_p , as expected, had somewhat of an effect on the rebinding probability (Figure 3-5). Constants of 5 and 1 $\mu\text{m}^{-1}\times\text{sec}^{-1}$ had similar results, indicating that the saturation of the NEM-myosin may occur around a K_p of 1 $\mu\text{m}^{-1}\times\text{sec}^{-1}$. In both cases, these K_p values allowed for rebinding to occur at angles less than 60° , with all filaments less than 30° rebinding every time. A K_p value of 0.5 $\mu\text{m}^{-1}\times\text{sec}^{-1}$ resulted in similar rebinding probabilities at 5 and 1 $\mu\text{m}^{-1}\times\text{sec}^{-1}$, with very slight differences (no filaments rebound between 50° and 60° , and a few filaments did not rebind between 20° and 30°).

Filament binding probability constants of 0.1 and 0.05 $\mu\text{m}^{-1}\times\text{sec}^{-1}$ had a similar effect as the other three values up to 20° to 30° , at which point the rebinding probability was significantly lower than the rebinding probability for the higher K_p values. The rebinding probability of 0.05 $\mu\text{m}^{-1}\times\text{sec}^{-1}$ also had a significantly lower rebinding probability than 0.1 $\mu\text{m}^{-1}\times\text{sec}^{-1}$ in this range. All filaments, regardless of their K_p value, had a 100% chance of rebinding if the angle was less than 10° . Finally, we looked at the effect of the persistence length of the filaments on the rebinding probability (Figure 3-6). As expected, the rebinding probability decreased as the persistence length increased, indicating that the rebinding probability is directly affected by the stiffness of the filament.

3.3.3 Alignment of Filaments

In our next set of simulations, we varied the track width, allowing the filaments to be initially placed in a random position within the track. Similar to our experimental results, increasing the track width decreased the alignment of the filaments (Figure 3-7). We once again varied the number of modes to make sure that two modes were sufficient. We found that the number of modes had no effect on the alignment of the filaments as a function of track width (Figure 3-7A). Figure 3-7B shows that filaments within 1.5 μm of the track edge have a higher average alignment than the average alignment of all filaments. This is in agreement with our experimental findings (Figure 2-8B).

This alignment does decrease slightly with track width due to a combination of effects. First, the same number of filaments were tested for each track width ($n = 1000$) and their initial positions were evenly distributed within the track. Therefore, the fraction of filaments with initial positions within 1.5 μm of the edge decreases as the track width increases. In addition, as the track width increases, filaments that elongate to 1.5 μm within the edge must have decreasing alignments to reach the edge with lengths between 1 and 16 μm . Filaments must have a component perpendicular to the track edge, and the only way for filaments to reach the edge as the track width increases without increasing the final length is to decrease their alignment with the edge of the track. Once again, these results show no dependence of alignment on the number of modes.

Next, we varied the binding probability constant, K_p , between values of 0.001 and $1 \mu\text{m}^{-1} \times \text{sec}^{-1}$ and found no dependence on the overall trend or values of the alignment as a function of track width (Figure 3-8). This indicated that K_p did not have an affect on the alignment at these values, which may correspond to our experimental values above 0.5 μM NEM-myosin (Figure 2-11A). Furthermore, the actual persistence length of bound filaments did

not depend on K_p , with estimated values ranging from 13.3 to 14.9 μm with no apparent trend. These values were comparable to the persistence length calculated for the same discretization resolution with no binding (14 μm), further indicating that binding did not affect the persistence of bound filaments. .

We next looked at even lower values of K_p (0.0005 and 0.0001 $\mu\text{m}^{-1}\times\text{sec}^{-1}$) for a track width of 4 μm to compare to our experimental analysis (Figure 3-9). We found that the alignment began to decrease for these K_p values. The difference between the alignment for K_p values of 0.001 and 0.0001 $\mu\text{m}^{-1}\times\text{sec}^{-1}$ is comparable to the difference between the values of alignment for 0.1 and 0.5 μM NEM-myosin in Figure 2-8A. However, in our simulations, filaments were more aligned than in our experiments. We also observed a decrease in alignment at higher K_p values (0.01, 0.1 and 1 $\mu\text{m}^{-1}\times\text{sec}^{-1}$). At these K_p values, the probability of rebinding to the tracks is high, however, once bound, the filaments may bind too often to fluctuate and realign with the track edge, causing the alignment to decrease. Experimentally, we may not have seen binding probabilities this high. In addition, we may have reached surface saturation, a factor that was not taken into account in our simulations. We also determined that the persistence length of the filament (Figure 3-10) had little effect on the alignment of filaments as a function of track width. Slight differences between the alignments of filaments with varying persistence lengths at lower track widths allude to a decrease in alignment with an increase in persistence length.

3.4 Discussion

Our simulations have aided in interpreting our experimental results and in confirming the microcontact printing as a means to guiding elongating actin filaments. The simulations also provide a useful tool for designing patterns and experimental conditions for optimal filament guidance. Furthermore, our simulation can be applied to other types of filaments, bundles of

filaments, and filaments with attached particles. We have replicated the experiments from Chapter 2 and have determined further parameters and limitations of the system. Filament lengths, NEM-myosin surface density, and persistence length, in addition to the angle of incidence, affect the probability of a filament rebinding to the edge of the track.

Specifically, longer filaments have a higher probability of rebinding and also rebind with higher angles of incidence. As we expected through our mechanism based on experimental data and as our simulation confirmed, as the filament increases in length (passed the track edge), its probability of rebinding, which is based on length, increases. For this reason, in applications, it is important to control the length of the filaments. With fewer filaments, each with greater length, alignment may be increased.

Also, as expected, the higher binding probability constants cause the rebinding probability to increase, but only within a certain range of incidence angles. As found with our experiments, there is a surface saturation point, and we found this in our simulations that recreated the rebinding probability, with little difference between 0.5, 1 and $5 \mu\text{m}^{-1} \times \text{sec}^{-1}$. This lack of effect on filament alignment suggests that the angle of incidence and the final filament length have a stronger effect on the probability of rebinding than the density of molecules on the surface. If a filament leaves the track at an angle greater than 70° , the persistence length of the filament limits the filament's ability to bend enough to sample the NEM-myosin track surface. If a filament is too short, it also may not have enough energy to bend back to the track.

Figure 3-5 shows that the only angles of incidences that are affected by the binding probability constant were in the range between 20° and 40° (persistence length = $10 \mu\text{m}$, total filament length = $3.2 \mu\text{m}$). This small range of angles may explain why the binding probability had little effect on the overall alignment of filaments evenly distributed over the entire track

width. These results support our mechanism proposed in Chapter 2, indicating that the filament thermal undulations are responsible for the alignment of the filaments on binding tracks, and that only very low surface densities will affect the rebinding and alignment of filaments. Figure 3-9 demonstrates that at K_p values on the order of $10^{-4} \mu\text{m}^{-1}\times\text{sec}^{-1}$, small effects are seen on the overall alignment of the filaments.

We were also able to vary the persistence length of filaments and study the effect on filament alignment. Filaments with longer persistence lengths were less likely to rebind at higher angles due to the decrease in the magnitude of their fluctuations. However, filaments with longer persistence lengths had slightly higher overall alignments on tracks with smaller widths ($< 10 \mu\text{m}$). Therefore, in applications with filaments for longer persistence lengths, a filament with a small initial angle will elongate with little changes in the alignment. However, if this filament leaves the track edge, it has less of a chance of rebinding to the track. Filaments with short persistence lengths may not align with the track edge, but may follow the track by continuing to cross the track edge and rebind, even though elongation itself on the track is less aligned.

We also determined that the surface does not affect the persistence length of bound filaments, indicating that the surface density did not alter the filament shape. This result is consistent with the experimental observation that the estimated measured persistence length of bound filaments did not vary significantly with the myosin density ($\lambda = 21.3 \mu\text{m}$ for $0.1 \mu\text{M}$ NEM-myosin, $15.7 \mu\text{m}$ for $0.5 \mu\text{M}$, $14.6 \mu\text{m}$ for $1 \mu\text{M}$, and $17.2 \mu\text{m}$, for $2 \mu\text{M}$). Therefore, we assume that the NEM-myosin surfaces lock the filaments into shapes that are generated by the thermal fluctuations of the filaments themselves.

Differences between experimental results and simulated results may be explained by the lack of certain conditions in the simulation. One of these factors includes the interaction between filaments, which we have not taken into account. Our simulations test one filament on a track, whereas our experiments contained many filaments per track. Experimentally, we eliminated surfaces that contained a high density of actin filaments. However, we could not completely eliminate filament interactions. Filaments may block each other from following paths that may be predicted for a single filament elongating on a track.

In addition, we did not account for any variations in the tracks of the filaments, including the possibility of diffusion of NEM-myosin monomers from the printed region of the surface to the unprinted regions. Binding of filaments by these diffused NEM-myosin molecules may cause filaments that would have normally bent back to rebind to the tracks to remain in the unpatterned region, therefore decreasing the rebinding probability. In our simulations, we assumed evenly distributed initial binding positions of filaments within the entire track, as well as evenly distributed initial filament angles. Experimentally, microcontact printing may cause slight variations of NEM-myosin surface density or activity, causing a less even distribution of filaments.

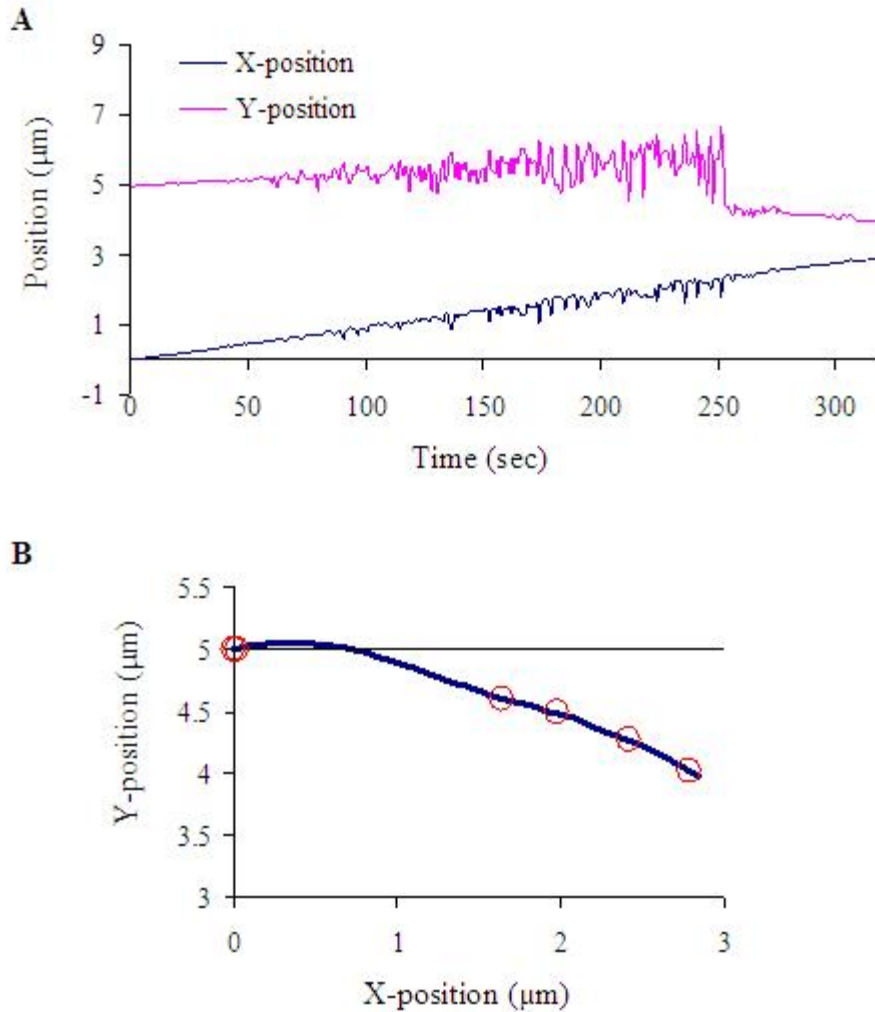


Figure 3-1. The x- and y-positions of elongating filament ends as a function of time. A) A filament leaving the track edge at a small angle eventually rebinds, as indicated by the decrease in fluctuations around 250 seconds. The initial angle of this filament was 19° . B) The final instantaneous shape of the $3.2\text{-}\mu\text{m}$ long actin filament from A. The thick blue line is the filament, the red circles represent binding of the filament to the surface, and the light black line at $y = 5$ is the track edge. C) A filament leaving the track at a large angle does not rebound. Fluctuations are larger in the x-direction because the filament is elongating almost parallel to the y-axis. The initial angle of this filament was 79° . Fluctuations continue to increase with time. D) The final shape of the $3.2\text{-}\mu\text{m}$ long actin filament from C. For both filaments, the initial position was set to $x = 0$ and $y = 4.99$ ($K_p = 0.1 \mu\text{m}^{-1}\times\text{sec}^{-1}$, $n = 2$, $\lambda = 10 \mu\text{m}$).

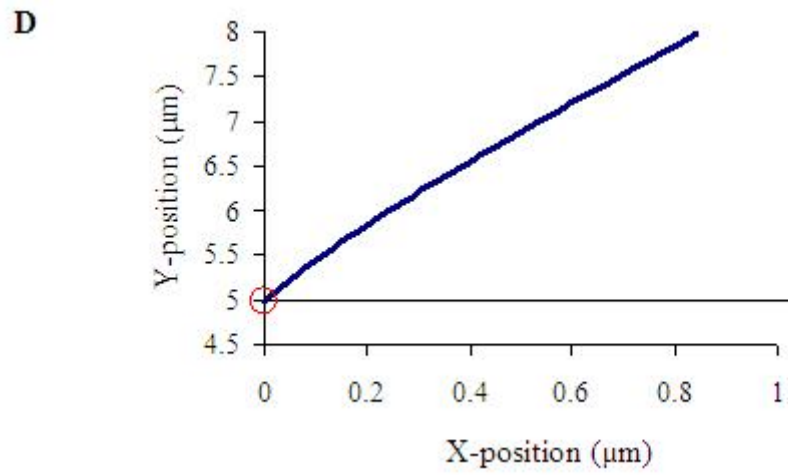
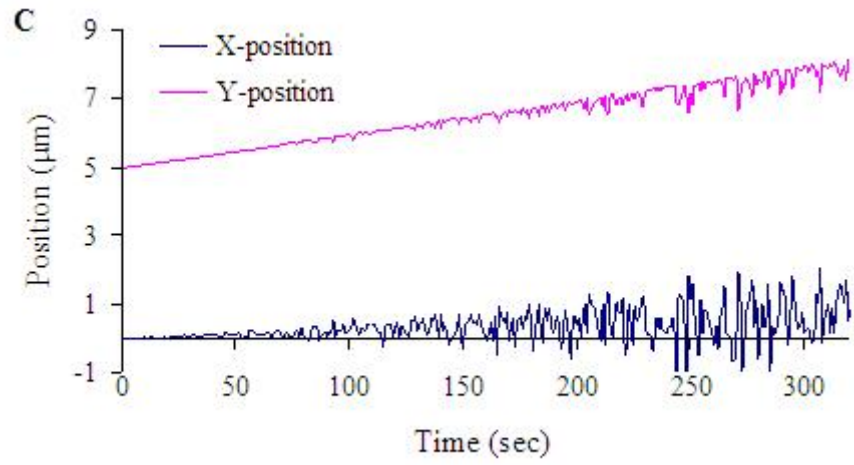


Figure 3-1. Continued

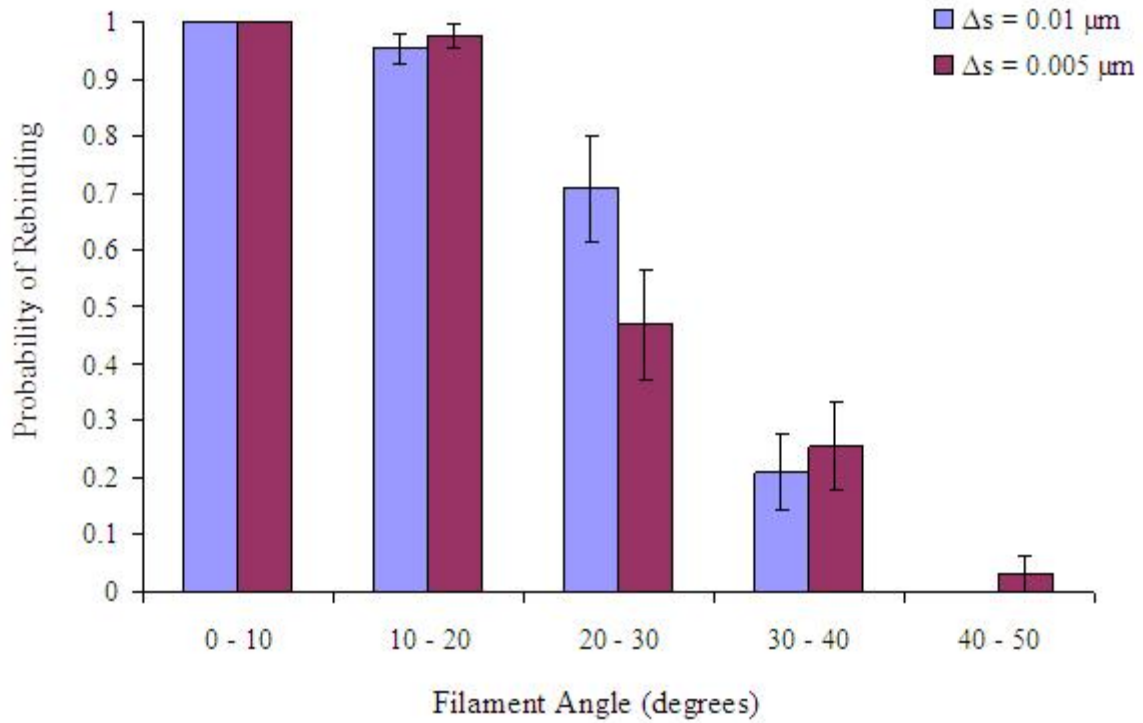


Figure 3-2. Effect of change in length (step-size of simulation) on the filament rebinding probability. Results were approximately the same for both values of Δs , indicating that the step-size has little effect on the rebinding probability ($K_p = 0.1 \mu\text{m}^{-1} \times \text{sec}^{-1}$, $n = 2$, $\lambda = 10 \mu\text{m}$, total length = $3.2 \mu\text{m}$). Note that for $\Delta s = 0.01 \mu\text{m}$, $\Delta t = 1 \text{ sec}$, and for $\Delta s = 0.0005 \mu\text{m}$, $\Delta t = 0.5 \text{ sec}$, therefore keeping the elongation rate of the filaments constant.

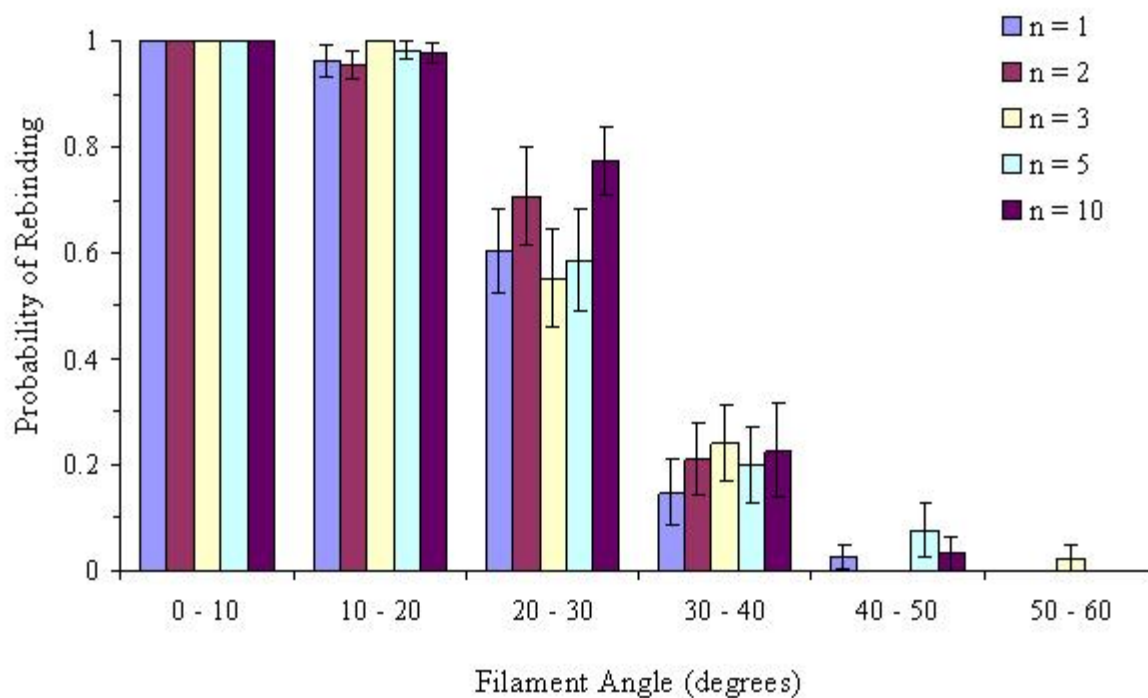


Figure 3-3. Effect of the number of modes on filament rebinding probability. For each mode, 300 filaments were analyzed. The trend and values for all modes were similar, indicating little effect of the number of modes on the rebinding probability ($K_p = 0.1 \mu\text{m}^{-1} \times \text{sec}^{-1}$, $\lambda = 10 \mu\text{m}$, total length = $3.2 \mu\text{m}$).

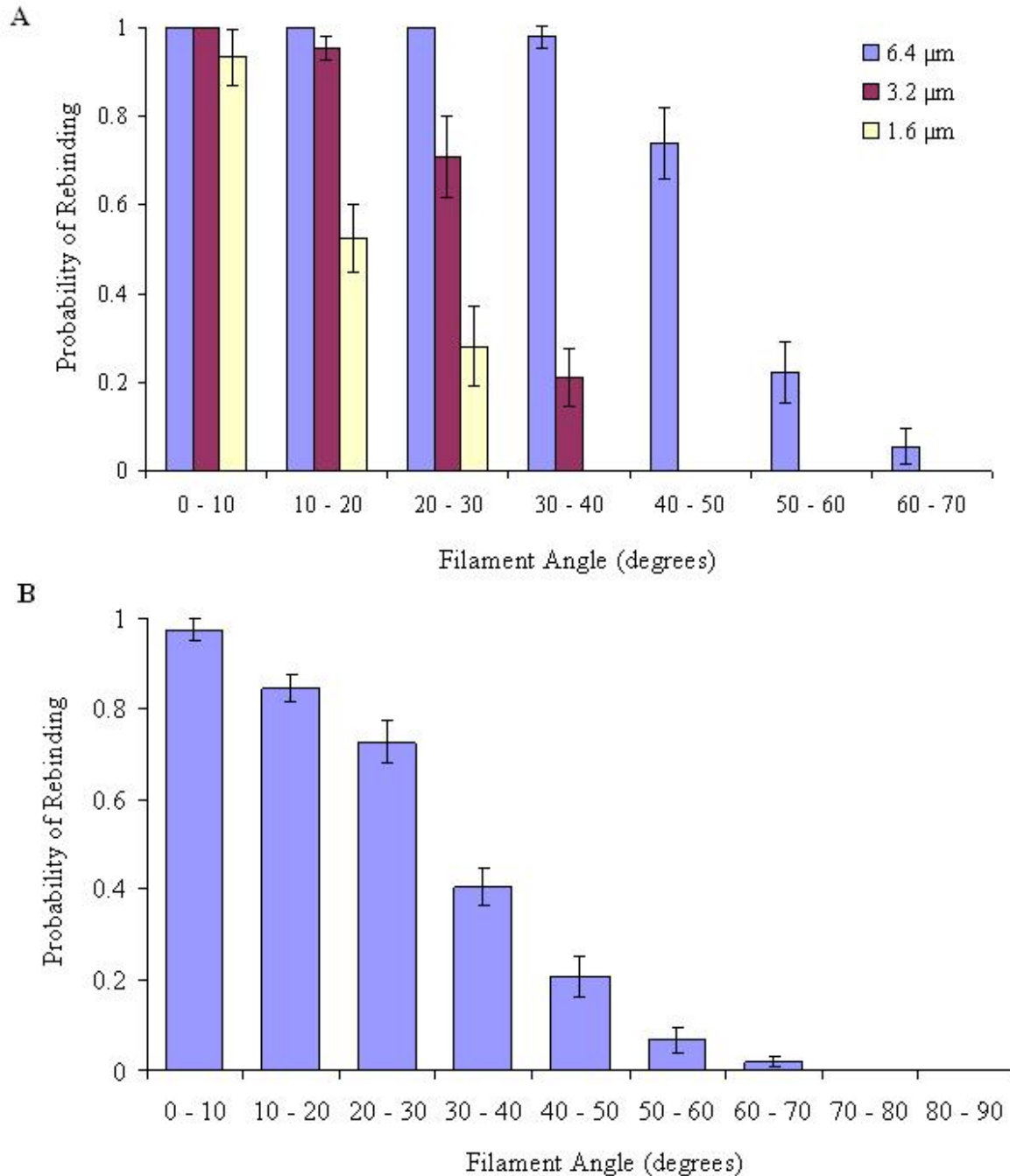


Figure 3-4. Effect of total filament length on filament rebinding probability. A) For each length, 300 filaments were analyzed. The filament angles refer to the initial angles assigned to each filament at the start of the simulation, which correspond to the angle at which the filaments crossed the track edge, or the angle of incidence. The trend for all lengths are the same, however, the rebinding probability of the longer filaments began to decrease at a higher angle of incidence. B) The filament lengths from A were combined for an average filament length of 3.7 μm ($K_p = 0.1 \mu\text{m}^{-1} \times \text{sec}^{-1}$, $n = 2$, $\lambda = 10 \mu\text{m}$).

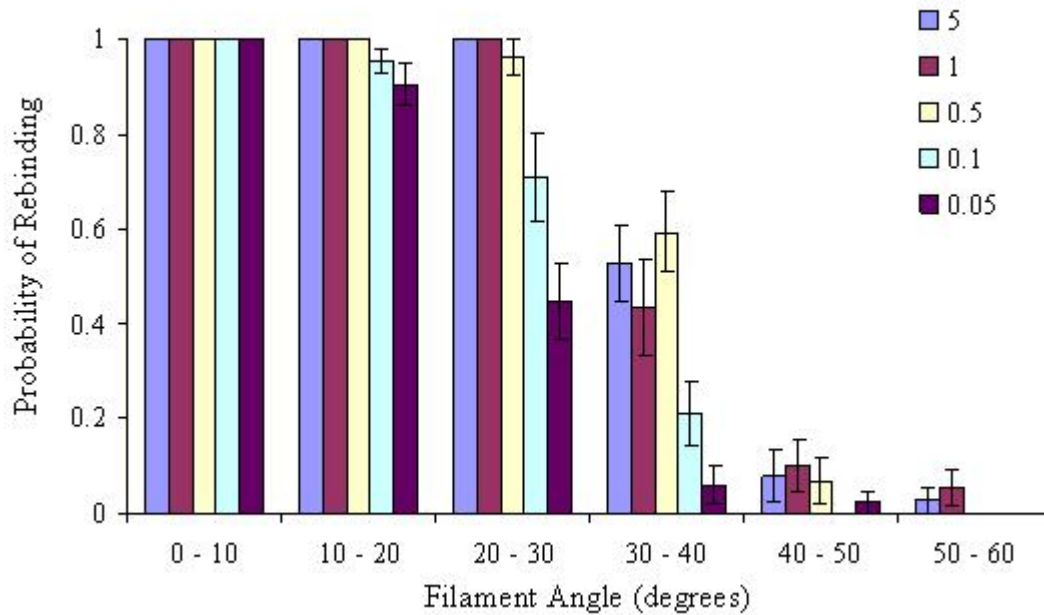


Figure 3-5. Effect of binding probability constant, K_p ($\mu\text{m}^{-1}\times\text{sec}^{-1}$), on filament rebinding probability. For each K_p value (0.05, 0.1, 0.5, 1, and 5 $\mu\text{m}^{-1}\times\text{sec}^{-1}$), 300 filaments were analyzed. The filament rebinding probability was unaffected by the binding probability constant except for filaments crossing the track edge between 20° and 40°. Within this range, the higher K_p values (0.5, 1 and 5 $\mu\text{m}^{-1}\times\text{sec}^{-1}$) had similar rebinding probabilities, while the rebinding probability decreased for both K_p values of 0.1 and 0.05 $\mu\text{m}^{-1}\times\text{sec}^{-1}$ ($n = 2$, $\lambda = 10 \mu\text{m}$, total length = 3.2 μm).

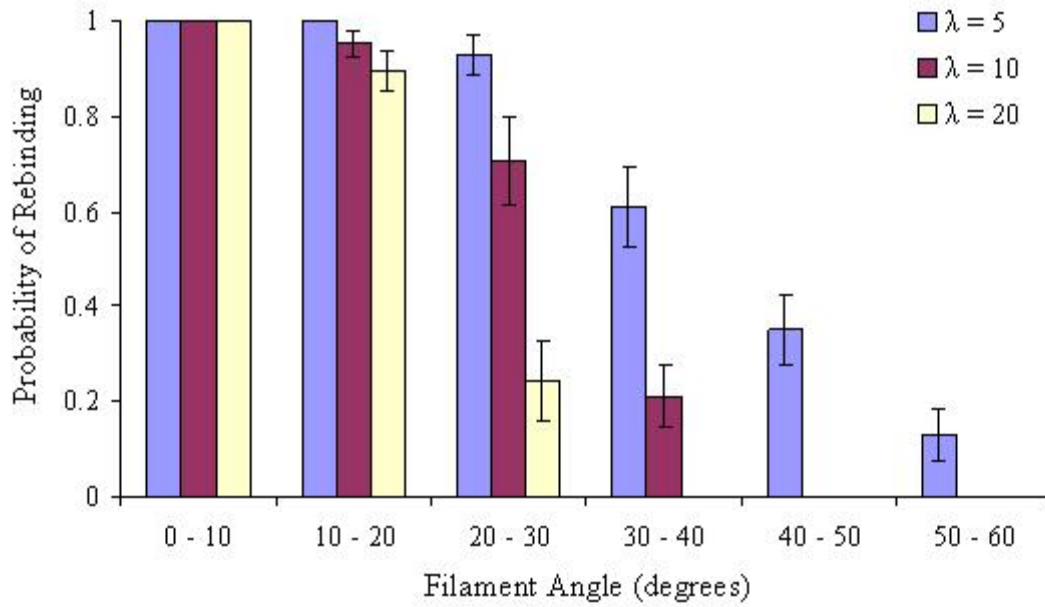


Figure 3-6. Effect of persistence length on filament rebinding probability. For each λ , 300 filaments were analyzed. As the persistence length increased, the filament rebinding probability decreased at angles above 10° ($K_p = 0.1 \mu\text{m}^{-1} \times \text{sec}^{-1}$, $n = 2$, total length = $3.2 \mu\text{m}$).

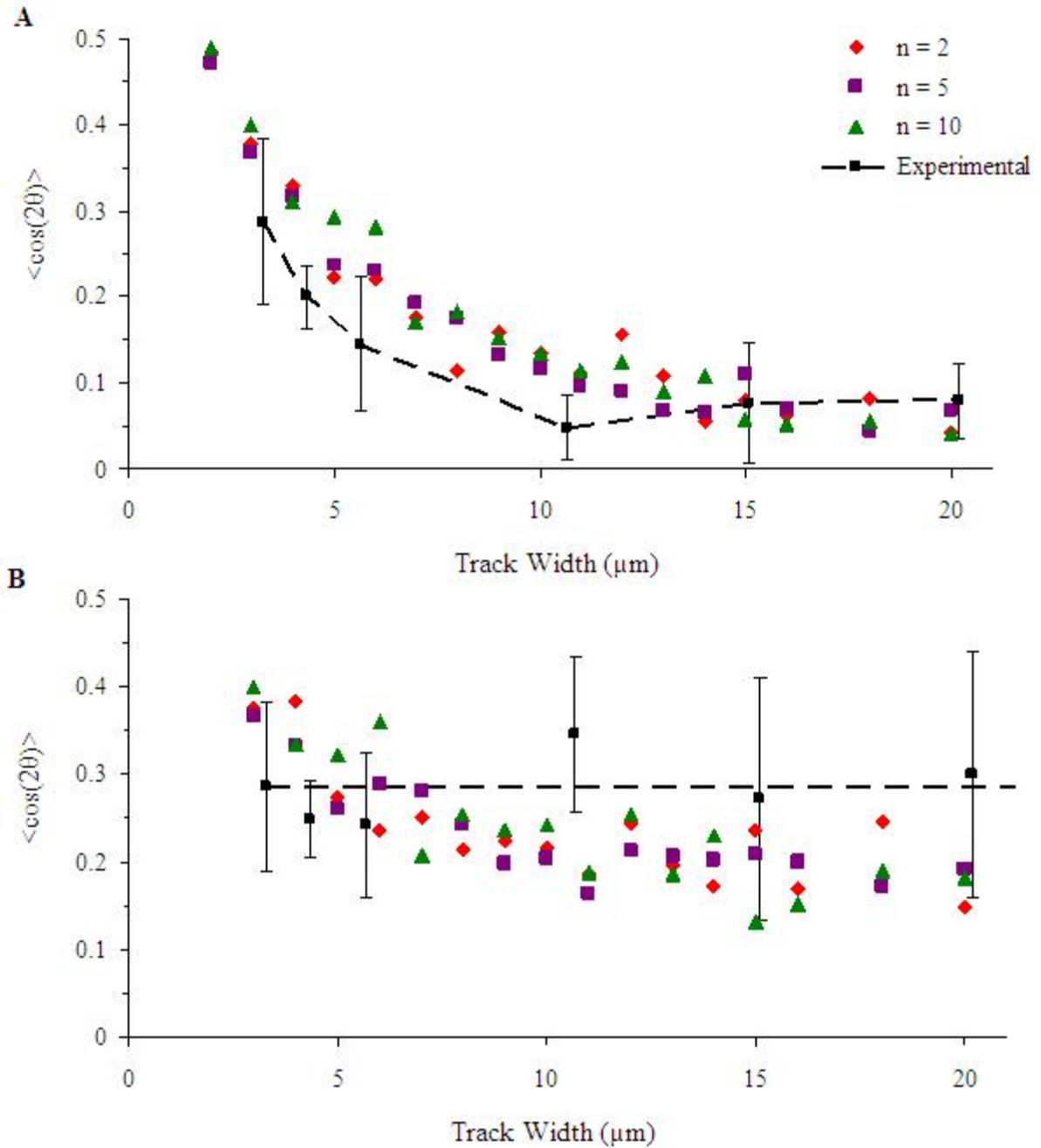


Figure 3-7. Effect of track width and number of modes on the alignment of filaments. A) The simulation produced the same trend found experimentally, with no dependence on the number of modes. B) Effect of the track edge on the alignment of filaments. Only filaments or parts of filaments within 1.5 μm of the edge of the track were included in the calculation of the alignment. The values are mostly within the error bars of the experimental data, with a slight decrease in alignment as the track width increases. The number of modes did not effect the alignment of filaments.

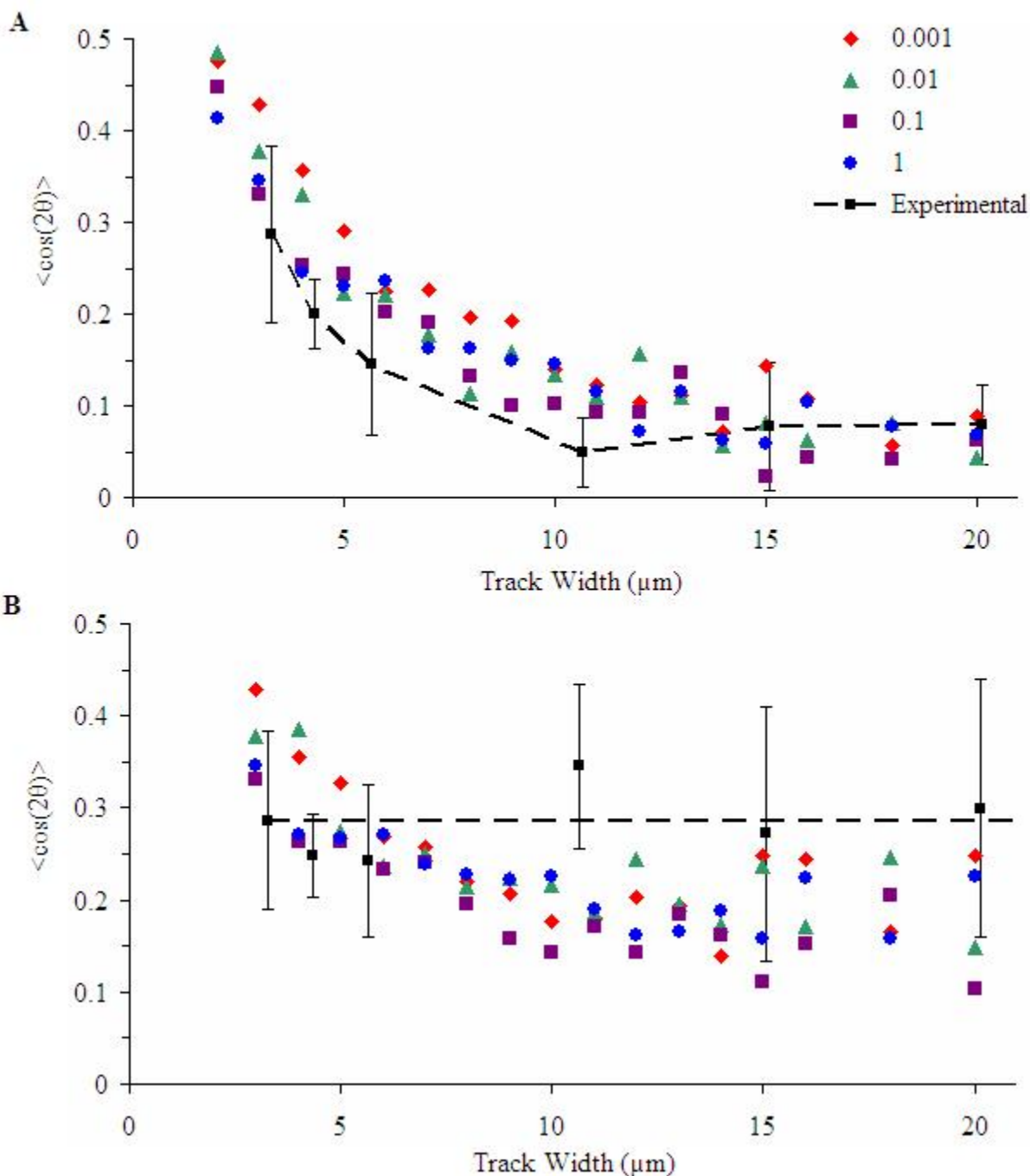


Figure 3-8. Effect of track width and binding probability constant on the alignment of filaments. A) The simulation produced the same trend found experimentally, with little dependence of alignment on the binding probability constant, K_p . B) Effect of the track edge on the alignment of filaments. Only filaments or parts of filaments within $1.5 \mu\text{m}$ of the edge of the track were included in the calculation of the alignment. The results are similar to 3-7A, with little dependence of the alignment on K_p ($n = 2$, $\lambda = 10 \mu\text{m}$).

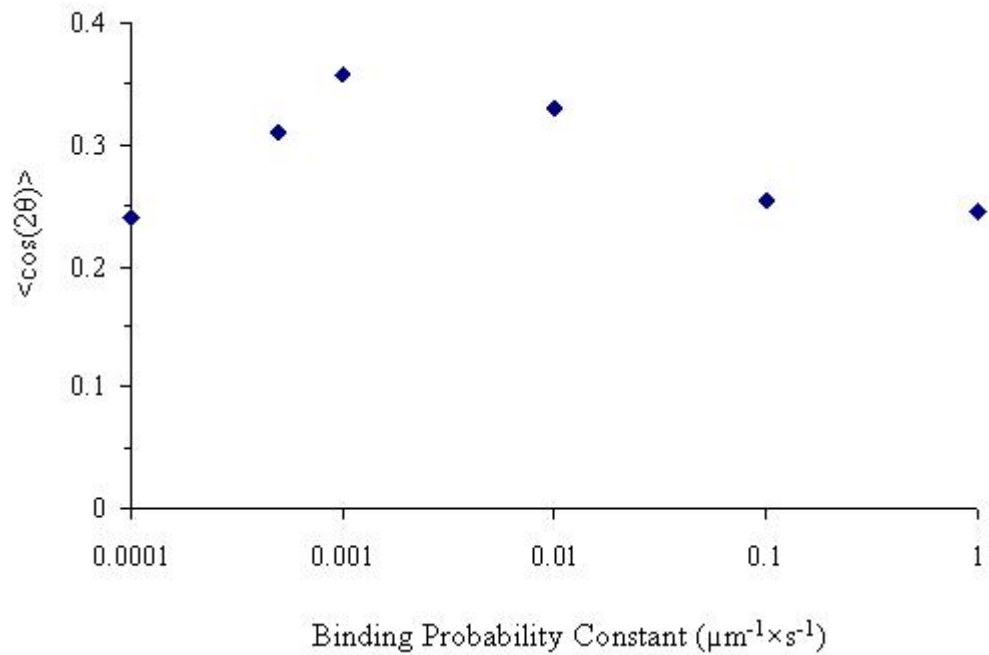


Figure 3-9. Effect of binding probability on the alignment of filaments. The alignment of filaments begins to decrease at binding probabilities with magnitudes of $10^{-4} \mu\text{m}^{-1} \times \text{sec}^{-1}$. This implies that not enough binding occurs to rebind filaments once they leave the edge of the track. The decrease at higher K_p values may indicate too much binding, resulting in a decrease of filament fluctuations and the subsequent decrease of alignment (track width = $4 \mu\text{m}$, $n = 2$, $\lambda = 10 \mu\text{m}$).

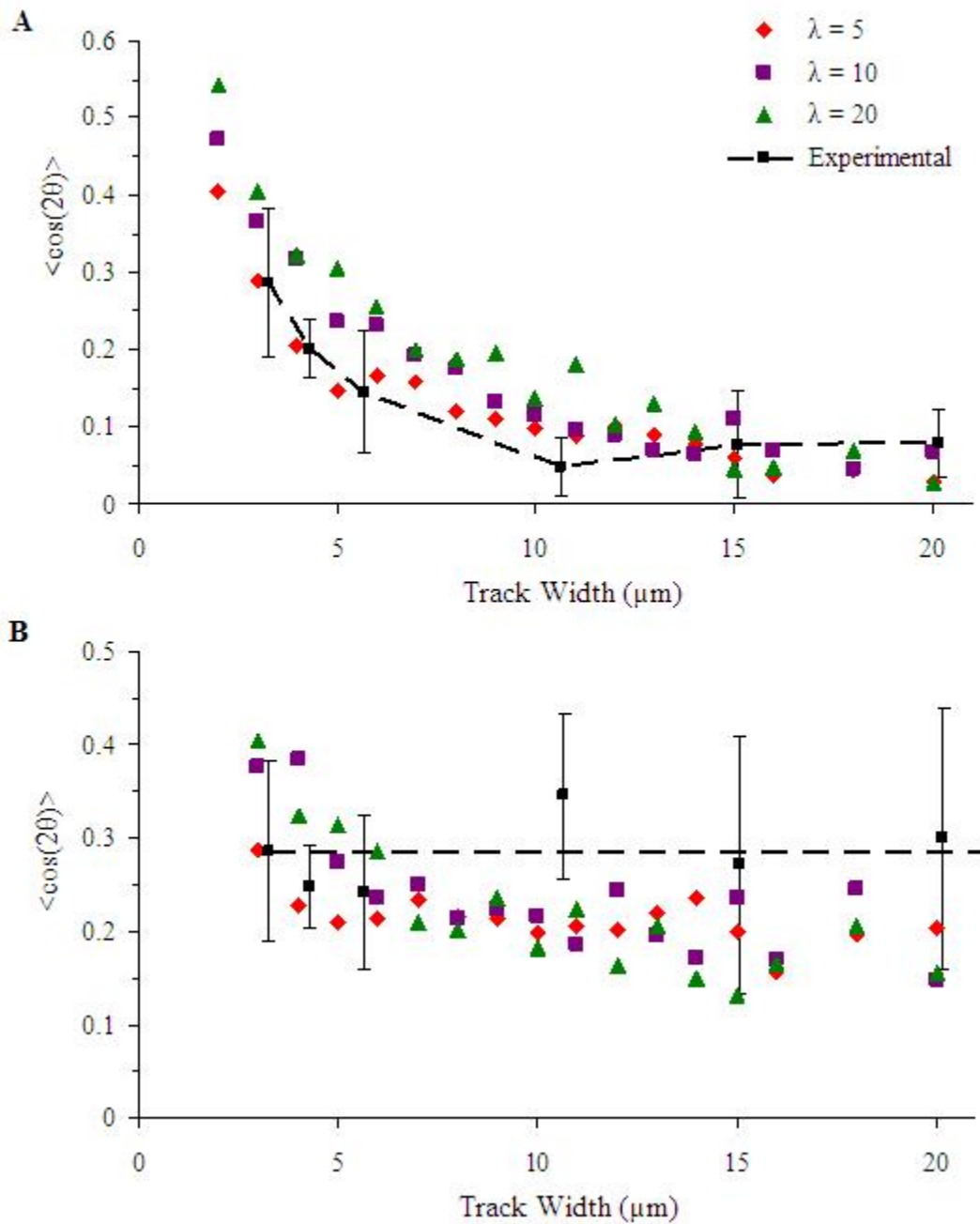


Figure 3-10. Effect of track width and persistence length on the alignment of filaments. A) The simulation produced the same trend found experimentally, with a slight dependence of the alignment on the persistence length. The higher persistence lengths produced lower alignment values at narrower track widths ($< 10 \mu\text{m}$). At a track width of $12 \mu\text{m}$, all three conditions produced the same alignment. B) Effect of the track edge on the alignment of filaments. Only filaments or parts of filaments within $1.5 \mu\text{m}$ of the edge of the track were included in the calculation of the alignment. Results are similar to Figures 3-7B and 3-8 B.

CHAPTER 4
ACTIN-BASED MOTILITY OF *LISTERIA* AND PARTICLES ON MODIFIED SURFACES

4.1 Introduction

We have replicated actin-based motility with both *Listeria* and ActA-coated 500-nm diameter polystyrene beads in bovine brain cell extract. NEM-myosin treated glass coverslips were used to provide an anchor for the actin rocket tails attached to the motile particles. Although actin rocket tails contained many filaments ($\sim 10^3$), providing a system much different than single filament elongation, these surfaces were able to confine tails and control the propulsion of the associated particles, as observed through both real-time phase-contrast imaging and TIRF.

We found that the paths of particles attached to confined actin-rocket tails lacked large thermal undulations (Brownian motion) relative to those particles and tails in solution. The effects of the NEM-myosin surfaces on the persistence and elongation rate of the actin rocket tail and the propulsion of the attached particle have been analyzed. Treatments of glass coverslips to create patterns or channels, including microcontact printing and photolithographic lift-off of cyclic transparent optical polymer (CYTOP), a fully fluorinated polymer that reduces nonspecific protein interactions (110), were used to attempt to guide the path of the particles near the surface.

4.2 Materials and Methods

4.2.1 *Listeria monocytogenes* Growth and Protein Purification

Listeria monocytogenes Strain Lut12 (pactA) over expressing ActA (87) and labeled with 4',6-diamidino-2-phenylindole (DAPI), was generously cultured and prepared by Will Zeile (University of Florida, Gainesville, FL). *Listeria* strains SLCC 5764 and DPL2823 were a kind gift of Dr. Daniel Portnoy (University of California, Berkley, CA).

A truncated version of the transmembrane protein ActA with a His₆ tag on the N-terminus was purified from *Listeria monocytogenes* (strain DPL2723) (111). Agar plates (containing brain heart infusion (BHI) media with agar and chloramphenicol) were streaked with bacteria, incubated for 24 hr at 37 °C, and stored at 4 °C. A colony of bacteria from the plates was added to 50 mL of BHI media diluted in ddH₂O with 10 µg/mL of chloramphenicol and incubated overnight at 37 °C while shaking at 225 rpm. The bacteria solution was then transferred to 1 L BHI with 10 µg/mL of chloramphenicol and incubated at 37 °C while shaking (180 rpm) for 6 to 8 hr (final OD₆₀₀ = 0.6 to 0.8).

The bacteria solution was cooled on ice for 20 min and clarified by centrifugation at 2700 × g for 20 min at 4 °C in a JA-10 rotor (Beckman Coulter, Inc., Fullerton, CA). Ammonium sulfate was slowly added and dissolved (1hr) in the bacteria solution for a final concentration of 50% (313.5 g/L) at 4 °C and was left in 4 °C for 3 hr while stirring to equilibrate. The precipitate was centrifuged at 4 °C for 30 min at 7000 × g in a JA-10 rotor and resuspended in less than 10 mL of HEPES-KCl buffer (HKB; 20 mM HEPES pH 7.4, 50 mM KCl,) supplemented with protease inhibitors (1 complete mini, EDTA-free tablet per 10 mL, 1 mM PMSF) per liter of supernatant. The protein was eluted from solution using a 5 mL bed volume of Talon Ni-NTA resin equilibrated in HKB supplemented with 250 mM Imidazole. The fractions were dialyzed against HKB overnight to remove Imidazole from the buffer (111).

Actin was purified and labeled with Oregon green 488 carboxylic acid, succinimidyl ester (Invitrogen, Molecular Probes, Carlsbad, CA), with the same procedure described in Chapter 2. NEM-myosin was also prepared as described in Chapter 2.

Frozen whole bovine brains were grinded into a fine powder in liquid nitrogen and mixed with an equal volume of sonication buffer (10 mM Tris-HCl, pH 7.5, 2 mM MgCl₂)

supplemented with 10 $\mu\text{g}/\text{mL}$ each of pepstatin A, leupeptin, chymostatin, and 1 mM PMSF. The mixture was dounce homogenized 30 \times on ice, sonicated on ice with a tip sonicator for 30 sec bursts at 25% power, and then centrifuged at 17,000 $\times g$ for 20 min at 4 $^{\circ}\text{C}$ in a Ti60 rotor (Beckman Coulter, Inc., Fullerton, CA). The supernatant was then centrifuged at 118,000 $\times g$ for 1 hr at 4 $^{\circ}\text{C}$ in a Ti60 rotor. The supernatant was recovered and supplemented with 1 mM DTT and 1 mM ATP. The extract was aliquoted, flash frozen with liquid nitrogen, and stored at -70 $^{\circ}\text{C}$ (112).

4.2.2 Bead Preparation

500-nm diameter polystyrene beads (Polysciences, Inc., Warrington, PA) were diluted in MOPS buffer (100 mM MOPS pH 7.0 with KOH) for a final of 0.5% solids solution. The beads were rinsed twice by centrifuging at 16,000 $\times g$ for 5 min at 4 $^{\circ}\text{C}$ (Eppendorf 5415C microcentrifuge), and resuspending in MOPS buffer. *Bis*[sulfosuccinimidyl] suberate (BS^3) (Pierce, Rockford, IL) was diluted to 20 mM and added dropwise to the beads, and the solution was incubated for 15 min at room temperature while shaking. The BS^3 solution was removed by pelleting the beads through centrifugation (5 min, 16,000 $\times g$) and ActA was added directly to the beads at ~ 200 to 250 $\mu\text{g}/\text{mL}$. The solution incubated at room temperature for 1 hr while shaking gently. The ActA solution was removed by centrifugation (5 min, 16,000 $\times g$), and the beads were resuspended and rinsed twice in a 200 mM solution of glycine methyl ester in MOPS buffer to block all remaining BS^3 binding sites. Beads were rinsed once in MOPS buffer, resuspended in brain extract buffer (20 mM HEPES, pH 7.5, 1 mM MgCl_2 , 1 mM EGTA, 100 mM KCl, 0.2 mM CaCl_2 , 150 mM sucrose), and stored at 4 $^{\circ}\text{C}$ until activity of the beads decreased significantly, which typically occurred within one week (William Zeile, unpublished).

4.2.3 Motility Assay

Motility assays consisting of extract from bovine brain cells were used to mimic *in vivo* conditions for actin-based motility of *Listeria* and 500-nm ActA-coated polystyrene bead. An aliquot of bovine brain extract was thawed and clarified by centrifugation at $16,000 \times g$ for 10 min at 4 °C. The supernatant was aspirated and supplemented for a final composition (by volume) of 10% creatine kinase (CK)-ATP regenerating solution (7.5 mM creatine phosphate, 2 mM ATP, 2 mM EGTA, 2 mM MgCl₂, 50 µg/mL creatine kinase), 10% protease inhibitors (10 µg/mL each of pepstatin-A, chymostatin, and leupeptin), 10% (10 mM) dithiothreitol (DTT) and 75% clarified extract (113).

After incubating on ice for 5 min, Oregon green 488-labeled actin was added to a final concentration of 5.7 µM and either *Listeria* (final concentration = 1 to 1000 dilution of stock) or ActA-modified beads (final concentration = 1 in 100 to 1 to 400 dilution of stock) were added in the final extract. Actin tails formed on these beads within 30 min and propelled the particles in solution. Motility assays used on modified surfaces were incubated in a microcentrifuge tube until approximately 15 to 30 min after the solution was first mixed. This typically allowed enough time for short rocket tails to form on the beads, which could then bind to the surface.

Flow-cells with cleaned glass coverslips were treated with either 2 µM NEM-myosin diluted in myosin dialysis buffer or 1% BSA in TM buffer (10 mM Tris, pH 7.5, 2 mM MgCl₂) for 1 min, followed by 1% BSA in TM buffer to wash any unbound NEM-myosin molecules and to passivate any exposed glass surface. A motility assay containing *Listeria* or ActA-modified beads was added immediately after the BSA rinse.

4.2.4 Fabrication of Channel Devices

Using a photolithographic lift-off technique, CYTOP was patterned on glass coverslips. A glass coverslip was photopatterned with two-coatings of NFR016, a negative photoresist. Using

an e-beam evaporator, a 50 Å-thick chrome layer was deposited on the top surface of the photoresist-patterned coverslip. CYTOP was then spin-coated onto the surface at 4000 rpm for 20 sec and was cured at 100 °C for 10 min. The slide was soaked in acetone for 5 min and sonicated briefly at low power. This caused the regions with the photoresist layer to lift off the surface, exposing the glass. The CYTOP layer was found to be approximately 2 μm thick based on measurements from an Alpha-Step IQ profilometer. PDMS stamps and CYTOP patterned surfaces were prepared by Dr. Suzanne Ciftan-Hens (International Technology Center, Raleigh, NC).

4.2.5 Microscopy and Analysis

Samples were observed using a Nikon Diaphot inverted photomicroscope equipped with phase-contrast optics for up to 2.5 hr after motility assays were mixed. Images were acquired using a digital CCD camera and analyzed using MetaMorph software. Time-lapse sequences were 5 to 10 min long with images acquired at 15 sec intervals. Objective-based TIRF (as described in Chapter 2) was used to image details on actin rocket tails bound to the surfaces approximately 2 to 4 hr after motility assays were mixed.

Random fields-of-view were taken for three experiments and combined to determine the fraction of bound actin rocket tails on BSA and NEM-myosin-treated surfaces. We only included those tails that were almost completely in the field-of-view for approximately the entire time-lapse sequence of 5 min. Particles and tails that were not attached to the surface were distinguished from those that were attached because of their larger fluctuations (which also hindered our measurements of tail length and bead velocity). A set of tails were considered to be partially attached; they were either attached at part of the tail that was not near the bead (causing a noisy bead trajectory) or the bead was attached to the surface but was not motile. Particle paths were manually tracked over time using MetaMorph software.

The elongation of the actin rocket tails was calculated by measuring the change in length of the actin rocket tail near the particle at a minimum of three time points for each tail. The average elongation rate was calculated by pooling all of the data within each surface treatment and determining the slope of a best-fit line (with intercept set to 0) for the change in length versus the change in time. Measurements of tails that were not bound to the surface may have been skewed due to parts of the tail leaving and re-entering the field-of-view. This limited our data of tails on passivated surfaces for the final analysis. Finally, tails were traced in the last frame of every time-lapse for both BSA and NEM-myosin treated surfaces to determine if the NEM myosin surface had any effect on the persistence of the tail. The distance between the end-points of the tails was squared and compared to the total length of the tail.

4.3 Results

4.3.1 Confining Particle Propulsion to the Surface

Actin-based motility was induced *in vitro* in cell extracts using the motility assay described above. Both *Listeria* and ActA-coated 500-nm diameter polystyrene beads produced actin rocket tails, as shown in images taken using phase-contrast microscopy (Figure 4-1). The actin tails looked identical in both cases, despite the slight difference in size and shape between the *Listeria* and the bead. The rocket tails elongated in solution, and in addition, rotated in three dimensions over time (Figure 4-2). The rocket tails took on a variety of different conformations, many tending to have a curved or helical shape.

In order to manipulate the path of the particles, we eliminated the rotation and thermal motion of the rocket tails in solution by confining them to NEM-myosin glass coverslips. Actin tails that were attached to the surface were distinguished from tails that were not attached by their decreased Brownian motion observed in real-time phase-contrast microscopy. Figure 4-3 shows an actin rocket tail attached to *Listeria* on an NEM-myosin surface over time. The rocket

tail remained stationary while the bacterium was propelled forward. On a BSA-coated surface, the actin rocket tail elongated but also changed position over time. Figure 4-4 shows similar results for a 500-nm diameter bead attached to a tail on an NEM-myosin and BSA surface. In 4-3B and 4-4B, the tail and the *Listeria* or bead remained in the focal plane for the entire time-lapse, moving only in the x- and y-directions. Many free tails also moved in the z-direction, coming into or out of the focal plane during the time-lapse. In addition, some free tails had part of their structure in the focal plane and the remainder above the focal plane for the entire sample time.

4.3.2 Effectiveness of NEM-Myosin Surfaces

Many samples contained a high percentage of actin rocket tails bound to the surface, as indicated by their lack of movement over time (Figure 4-5). The number of tails bound per field-of-view varied, depending on the sample, the time of the assay, and the position in the flow-cell. On NEM-myosin-coated surfaces, equal fractions of actin rocket tails attached to 500-nm diameter beads near the surface were completely bound or partially bound, comprising ~60% of the total number of tails (Figure 4-6). Partial binding occurred when a tail was attached at certain points away from the particle or when a particle attached to the surface was not moving. On the BSA surfaces, only one tail was attached to the surface, indicating that the binding of the actin rocket tails was caused by specific interactions with NEM-myosin.

The movement of the free tails in solution caused the trajectories of the attached beads to appear chaotic compared to the smooth trajectories of the particles attached to bound tails (Figure 4-7). Particle motility in the bound case was likely controlled by actin filament elongation within the actin rocket tail. For particles not bound (on either NEM-myosin or BSA-treated surfaces), the trajectory was chaotic because, in addition to elongation, the rocket tail itself was moving with respect to time. These results suggest that NEM-myosin can

effectively bind actin filaments within a large actin tail, confining the tail to the surface for some time while continuing to propel particles attached to the actin rocket tail in a more controlled manner. In some cases, the interaction between the NEM-myosin and the actin rocket tail was enough to confine actin rocket tails with helical shapes, as shown in Figure 4-8. It is unknown in this case if the actin rocket tail landed on the surface as a helix or elongated into that shape while bound to the surface. However, the particle did continue to follow the curvature of the helical path as its tail elongated, which is most likely an effect of the long persistence length of the rocket tail.

Even though the entire tail remains in the same position over time for many samples, it is likely that only some regions of the tail were attached. TIRF images show that regions of the rocket tails were clearly bound to the coverslips (Figure 4-9), while other regions were not interacting with the surface. Slightly above TIRF range (> 200 nm from the surface), the entire rocket tail was observed, proving that, in many cases, the actin rocket tail was bound randomly along its length. This implies that the entire length of the tail did not need to be interacting with the surface for the tail to remain bound. An enlarged TIRF image of the actin rocket tail revealed potential actin-surface interactions at the sides of the tail, where single filaments or small bundles seemed to protrude away from the main structure (Figure 4-10). It is unclear if these single filament protrusions were located at the bottom of the tail as well. The binding interactions may have occurred mainly with these filaments.

4.3.3 Particle Velocity and Tail Characterization

We next looked at the effect NEM-myosin substrata had on both elongation rate and persistence of actin rocket tails. Figure 4-11 shows a histogram of tail elongation rates on both NEM-myosin and BSA surfaces. NEM-myosin surfaces had a narrower distribution of instantaneous rates, whereas the BSA surfaces were more wide-spread, containing some rates

below 0 $\mu\text{m}/\text{sec}$. The change in length versus time was plotted for bound actin rocket tails on NEM-myosin surfaces and free tails on BSA surfaces (Figure 4-12). The slope was calculated from a best-fit line to determine an overall tail elongation rate of $0.0157 \pm 0.0005 \mu\text{m}/\text{second}$ for tails attached to NEM-myosin surfaces and $0.0135 \pm 0.001 \mu\text{m}/\text{second}$ for free tails near a BSA surface, showing little effect of the surface on the rate of particle propulsion. Accurate measurements were difficult to obtain for the free tails due to the motion of the tails over time in the x- and y-direction and also in and out of the focal plane. This difficulty in measurement could imply that the free filament elongation rate reported may be lower than the actual elongation rate due to loss of data. This may also account for the wider distribution of elongation rates and the negative elongation rates acquired for certain samples.

The persistence of the actin rocket tails was measured by comparing the total length of the tail to the distance between the start and the end of the tail. The ratio of distance to length of the tails bound to the NEM-myosin surface was similar to that of free tails up until lengths of approximately 35 μm , at which point bound or partially bound tails have a slightly higher ratio than free tails on NEM-myosin or BSA surfaces (Figure 4-13). This implies that the NEM-myosin had a slight effect on the final shape of the actin rocket tail and subsequently, a slight effect on the final path of the 500-nm particles. Furthermore, the average length of the actin rocket tails measured on the NEM-myosin surface ($28.4 \pm 1.5 \mu\text{m}$) was statistically greater than the average length for those on the BSA surfaces ($21.8 \pm 1.7 \mu\text{m}$), with a two-tailed p-value = 0.0196. This result indicates that tails bound to NEM-myosin-coated substrata contain more tail length within a two-dimensional plane than free tails. In this case, the NEM-myosin surface had a clear effect on the tail shape, eliminating the freedom of the tails to bend into the z-direction.

4.3.4 Guiding Particle Propulsion

Microcontact printing was used to attempt to further guide the particles, similar to the guidance of single filaments. There are many differences between actin rocket tails and single filaments, including size and solution conditions, indicating that this method may not be as effective for the large bundles of actin filaments. Initial attempts show selective binding of the particles to the NEM-myosin, but confinement does not compare to the tails bound to unpatterned NEM-myosin surface (Figure 4-14). Although tails remained near the surface, many rotated or moved around one point of attachment, implying that short tails shown in the time series were only partially bound to the surface. Furthermore, these tails did not elongate over time, preventing motility of the attached beads.

Factors that may be inhibiting the actin tail-NEM-myosin interaction on the microcontact-printed surfaces include the density of the NEM-myosin layer, conformation of NEM-myosin molecules and the binding activity of the NEM-myosin with actin filaments. In addition, the brain extract used contains large amounts of protein, including myosins, tropomyosins, and actin. All of these proteins may have bound to the regions of NEM-myosin non-specifically, blocking the binding of the actin rocket tails to the surface.

Three-dimensional surface structures using patterned CYTOP on glass coverslips have been tested for their ability to guide 500-nm diameter beads undergoing actin-based motility. While many actin tails were confined to the NEM-myosin-treated glass portion of the surfaces of these devices (Figure 4-15), the ability of the device to guide the particles has not yet been determined. Figure 4-16 shows a particle being propelled by an actin rocket tail encountering a wall at a perpendicular angle. The particle was propelled over the wall, indicating that the height and design of the wall were not optimal to guide the path of the particle.

4.4 Discussion

4.4.1 Mechanics of Actin Rocket Tails on Surfaces

The results obtained in this chapter suggest that surface manipulation may be used to confine the propulsion of both *Listeria* and 500-nm diameter particles undergoing actin-based motility. NEM-myosin adsorbed to glass surfaces has the ability to confine the actin rocket tails to the substratum while continuing to propel the objects. NEM-myosin molecules bind to single actin filaments, thus the tails must be confined to the surface by many interactions between single actin filaments within the tail and single NEM-myosin molecules.

Based on our TIRF images, NEM-myosin may create a place for actin filaments protruding and elongating from the sides of actin rocket tails to bind. In solution, filaments are likely protruding from all sides of the tail. Therefore, the side of the tail facing the surface may be interacting with the surface through these small filaments rather than filaments that are cross-linked within the main tail. These filaments may have been side branches created by the presence of Arp2/3 in the extract (114). If these filaments are present *in vivo*, they may function by incorporating in the cytoskeletal actin network, providing an anchor for the propulsion of *Listeria* in the cytoplasm. Our TIRF images also indicate that the entire length of the tail does not appear to be bound to the surface. Tails may be confined to the surface at random places along their length, and this may be sufficient for overall confinement of the tail. Another possibility is the areas that do not appear directly on the surface may be cross-linked to the nonspecific actin filaments that are attached to the surface, creating a network from the NEM-myosin surface to the tail.

Only filaments in the tails that are contacting the substratum are available for binding to the substratum, a fact which limits the effect the substratum properties has on the entire actin tail and the propulsion of the particle. The most significant effect of the surface-tail interaction is the

ability to reduce the noise in particle trajectories. By controlling the trajectories, particles are more likely to follow a designated path on a surface and move against flow or diffusion gradients. The tail elongation rate and two-dimensional shape was not affected significantly by the NEM-myosin surfaces. (The surface did affect the shape of the tail with respect to the z-direction.) The rocket tails contain many filaments, all of which contribute to the overall elongation rate and shape of the tail. Since only filaments near the surface are interacting with NEM-myosin, it is expected the surface interactions will have little effect on these parameters. Furthermore, the filaments protruding from the sides of the rocket tail, which are likely to be interacting with the substratum, should not effect the elongation rate at all since they are not elongating near the surface of the motile object.

4.4.2 Biochemical Considerations

Biochemical modifications may control certain parameters of the system, including percentage of beads that form tails, length of tails and velocity of the particles. We have tested a variety of extracts, including rat brain, bovine brain, and human platelet extracts. All three of these extracts supported motility of *Listeria* and beads. A thorough analysis of the extracts may be beneficial for optimization of the assay. The extracts may contain variable amounts of VASP, Arp2/3, ATP and ADP, protease inhibitors, ADF, cofilin, profilin and actin, as well as many unknown proteins that could aid or inhibit certain aspects of actin-based motility (115). Cameron, et al. showed that extract dilution, in addition to bead diameter and ActA coverage, influenced the speed of particles and the tail curvature (116). We expect these parameters will have the same effect on beads attached to the surfaces.

Another important factor is the time-sensitivity of the 500-nm ActA-treated particles, i.e. the same particles may behave differently as soon as one day after initially making and testing the sample. The particles tend to aggregate and the surface concentration of ActA decreases over

time through desorption. Even though ActA was cross-linked to the surface of the particles, it is possible that some ActA only physic-adsorbed to the beads and is aiding in tail formation and elongation. The subsequent desorption of this ActA may be enough to decrease tail formation significantly.

Surface binding is also dependent on the length of the tails when the motility assay is added to the modified glass coverslips. Before actin tails begin to form, an actin cloud, or a cross-linked actin network, surrounds the ActA-coated motile object. The bead inside this network may make small fluctuations, eventually causing the network to break spontaneously to one side of the bead, i.e. symmetry break (117). If the assay is added to the surface during the actin cloud state, the cross-linked actin network may bind to the surface, trapping the bead inside the network, ultimately preventing symmetry breaking. All of these factors combined make the biochemistry of this system complex. It may be beneficial in the future to move from cell extracts to single component systems (115), which could enhance the effect of the surfaces on the actin rocket tails and particle propulsion as well as allow more control over the velocity and curvature of the particles.

4.4.3 Considerations for Bionanotechnology

As mentioned before, each NEM-myosin molecule binds to only one filament in the tail, leaving most of the tail unaffected by this interaction. This characteristic of actin tails could indicate that modified substrata alone may have a limited effect on controlling the trajectories of the 500 nm beads on the surface. With larger actin structures propelling particles, a combination of channels and modified substrata may provide the most control over the trajectory of the particles (105). Microcontact printing may be further investigated as a way to confine filaments to the surface, but it is unlikely that this technique will provide the same advantages that it does for single actin filaments. The actin rocket tail is much stiffer than a single actin filament,

suggesting that the smaller thermal fluctuations of the tail would make it difficult to bend back and rebind to a track. In addition, the path and velocity of the propelled particle is dependent on many filaments that may not be interacting with the surface. For these reasons, physical barriers may be needed to provide control over the particle's path.

Further optimization of the height of the channels may prevent the particles from traveling over the top of the channel walls. Other designs, such as undercuts may also prevent this, as shown to be effective by Hess, et al. for the guidance of sliding microtubules (17). If the channel walls are high enough, beads may be able to take paths that include sharp or rounded turns. In addition, directionality of the particles may be easily obtained through the use of paramagnetic particles or electric fields. By allowing tails to bind first and then applying a force, the particles may change their path toward a specified direction.

Particle motility for potential use in nanodevices has been confined to methods using single filament microtubule/kinesin or actin/myosin sliding assays, where particles are either attached to the filament or the motor protein (2, 3, 6, 7). Bohm, et al. successfully showed motility of large, micron-sized particles of various materials by attaching the objects to kinesin and allowing them to move along an array of aligned, isopolar microtubules (3). We have added another method of particle motility that exploits actin polymerization and the ActA/VASP complex and can be useful in the future for nanodevices.

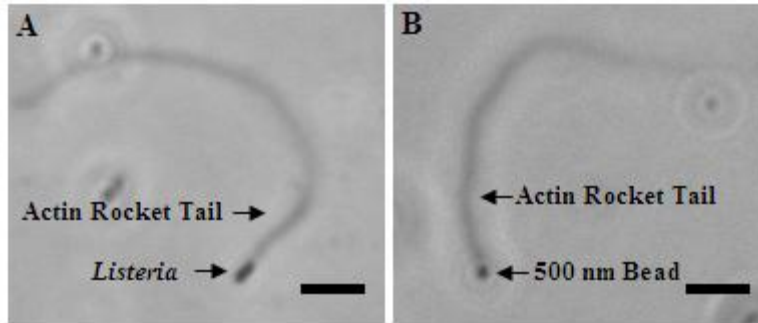


Figure 4-1. *Listeria* and 500-nm diameter bead propelled by actin rocket tails. A) *Listeria* placed in cell extract formed actin rocket tails at its rear. B) Polystyrene 500-nm diameter particle treated with the surface protein ActA emulated the behavior of *Listeria* under the same conditions, forming actin rocket tails. Images were taken in phase-contrast (scale bars = 5 μm).



Figure 4-2. Rotation of a helical actin rocket tail in solution. A polystyrene 500-nm diameter particle contained an actin rocket tail which rotated in three dimensions over time. The arrow indicates where the tail crosses itself in the various views. The images were taken 1 minute apart in phase-contrast (scale bar = 5 μm).

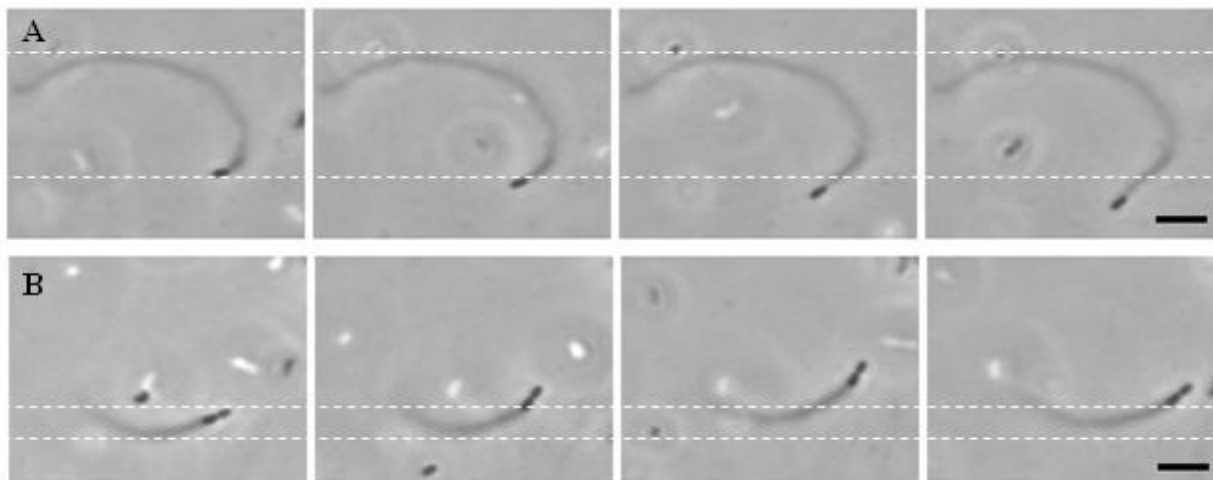


Figure 4-3. *Listeria* rocket tails on NEM-myosin and BSA-treated surfaces. A) *Listeria* actin rocket tail is bound to an NEM-myosin treated surface. The tail did not move over time, as indicated by the top line. The actin rocket tail propelled the *Listeria* as seen by the increasing distance between the bacterium and the bottom line over time. Images shown were taken 75 seconds apart. B) *Listeria* actin rocket tail remained free in solution when exposed to a surface passivated with BSA, as indicated by the movement of the entire tail over the time lapse. Note there are two *Listeria* in this time-lapse sharing a membrane. Images shown were taken every 45 seconds (scale bars = 5 μm).

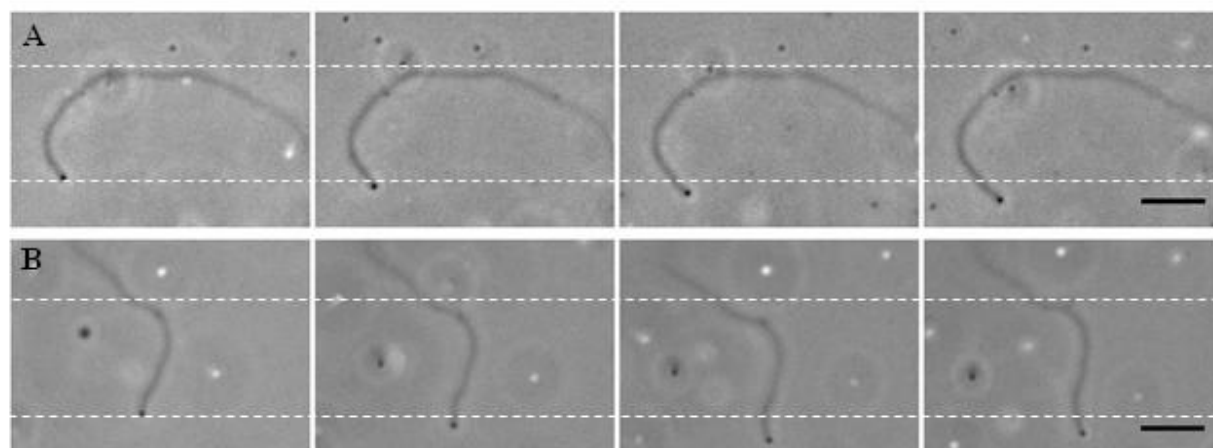


Figure 4-4. 500-nm diameter beads attached to rocket tails bound on NEM-myosin and BSA-treated surfaces. A) Actin rocket tail is bound to an NEM-myosin treated surface. The tail did not move over time, as indicated by the top line. The actin rocket tail propelled the particle as seen by the increased distance between the particle and the bottom line. Images shown were taken 75 seconds apart. B) Actin rocket tail remained free near a surface passivated with BSA, as indicated by the movement of the entire tail over the time lapse. Images shown were taken every 75 seconds (scale bars = 10 μm).

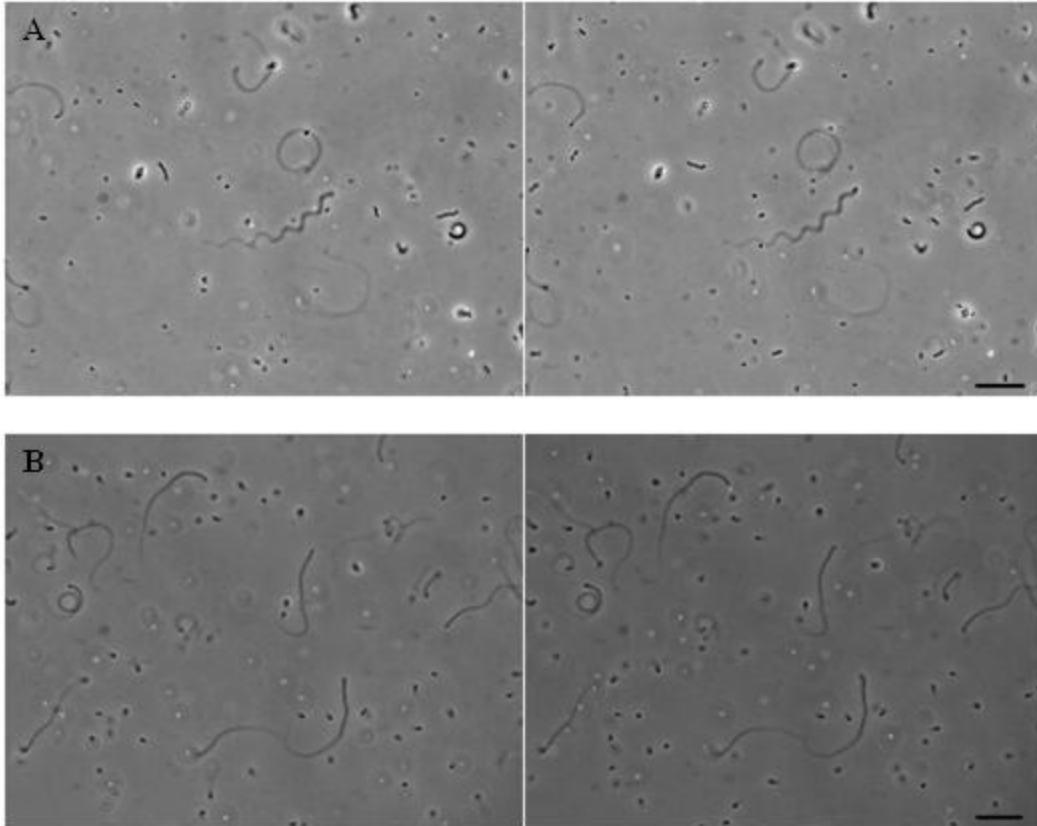


Figure 4-5. Fields-of-view with large percentage of tails bound to surface. A) Actin rocket tails on *Listeria* bound to an NEM-myosin surface. Many tails remained in position while elongating over the 2.5 minutes between images. B) Actin rocket tails on 500-nm diameter beads are also bound in a high percentage to NEM-myosin treated surface. Tails remained in position between the first image and the second image, taken 3.5 minutes apart (scale bars = 20 μm).

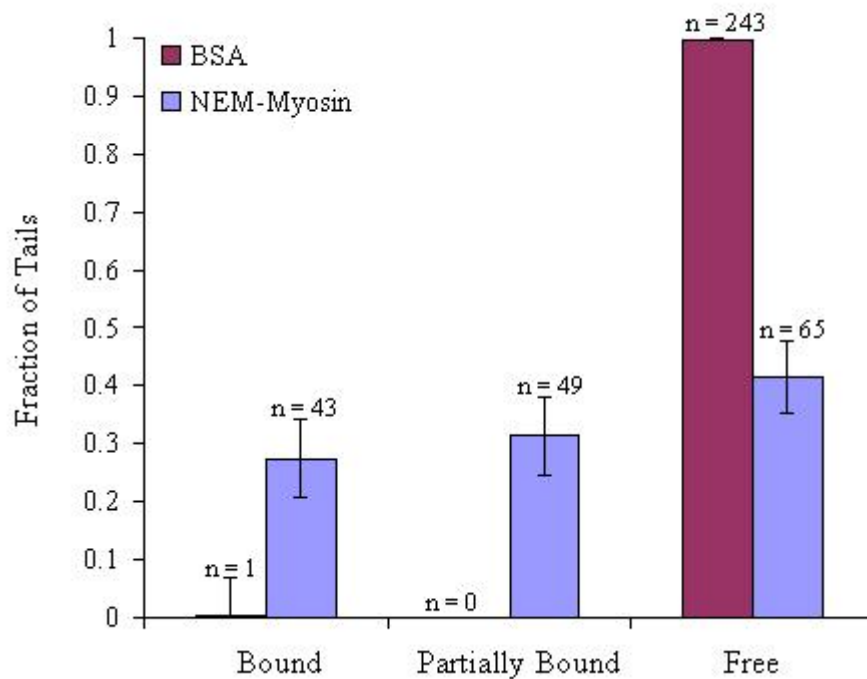


Figure 4-6. Fraction of actin rocket tails bound to NEM-myosin and BSA-treated surfaces. Only one tail was bound to the BSA surface. Of the tails on the NEM-myosin surface, 28% were bound and successfully propelling a particle, 31% were partially bound, and 41% were free in solution. Tails were analyzed from 20 randomly selected fields-of-view for each surface from three different experiments. Error bars represent \pm standard error = $(f(1-f)/N)^{1/2}$, for N total filaments.

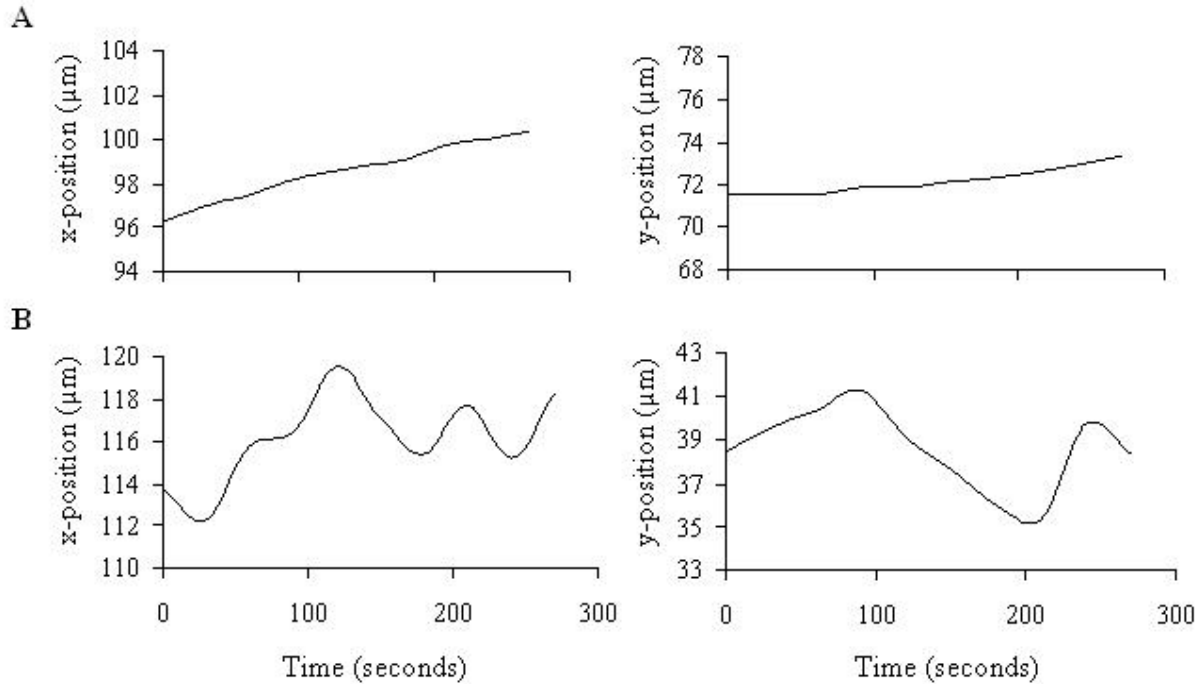


Figure 4-7. Change in x- and y-position over time for beads on NEM-myosin and BSA surfaces. A) A 500-nm diameter bead attached to an actin rocket tail bound to an NEM-myosin coated surface is propelled forward in a smooth trajectory. B) A 500-nm diameter bead attached to an actin rocket tail that is in solution near a BSA-coated surface underwent Brownian motion as indicated by the noise in the position over time.

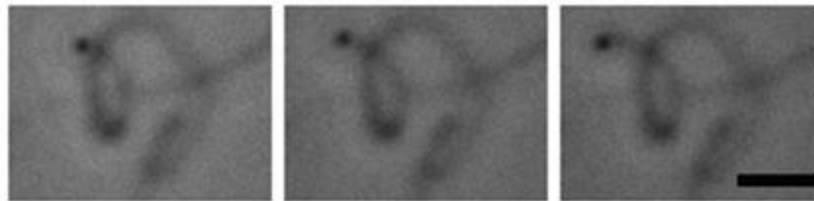


Figure 4-8. Helical actin rocket tail confined to NEM-myosin-treated surface. Images were taken 1 minute 15 seconds apart (scale bar = 5 μm).

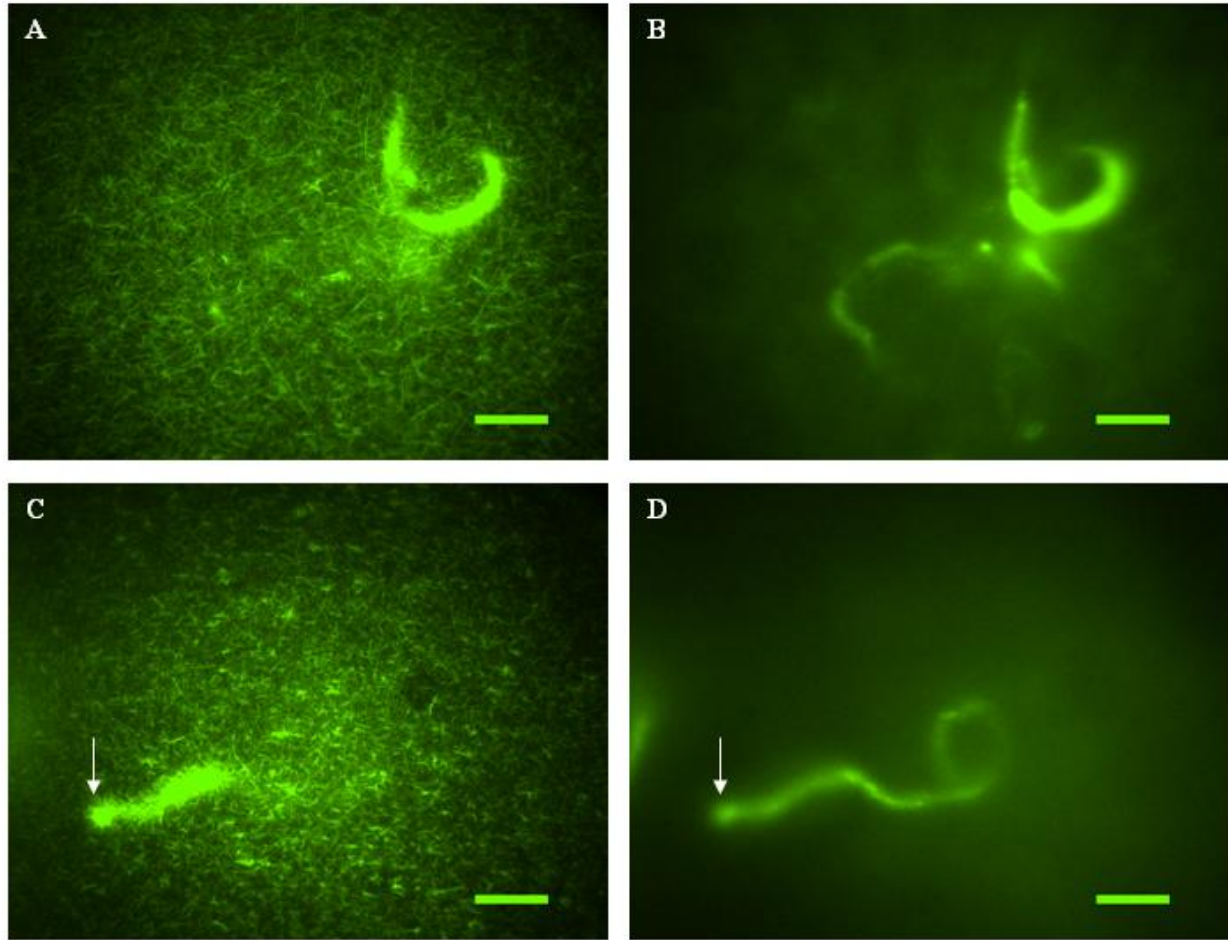


Figure 4-9. Actin rocket tails in total internal reflection fluorescence microscopy. A) Actin rocket tail attached to *Listeria* was bound to the NEM-myosin surface, as shown in TIRF. The actin rocket tail appears to have smaller bundles or single filaments extending off the side of the main structure. B) Image of A taken in fluorescence just above the 200-nm TIRF region, showing the entire rocket tail. Only a small portion of the length of the tail was bound to the surface. C) Actin rocket tail attached to a 500-nm diameter bead was bound to a NEM-myosin surface. The arrow points to where the bead was most likely located. D) Fluorescent image slightly above TIRF corresponding to C (scale bars = 10 μm).

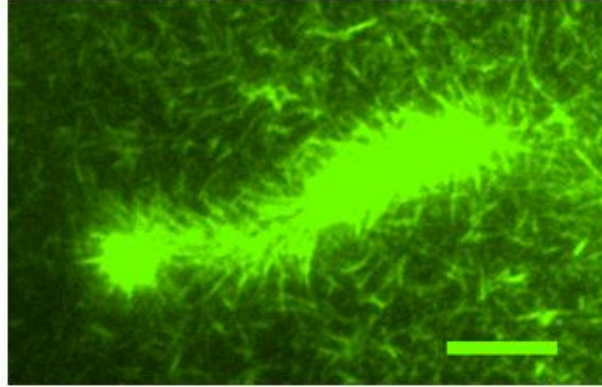


Figure 4-10. Magnified image of actin rocket tail with protruding filaments. The actin tail had single filaments or small bundles of actin extending from the main structure. Short filaments that may have formed spontaneously in solution were also bound to the surface (scale bar = 5 μm).

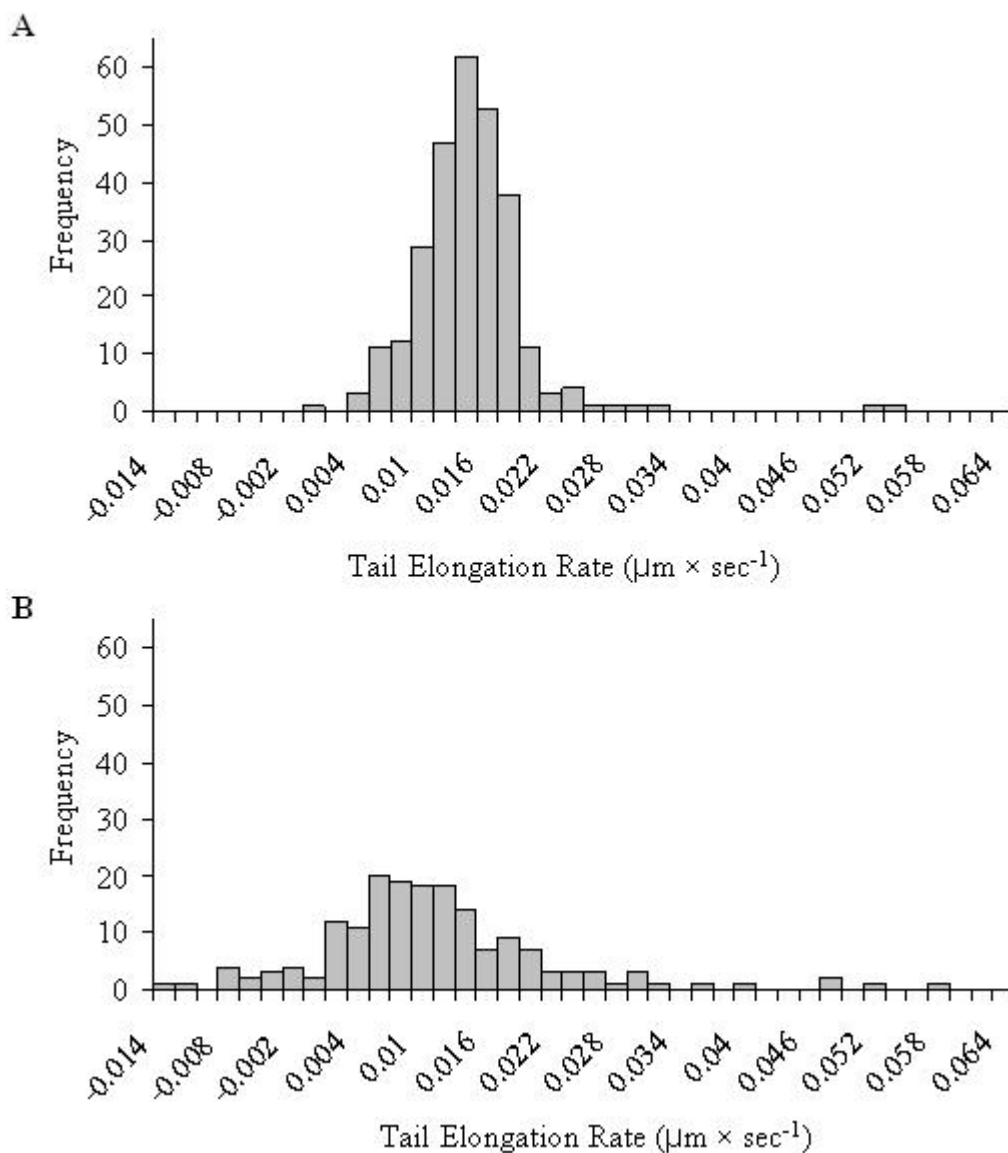


Figure 4-11. Actin tail elongation on NEM-myosin and BSA surfaces. A) Histogram of instantaneous tail elongation rates (frequency) observed for actin tails bound to NEM-myosin surfaces. The peak occurs between 0.015 and 0.016 $\mu\text{m}/\text{sec}$ ($n = 280$, 80 filaments). B) Histogram of instantaneous tail elongation rates observed for free actin tails near a passivated BSA-treated glass surface. The peak occurs between 0.006 and 0.008 $\mu\text{m}/\text{sec}$. The wider spread of rates, including negative elongation rates, was caused by difficulties in measuring the length of tails that were not attached to the surface and were potentially moving in and out of the focal plane ($n = 169$, 58 filaments).

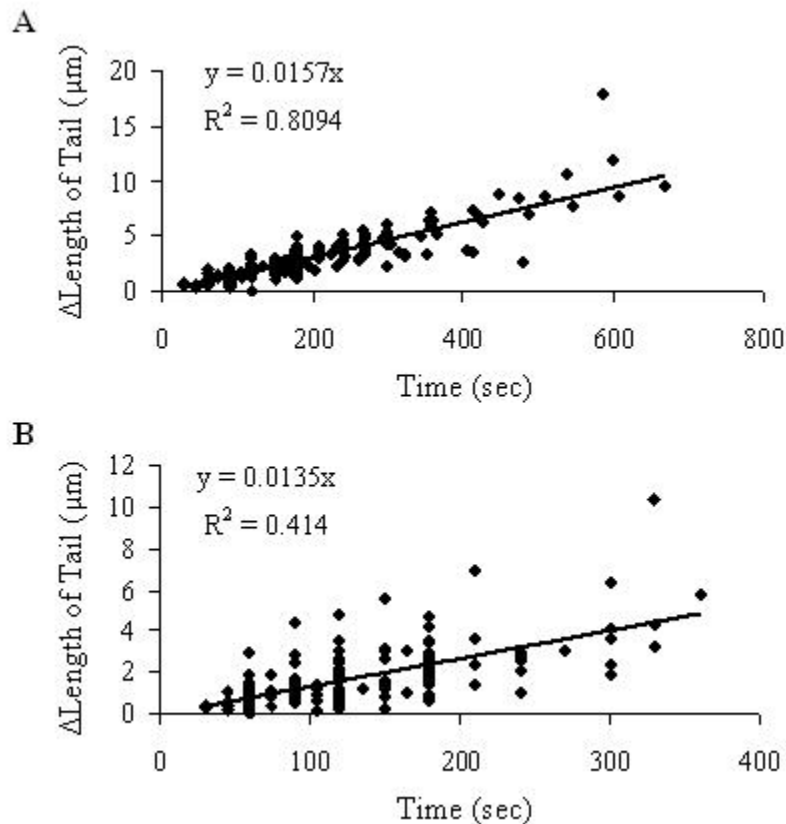


Figure 4-12. Average tail elongation rates determined from the slope of a best-fit line. A) The changes in length of the tails attached to NEM-myosin surfaces were plotted against time to determine an average rate of $0.0157 \pm 0.0005 \mu\text{m}/\text{sec}$. The two outliers in the histogram (Figure 4-11A, $> 0.05 \mu\text{m}/\text{sec}$) were excluded from the plot ($n = 280$, 80 filaments). B) Values less than 0 and greater than 0.05 were eliminated (Figure 4-11B) to determine an average elongation rate of $0.0135 \pm 0.001 \mu\text{m}/\text{sec}$ for free filaments near BSA-treated surfaces ($n = 146$, 50 filaments). An unpaired t-test gives a p-value of 0.04, indicating that the two elongation rates are significantly different.

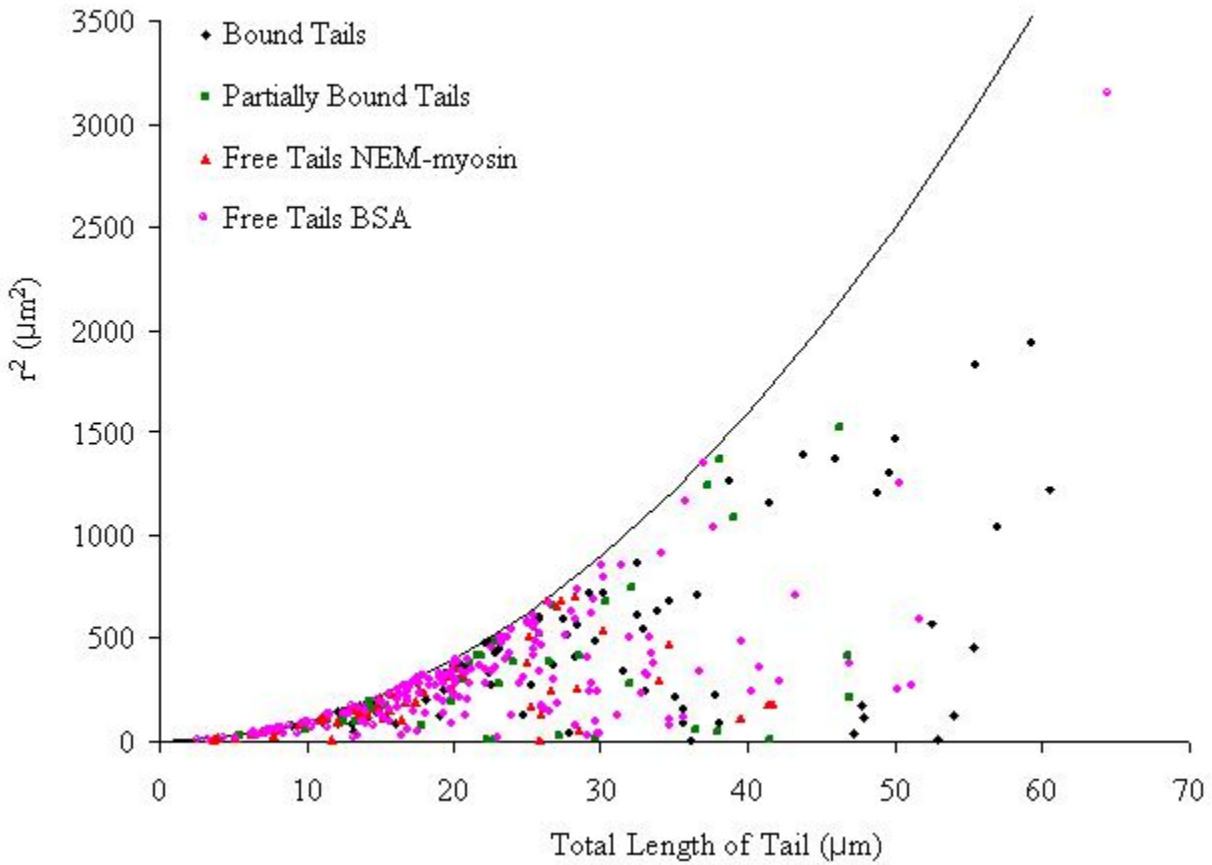


Figure 4-13. NEM-myosin surface effect on persistence of tail. Tail lengths were measured as they appeared in the two-dimensional focal plane. The total length of the filaments was typically longer than the distance between the end-points of the tail (r). Bound and partially bound tails ($n = 84$ and $n = 40$, respectively) between 35 and 60 μm long seem to have slightly more persistence than free tails on NEM-myosin surfaces or BSA surfaces ($n = 56$ and $n = 197$, respectively). We were able to measure more length per filament for the bound tails due to their confinement in the focal plane.

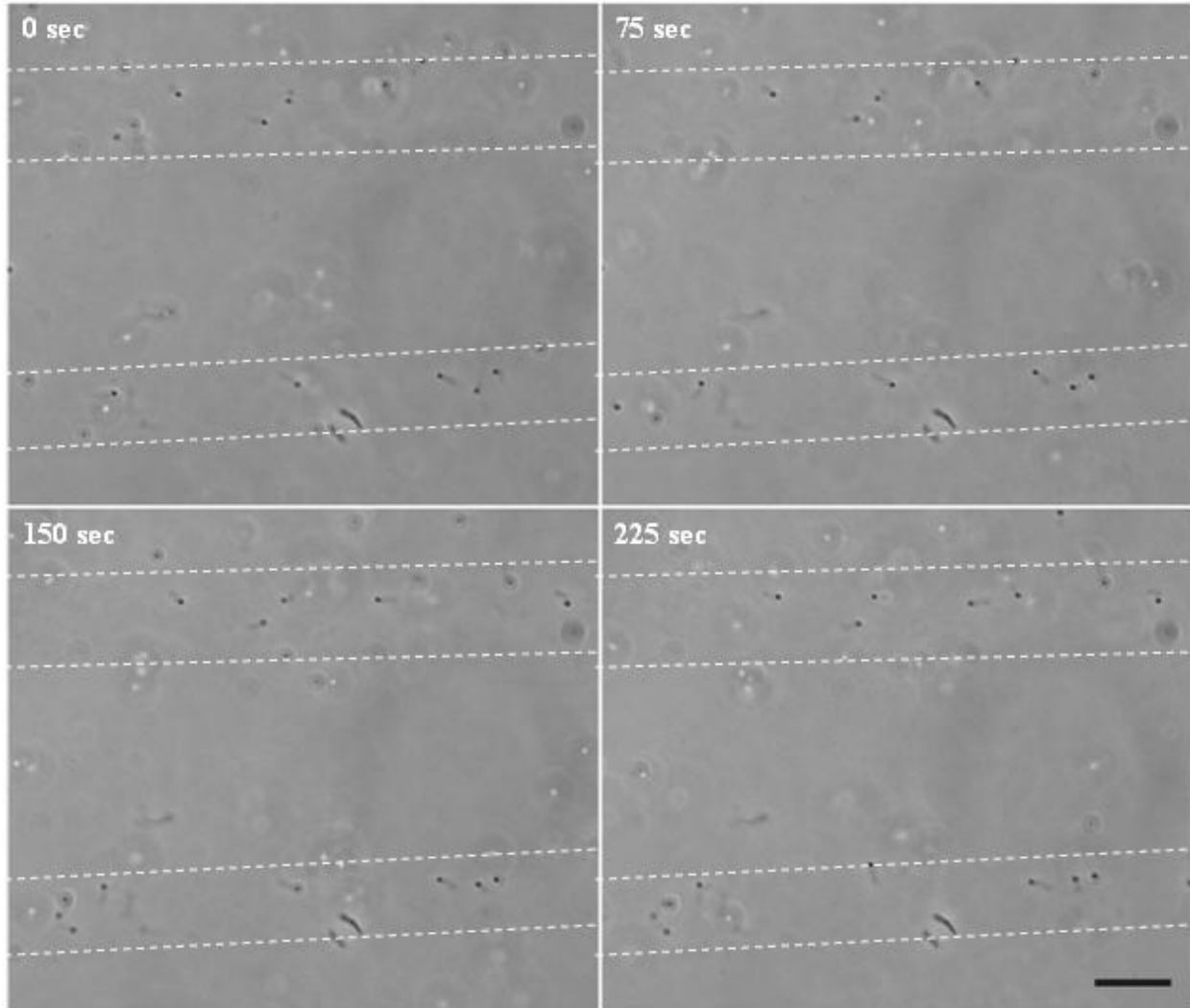


Figure 4-14. Stamped surfaces with 500-nm diameter beads attached to actin tails. Very faint lines in phase-contrast were present and are enhanced by the white dashed lines. Beads seemed to attach to the regions within the track boundaries; however, elongation was not observed, and tails seemed to rotate or move slightly over time. Images shown were taken 75 seconds apart (scale bar = 10 μm).

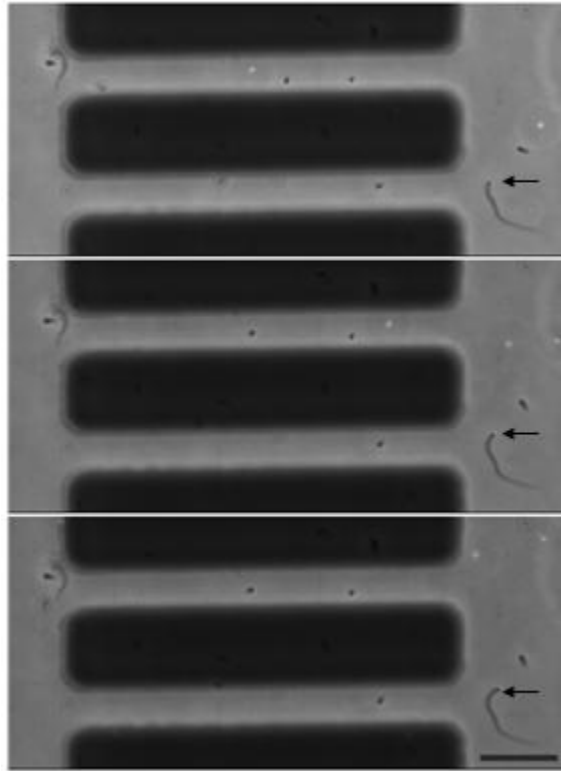


Figure 4-15. Actin tails bound to NEM-myosin-treated exposed glass of fabricated device. Black regions in the images are CYTOP, while all other area is exposed glass. The arrow points to a 500-nm diameter bead that was propelled by an actin rocket tail bound to the glass. No tails were observed elongating inside the channels. Images were taken 75 seconds apart (scale bar = 20 μm).

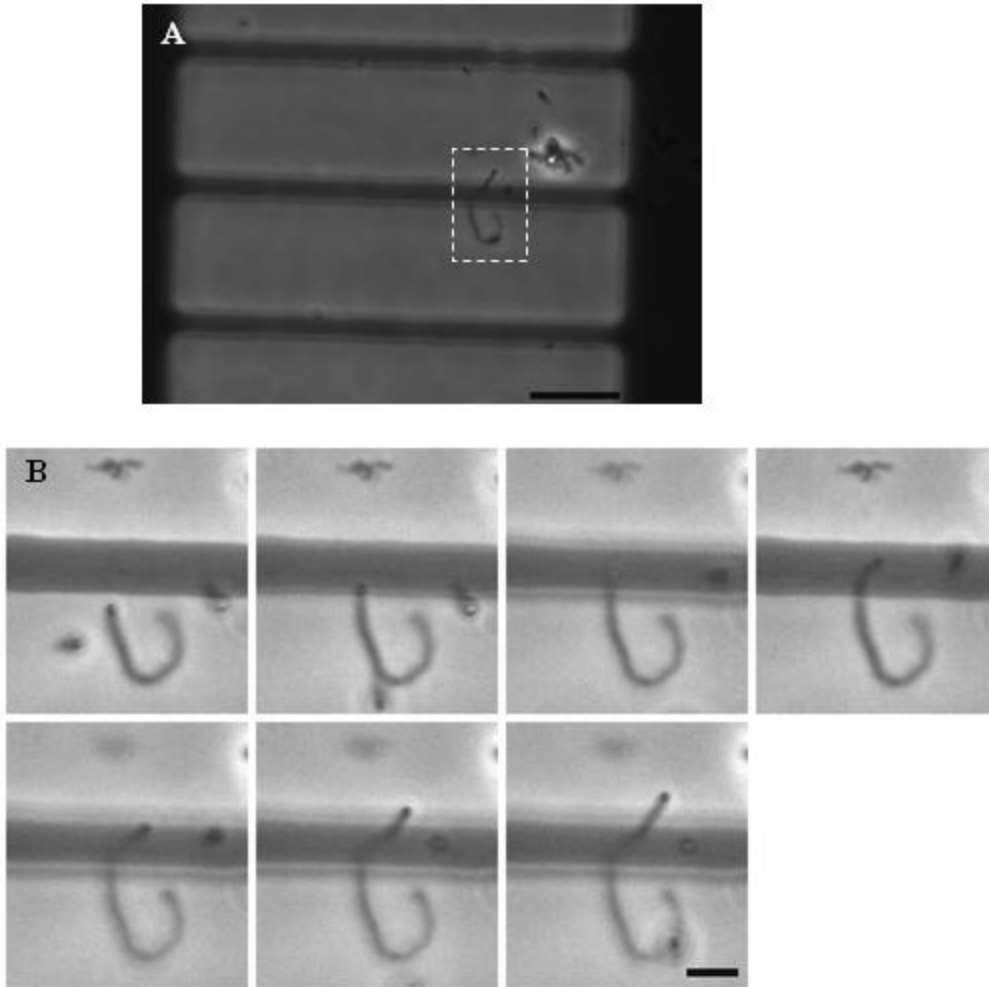


Figure 4-16. Actin rocket tail encounters CYTOP wall. A) Image of entire region of the device. The black region is CYTOP while all other regions are NEM-myosin treated glass (scale bar = 20 μm). B) An actin rocket tail confined to the glass surface encountered the wall at a perpendicular angle and propelled the particle over the channel wall, indicating that channel walls may need to be higher to guide the particles. Images shown are at 2.5 minute intervals (scale bar = 5 μm).

CHAPTER 5 SINGLE FILAMENT ACTIN-BASED MOTILITY OF PARTICLES

5.1 Introduction

The use of rocket tails for propulsion of larger particles and bacteria is challenging in that guiding stiff bundles of actin filaments on modified surfaces is difficult without three-dimensional barriers (channel walls). Smaller particles (50 nm in diameter) have potential to be propelled by a single filament or a few actin filaments while behaving similarly to elongating single filaments without particles. As stated earlier, this may lead to guidance of these particles using microcontact-printed tracks (Chapter 2). The challenge thus far has been observing elongating single filaments bound to particles while persistently attached via the ActA/VASP complex.

The only previously published observation of a single filament on a 50-nm diameter ActA-coated bead was obtained using transmission electron microscopy (TEM) (89). Recently, our group has observed many single filaments on 50-nm ActA-coated beads in TEM (Sturm, C., J. Phillips, W. Zeile, K. Interliggi, R. Dickinson, and D. Purich, unpublished), lending promise to the possibility of single-filament bead propulsion for nanodevices. Processively elongating single filaments have been more frequently and easily observed using formins attached to 1- μm diameter beads (27). A bead with a diameter of 1 μm would be too large to guide on microcontact-printed surfaces alone, but the attachment of single filaments through formins could be applied to smaller particles.

With our recent experiments, we have shown that single filaments are attached at their (+)-ends to small ActA-coated beads, supporting the end-tracking motor mechanism for ActA-induced filament elongation (Sturm, C., J. Phillips, W. Zeile, K. Interliggi, R. Dickinson, and D. Purich, unpublished). This result also verifies the potential for guiding small particles

with single filament elongation through filament end-tracking motors. To address the possibility of single-filament actin-based motility in nanodevices, we first looked at attaching particles, rather than tails, to surfaces. This method decreases the Brownian motion of the beads to give a reference point for actin filament-particle interaction and allows dynamic observation in TIRF. Once filaments could be observed consistently, the system was optimized to visualize only a single filament or a few filaments per bead. Actin filaments were characterized by their fluorescent intensities to elucidate the mechanism of attached filament elongation near the bead surface. Finally, attempts were made to attach actin filaments under these conditions to NEM-myosin surfaces to observe a motile bead. The complexity of this system was assessed through these experiments.

5.2 Materials and Methods

5.2.1 Protein Preparations

ActA, bovine brain extract, actin, and NEM-myosin were all prepared as described in Chapter 2 and Chapter 4.

5.2.2 Bead Functionalization

A 500- μ L aliquot of 50-nm diameter silica beads (Polysciences, Inc., Warrington, PA) was pulse sonicated 20 \times at low power (Benson Sonifier 450) to break apart aggregates of beads and suspend them evenly in solution. The beads were incubated for 1 hr at room temperature with 0.2% gluteraldehyde with gentle shaking. The solution was centrifuged at 16,000 \times g for 5 min at room temperature followed by aspiration of the supernatant and resuspension of the beads in 500 μ L of 1600 μ g/mL of ActA in brain extract buffer. The solution incubated for 40 min at room temperature with gentle shaking, followed by centrifugation (16,000 \times g , 5 min, 4 $^{\circ}$ C). The beads were resuspended in a 500 μ L solution of 3100 μ g/mL of Oregon green 488-labeled BSA and incubated for 1 hr at room temperature. The solution was centrifuged as before,

resuspended in 500 μ L of 100 mM glycine methyl ester in brain extract buffer to block any reactive gluteraldehyde molecules, and pulse sonicated. The solution was centrifuged and resuspended in brain extract buffer twice to wash away any excess protein or chemicals and then stored in brain extract buffer at 4 °C.

5.2.3 Motility Assays

Two motility assays were tested using the 50-nm diameter beads. First, beads were attached to the surface and exposed to a motility assay. The second assay bound actin filaments formed in a solution of ActA-coated 50-nm diameter beads and extract to NEM-myosin surfaces, similar to the motility assays described in Chapter 4.

5.2.3.1 Attached beads

Aminopropyltriethoxysilane (APES)-treated surfaces were prepared as follows. Glass coverslips were rinsed in water followed by 100% ethanol. Dry coverslips were then incubated in a water-free acetone bath for at least 1 hr before transferring to a 2% APES solution in water-free acetone. Coverslips were incubated in the APES solution for two days, rinsed twice in acetone and once in water, and set out to dry. These coverslips were incubated in a 1% gluteraldehyde solution for 20 min at room temperature and rinsed twice in distilled water. The coverslips were dried and then made into flow channels using double-sided tape.

The 50-nm diameter ActA-treated silica beads were diluted in brain extract buffer, added to the flow channel and incubated for 10 min at room temperature. A 100 mM solution of glycine methyl ester in brain extract buffer was flowed into to the channel at twice the chamber volume and incubated for 20 min, followed by brain extract buffer for storage until use. After incubating on ice for 5 min, supplemented bovine brain extract (see Chapter 4) with either 100% or 60% extract diluted in brain extract buffer was mixed with 5 μ M of Oregon green 488-labeled actin and the solution was flowed into the channel. Actin filament structures were visible within

a few minutes. When noted, reactions were fixed with 1% glutaraldehyde after the reaction was allowed to proceed for 1 to 5 min.

5.2.3.2 NEM-myosin surfaces

Flow-cells with cleaned glass surfaces were treated with 2 μ M NEM-myosin for 1 min followed by 1% BSA in HS-TBS and 1% BSA in LS-TBS. A motility assay containing a 1 to 200 dilution of ActA-coated silica beads was added to the surfaces. (See Section 4.2.4 for a description of the motility assay.)

5.2.4 Microscopy and Analysis

All samples were observed using TIRF microscopy. MetaMorph was used to acquire images and to perform analysis. Fluorescent intensity line-scans were performed on samples to determine the change in intensity over time at various positions on actin filaments. Rate constants for the recovery of fluorescence at these positions were calculated by fitting the data to Equation 5-1.

$$\frac{I - I_{Eq}}{I_o - I_{Eq}} = e^{-kt} \quad (5-1)$$

I is the intensity (arbitrary units) at time, t (sec), I_o is the initial intensity immediately after photobleaching, I_{Eq} is the equilibrium intensity reached, and k is the rate constant (sec^{-1}).

Microsoft Excel was used to solve for k and I_{Eq} by solving for the minimum difference between the experimental and theoretical values.

5.3 Results

5.3.1 Actin Asters

We observed growth of actin filaments from 50-nm ActA-coated beads covalently bound to glass coverslips using TIRF. These actin filaments formed actin asters, or star-like structures, around the beads over time (Figure 5-1). The highest intensity of fluorescence was at the center

of the beads, and the filaments' intensities seemed to decrease with increasing distance from the bead (Figure 5-2). One explanation of this decrease implies that new monomers were incorporating at the particle ((+)-end elongation near the bead) and that the older regions of the filament (the (-)-ends), which have been exposed to light in TIRF and were therefore dimmer due to photobleaching, were further away from the bead. Another possibility for the decrease in intensity is that shorter filaments closer to the surface were directly below longer filaments, which were slightly above the surface. In either case, many of the filaments present demonstrated the same trend (Figure 5-2).

To investigate monomer addition further, we photobleached fields-of-view by exposing the samples to the laser at its highest intensity and observing the recovery of the fluorescence. Figure 5-3 is an example of photobleaching where filaments reappeared on the particle and on the glass surface in the field-of-view. A closer look indicates that the reappearing filaments on the surface of the bead seem to correspond to a filament existing on the bead before photobleaching (Figure 5-4). Not all filaments present before photobleaching reappeared.

The fluorescent intensity of two filaments was plotted against the filament distance from the center of the bead for four different time points after photobleaching occurred (Figure 5-5). In the first case, the filament recovered, following the same trend of intensity along the length of the filament until approximately 1.5 μm away from the particle, where the intensity increased to above the original intensity. This may be due to a short, free filament landing above the filament. In the second case, the intensity recovery followed the same trend of intensity along the length as the original filament, reaching approximately 50% to 75% of the initial intensity. In both cases, after three minutes of recovery, the fluorescent intensity decreased slightly.

Photobleaching is most likely occurring again after this time period, despite the short exposure time, causing the fluorescent intensity to decrease.

The fluorescent intensity was also measured as a function of time. We fitted the fluorescent intensity as a function of time and found both the equilibrium intensity and the rate constant at various points along the filament length. In Figures 5-6A and B, corresponding to the filament represented in Figure 5-5A, neither the rate constant nor the equilibrium intensity followed a clear pattern with respect to the length of the filament. The first two rate constants may be lower because the points were located near the center of the bead, which did not photobleach completely.

In Figures 5-6C and D, which correspond to the filament in Figure 5-5B, the rate constant decreased exponentially over the length of the filament, reaching a final value assumed to correspond to the background rate of recovery. This implies that recovery near the bead is faster, i.e., monomers are incorporating in the filament at the bead's surface first. Based on the initial fluorescent intensity, the region near the bead seems to have a high concentration of monomers, which could be locally available to the (+)-ends of polymerizing filaments. The equilibrium intensity remained near the same ratio (compared to the initial intensity before photobleaching) along the length of the filament, except for a decrease between 0.5 and 1 μm .

5.3.2 Single Actin Filaments

From these results, it is difficult to determine clearly if filaments are incorporating at the surface of the particle through filament end-tracking motors. Therefore, the brain extract buffer was diluted to reduce the number of filaments per bead and samples were fixed with glutaraldehyde to observe a single filament attached to a bead (Figure 5-7). These samples showed single filaments that were present on particles bound to the surface. The filaments were

all swept in the direction of flow during the fixing step, potentially causing two filaments (on the same bead) to appear as one.

We next attempted to bind filaments with attached beads to the surface to observe particle motility. NEM-myosin surfaces bound many filaments, but beads were hard to image from solution because they were small with large thermal motion (Figure 5-8). An enlarged image of the modified surfaces shows filaments with a corresponding bead, but it is unclear if they were attached or simply near each other by chance. The images from this experiment are difficult to interpret because many filaments may be free filaments in solution that bound to the surface but are not associated with a bead. Motility assays with and without beads appeared very similar in TIRF when looking at the fluorescently-labeled F-actin, confirming that F-actin was present in large concentrations in the extract (Figure 5-9). The actin monomer concentration in the solution is high ($> 5 \mu\text{M}$), which provided ideal conditions for the formation of free filaments.

5.4 Discussion

We have attempted to propel small particles by single filament elongation using the ActA/VASP complex. We found that the fluorescent intensity along the length of the filaments decreased exponentially from the center of the particle to the end of the filaments, inferring that the polymerization may be occurring at the bead surface. Fluorescent recovery after photobleaching showed that, in the case of one filament, faster recovery rates occurred near the surface of the bead. Other filaments either did not recover or had different intensity trends compared to the initial filament, leaving the photobleaching results inconclusive. If the elongation of all filaments was occurring by insertional polymerization, we would expect that the recovery rate would continue to decrease along the filament length because monomers can only add to the (+)-end of the filament.

Formation of the actin asters potentially have multiple mechanisms at work that are difficult to distinguish from one another through fluorescent microscopy. Single actin filaments are only 7 nm in diameter, making it possible that the free filaments in solution and the background fluorescence of the surface in TIRF may be distorting some of the observed trends. Therefore, insertional polymerization may not be solely responsible for the recovery of fluorescence in our photobleaching experiments. Another explanation of the photobleaching results could be that multiple filaments are lined up with each other, appearing as one, more intense filament in certain regions. New filaments may be dropping to the surface as seen in Figure 5-3 and randomly landing on or around filaments attached to the beads.

In addition, two previously reported studies add to the possible explanations of the formation of actin stars and growth on beads. Brown, et al. observed actin stars on polylysine-coated 1- μm diameter polystyrene beads, which can nucleate polar assembly of filaments. In this case, through myosin subfragment S₁ labeling and observation with an electron microscope, the filaments were shown to be attached to the bead at the (-)-end and therefore, polymerized outward by adding monomers to the filament (+)-end (118). Our results hint that polymerization is occurring at the bead, but we have not conclusively eliminated the possibility of filaments attached to the particles at their (-)-end by some other mechanism. Vignjevic, et al. observed star-like actin structures with bundled filaments, not single-filaments, creating the arms. These stars demonstrated organization of both lamellapodia and filopodia and were dependent on the concentrations of Arp2/3 and capping protein (119). Through fluorescent microscopy, we can not distinguish between single filaments and bundles of a few filaments. Bundling proteins are likely present in the cell extracts, making it possible for bundles of filaments to form.

Diluting the extract seemed to consistently produce beads with single or a few filaments. Insight into the mechanism has recently been gained with the use of electron microscopy (EM) images and TIRF color-change experiments (Sturm, C., J. Phillips, W. Zeile, K. Interliggi, R. Dickinson, and D. Purich, unpublished). Details of filaments, such as the difference between bundles and single filaments are hard to resolve in TIRF, therefore, EM was used. Under specific conditions, a majority of particles attached to filaments only had one filament per particle. Furthermore, by exchanging the actin from a green fluorescent label to a red fluorescent label (or vice-versa) in a flow-cell, the color of the labeled actin added second was always closest to the bead, indicating insertional polymerization (i.e. the (+)-end is attached to the surface of the bead). In most cases, the filaments grew to an average length of 500 nm for 10 seconds, corresponding to an elongation rate of approximately 3 $\mu\text{m}/\text{min}$ (Sturm, C., J. Phillips, W. Zeile, K. Interliggi, R. Dickinson, and D. Purich, unpublished).

The length may be controlled by the presence of capping protein in the extract and could possibly be optimized through varying the concentration of capping protein. For the purpose of control over this system, it may be necessary to use pure component systems which include actin, Arp2/3, ADF, capping protein, VASP, profilin, and α -actinin (115). A pure component system would provide control over protein concentrations, and could help to polymerize filaments for longer time- and length-scales, essentially broadening their application in nanodevices.

When NEM-myosin surfaces were used, visualization was difficult because many actin filaments did not correspond to a bead. Due to the extent of nonspecific actin polymerization, it could not be confirmed that actin filament tails were attached to 50-nm diameter beads when applied to the NEM-myosin surface. Many filaments are most likely spontaneously forming due

to the high concentration of actin, as indicated by the control sample in which no beads were added. Solutions to preventing nonspecific filament formation include the use of profilin or capping proteins.

Insight into the mechanism of actin-based motility suggests that we are making strides toward single filament elongation that can propel small particles end-tracking motors, such as formins and possibly ActA/VASP. Single filaments have the advantage over large rocket tails because they are more flexible, making it easier to manipulate their paths on patterned surfaces. Motile particles would need to be small enough so they do not effect the fluctuations of the attached, elongating filament end. The limitation of these experiments is visualization of both the 50-nm diameter particle and the actin filament in fluorescence at the same time. Biochemical optimization of the system could lead to better visualization and the development of single-filament actuators for use in bionanodevices.

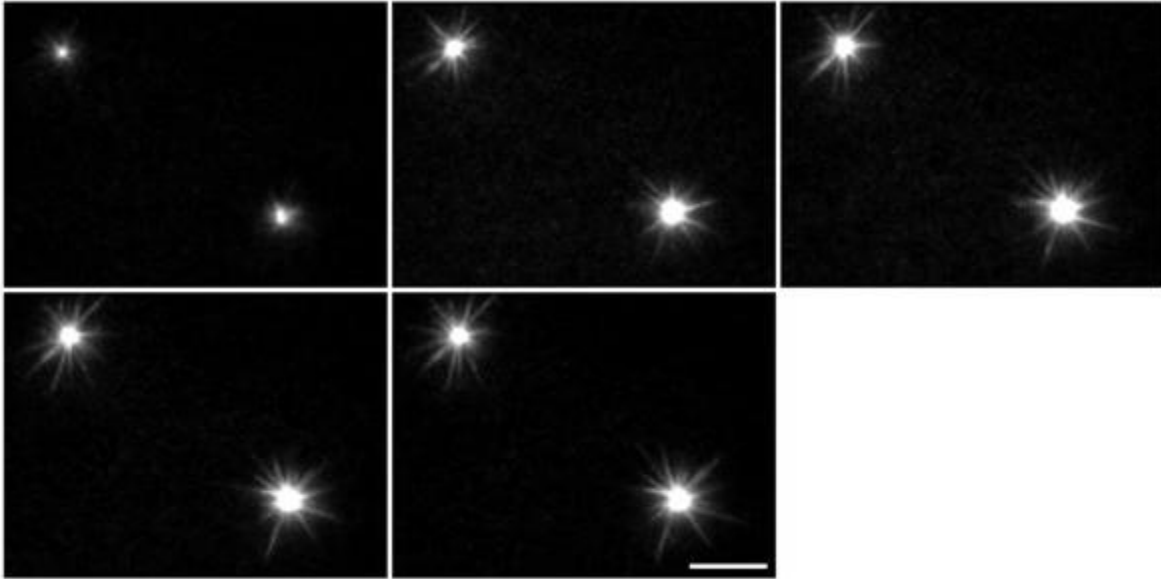


Figure 5-1. Growth of actin filaments/bundles on 50-nm diameter beads. Initially, the 50-nm beads bound to the surface become surrounded by an actin network. The number of filaments and, to some extent, the length of the filaments becomes larger and longer with time. Experiments used full extract strength with an addition of 5 μM of Oregon green-labeled actin (scale bar = 5 μm).

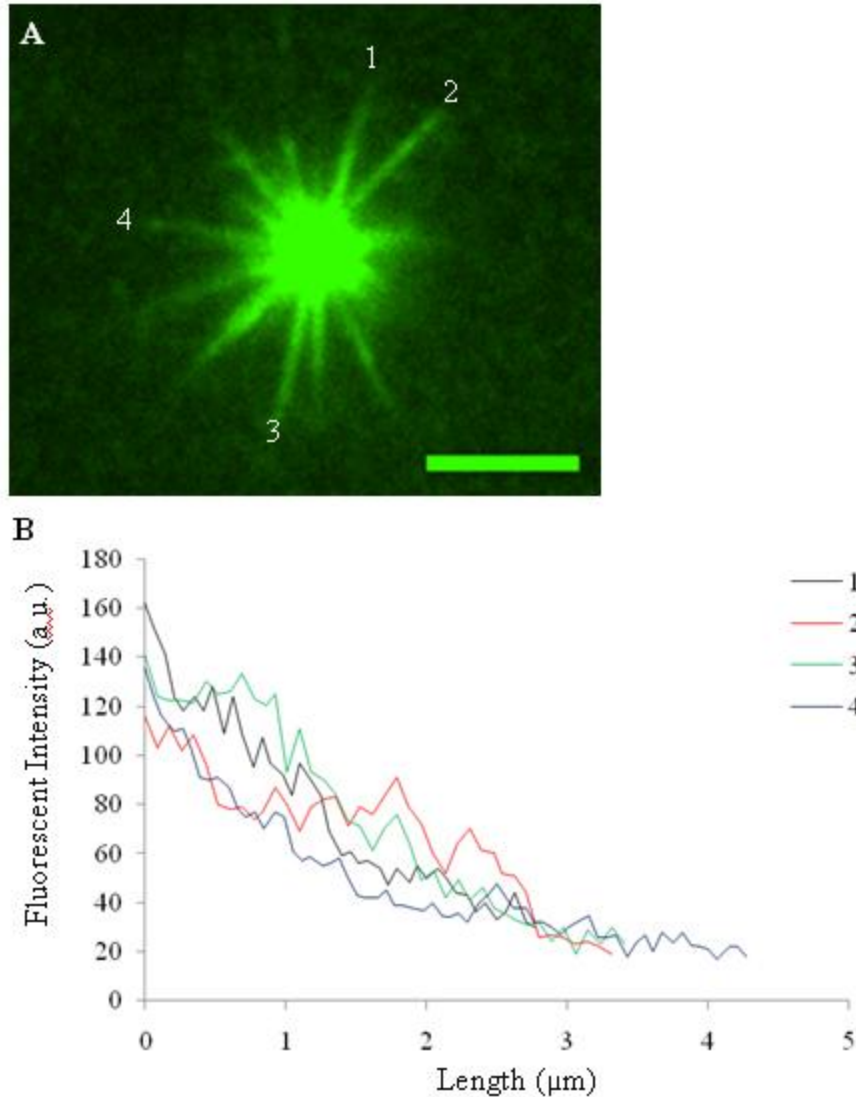


Figure 5-2. Fluorescent intensity of actin filaments/bundles. A) Enlarged image from Figure 5-1 of 50-nm bead bound to the surface. The fluorescent intensity is greatest in the center of the bead (scale bar = 3 μm). B) Fluorescent intensity as a function of length along the filament. The numbers in the legend correspond to the filament labels in A. A line-scan across the filaments show that for all four cases, the intensity decreased for approximately 3 μm of length, where it ultimately levels out to the background intensity. Line-scans began at the beginning of each protrusion at the apparent surface of the bead.

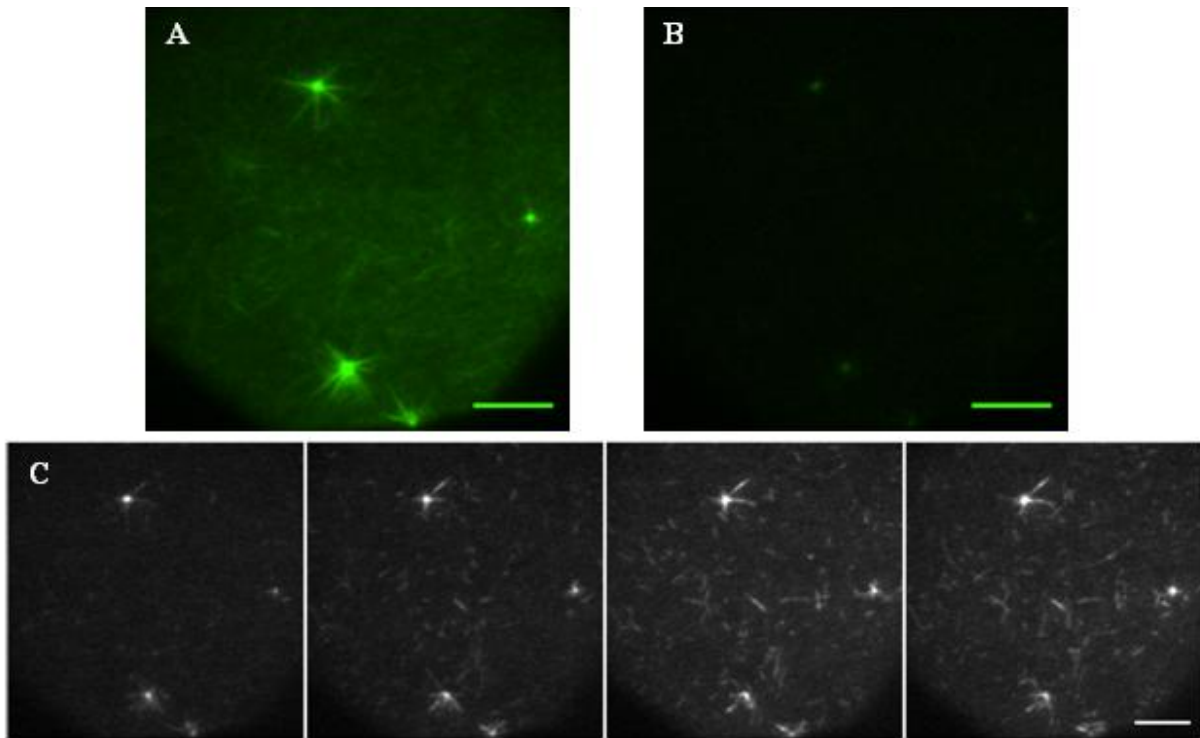


Figure 5-3. Actin asters recovery after photobleaching. A) Initial image of asters of actin on 50-nm diameter beads. B) After photobleaching, only a small fluorescent signal is present at the center of the bead. C) Over time, fluorescence is regained and filaments reappeared on the 50-nm beads. Filaments not associated with a bead also reappeared on the surface. Images were taken 1.5 minutes apart (scale bars = 5 μm).

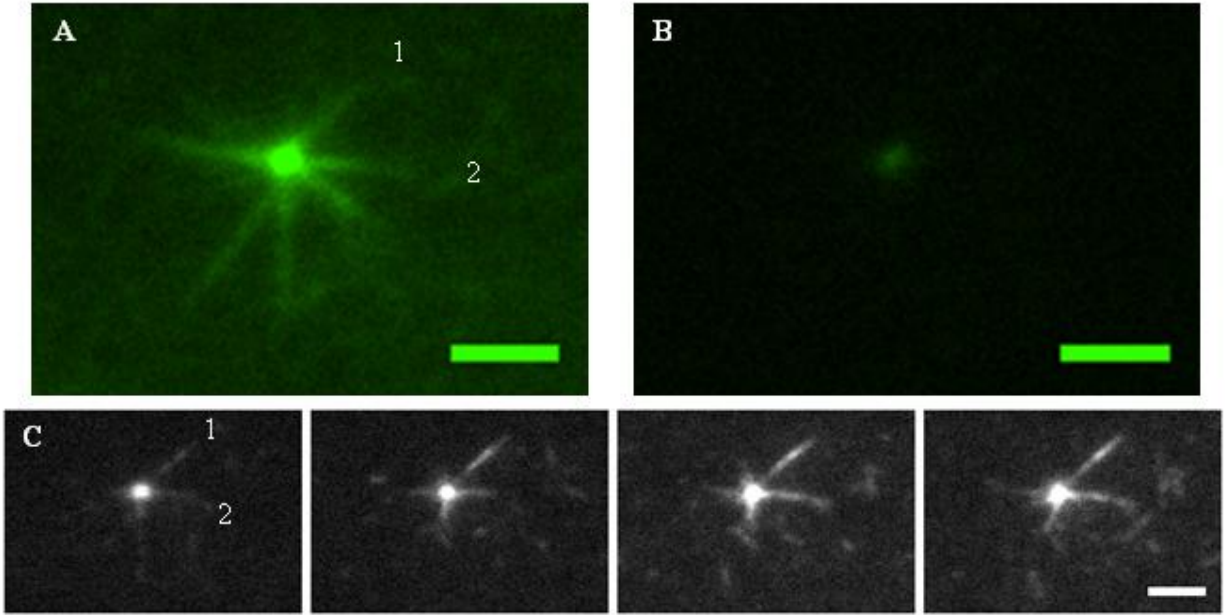


Figure 5-4. Enlarged image of asters reappearing after photobleaching. A) Initial image of asters of actin on 50-nm beads (from Figure 5-3A). B) After photobleaching, only a small fluorescent signal is present at the center of the bead. C) Over time, fluorescence is regained and filaments reappeared on the 50-nm beads. The filaments that appear during the recovery of photobleaching may correspond to initial filaments seen in A. Images were taken 1.5 minutes apart (scale bars = 2 μm).

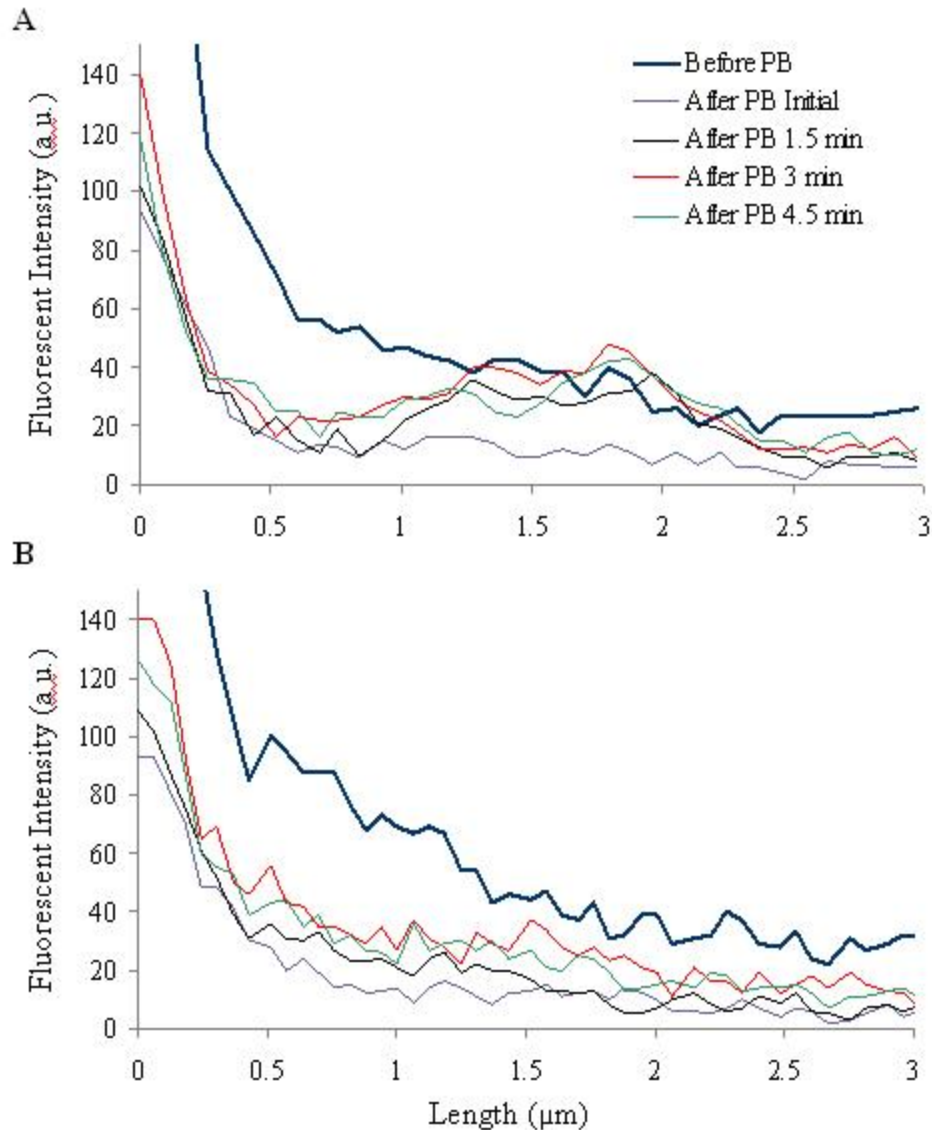


Figure 5-5. Fluorescent intensity of photobleached filaments. A) Fluorescent intensity of filament 1 (Figure 5-4A) as a function of time. At length = 0 μm to 1.5 μm , recovery with respect to length followed the initial trend. At length greater than 1.5 μm , fluorescent intensity exceeded the initial intensity and also increased slightly with increasing length. B) Fluorescent intensity of filament 2 (Figure 5-4B) as a function of time. The intensity of the filament as a function of length followed the initial intensity, before photobleaching.

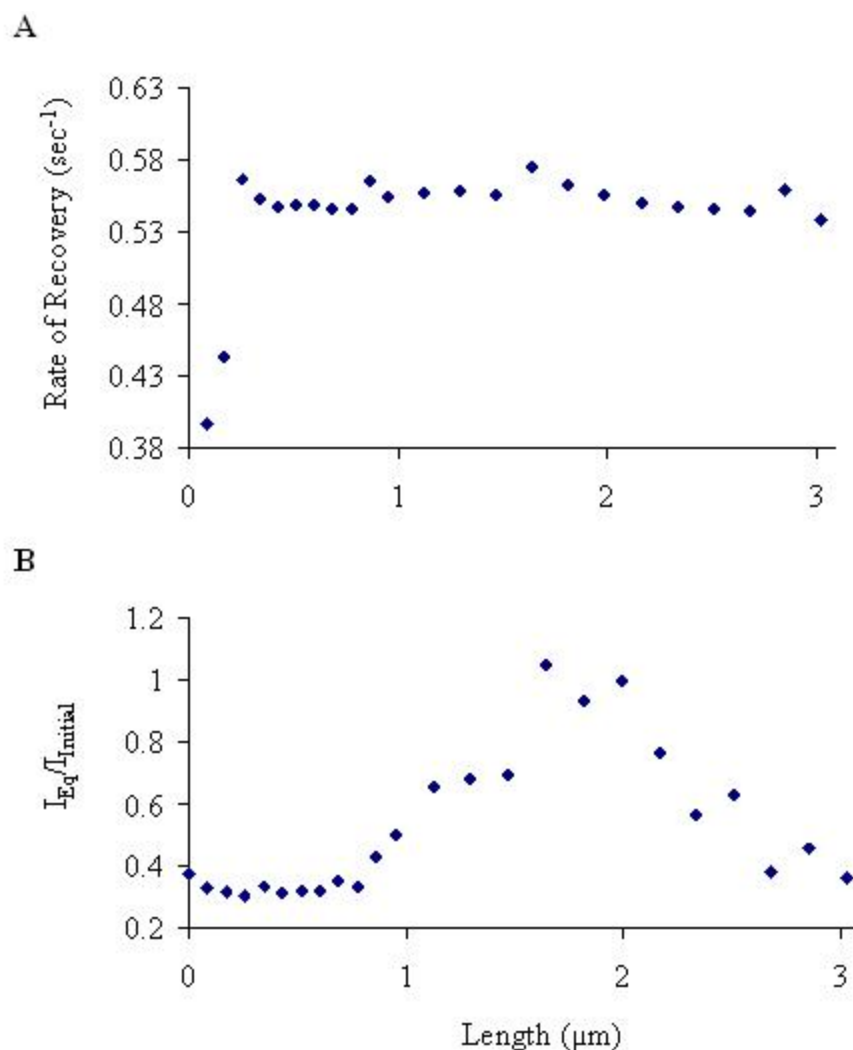


Figure 5-6. Recovery rates and equilibrium intensities of photobleached filaments. A) Fluorescent recovery rate of filament 1 (Figure 5-4A) as a function of position of the filament from the center of the bead. B) The ratio of the calculated equilibrium intensity and the initial intensity before photobleaching of filament 1 (Figure 5-4A). Note that the intensity recovered between 1.5 and 2 μm is greater than 1, corresponding to the region of the filament that was brighter than the initial filament. C) Fluorescent recovery rate of filament 2 (Figure 5-4B). The rates follow an exponential trend as the length away from the bead increases. D) The ratio of the calculated equilibrium intensity and the initial intensity of filament 2 (Figure 5-4B). With the exception of intensities between 0.75 and 1 μm, the equilibrium intensities to initial intensity ratio seem to be within 0.35 and 0.55.

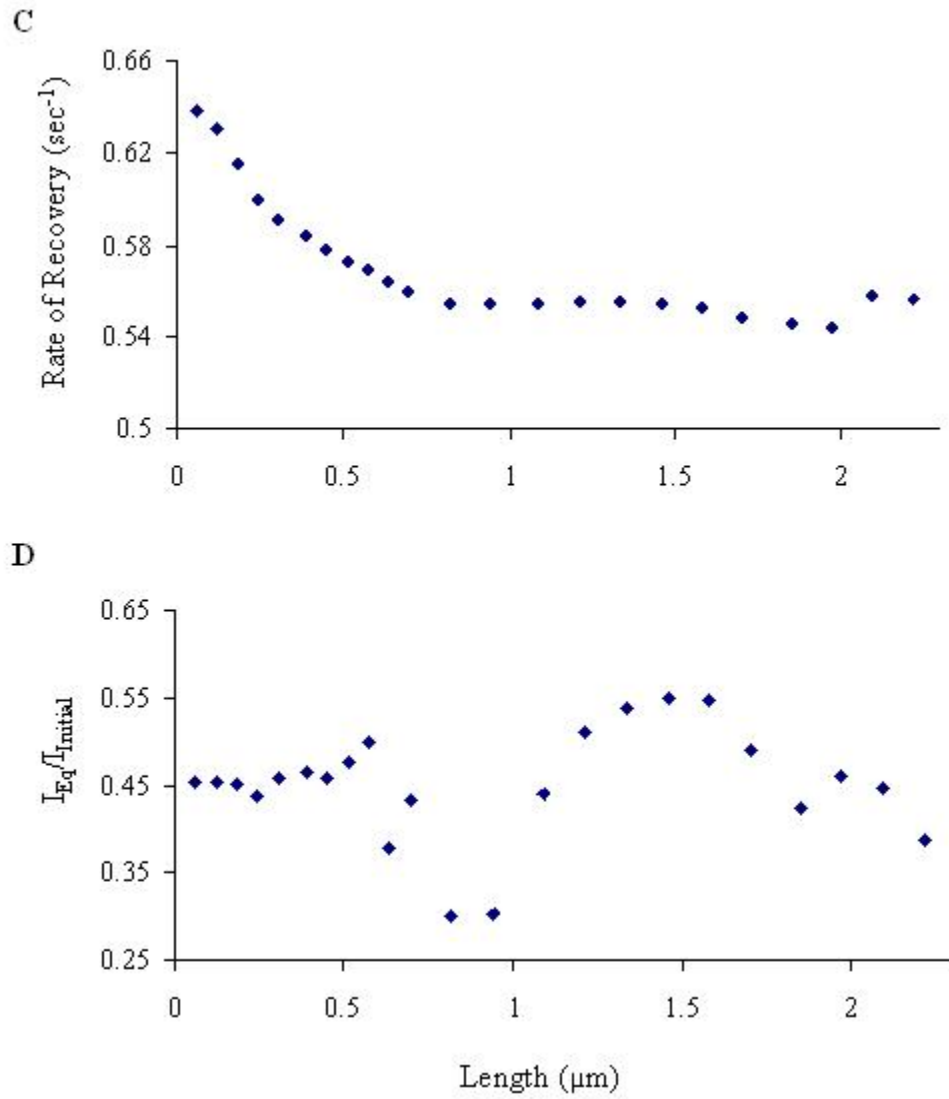


Figure 5-6. Continued

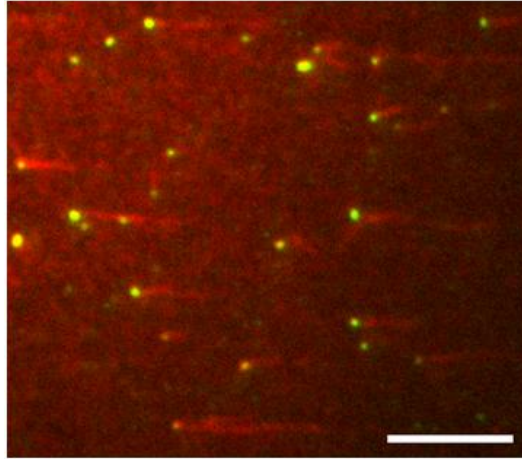


Figure 5-7. 50-nm diameter beads bound to surface with single filaments or bundles attached. Experiments were fixed with gluteraldehyde. Optimization of conditions with the extract (diluted 4:3 in brain extract buffer) led to a reduced number of filaments per bead (scale bar = 5 μm).

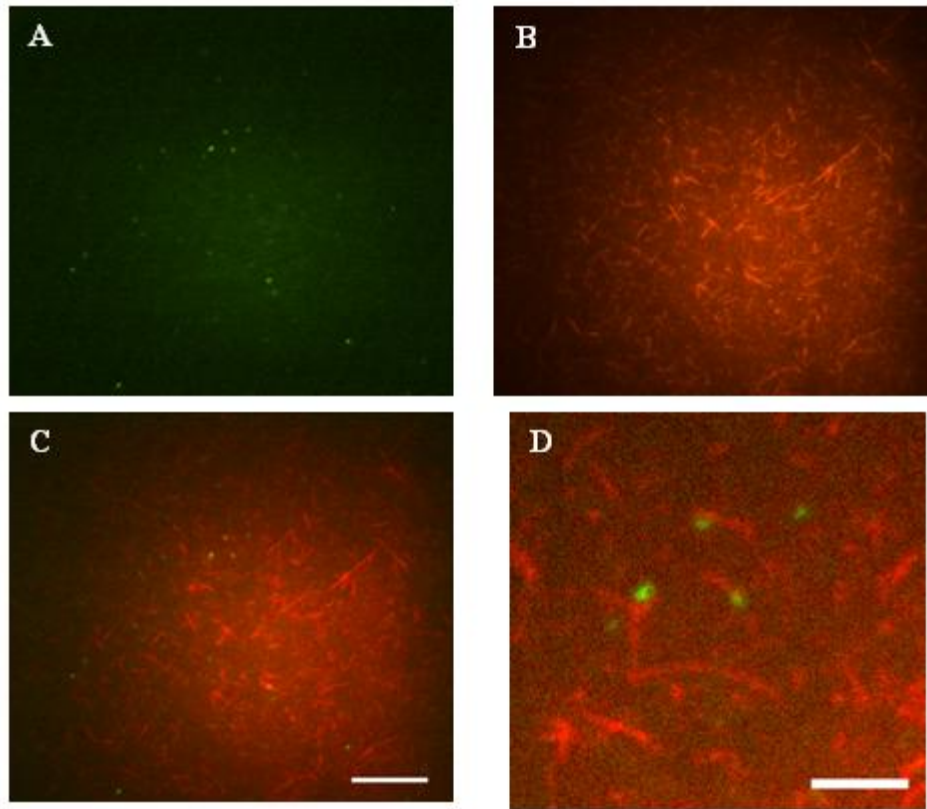


Figure 5-8. 50-nm diameter beads in solution on NEM-myosin surfaces. A) Instantaneous image of fluorescent 50-nm diameter particles, which are constantly moving in and out of the focal plane with time since they are not bound to the surface. B) Rhodamine-labeled actin filaments bound to NEM-myosin surface in same field-of-view. C) Overlay of images A and B. The large number of filaments make it difficult to see any corresponding beads and filaments (scale bar = 10 μm). D) Enlarged image of beads near filament ends. It is unclear if the beads are attached to the filaments or if they are near each other (scale bar = 3 μm).

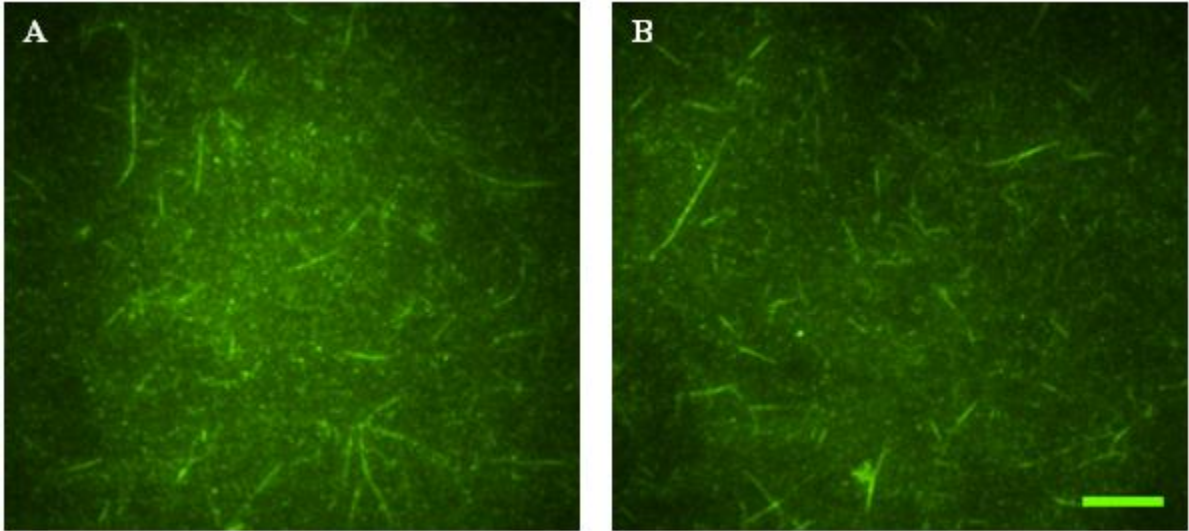


Figure 5-9. Actin motility assay with and without beads on NEM-myosin surfaces. A) Sample containing no beads still produced filaments in solution which bind to the NEM-myosin treated surface. B) Sample containing beads produced and bound approximately the same amount of filaments as a sample with no beads. Both samples have 5 μ M of Oregon green-labeled actin (scale bar = 5 μ m).

CHAPTER 6 SUMMARY AND FUTURE WORK

Applications that involve the exploitation of biomolecular motors are continuously expanding to include a broad spectrum from biosensors for single molecule detection to production of nanoelectromechanical devices. Several methods have already shown promise towards these types of applications, including the gliding of actin filaments or microtubules on myosin- or kinesin-modified surfaces, respectively, and the movement of cargo-carrying myosin or kinesin on immobilized filaments (32). These techniques have yet to explore the potential of actin polymerization and actin-based motility as possibilities for nanoscale transport.

6.1 Single Actin Filaments

The work presented in Chapter 2 demonstrates a technique that aligns polymerizing actin filaments on tracks with the potential for transport of material through cargo-carrying myosin or end-tracking motors bound to filament (+)-ends. Single filaments can potentially attach to end-tracking motors bound to cargo to propel small nanoparticles in an aligned fashion for suitable applications that do not change the thermal fluctuations of the filament. Such particles may include 50-nm diameter particles, antibodies, or quantum dots (2, 4, 14). One important aspect of this assay is that the density of filaments on the surface can be easily controlled. We demonstrated that the filament density decreased on surfaces with the addition of profilin to the actin solution. Higher filament density can be achieved by increasing actin concentration and actin nuclei, potentially with the addition Arp2/3.

Our experiments showed that elongating actin filaments bound to NEM-myosin tracks aligned with the track edge in a manner dependent on the track width and NEM-myosin surface density. We concluded that the alignment of filaments at track boundaries was facilitated by filament thermal fluctuations, based on the following results. Alignment of actin filaments was

inversely proportional to the track width, with the trend leveling off to slightly above random alignment at 10- μm wide tracks. This can be explained by the higher ratio of track edges to track area for the narrower track widths. This increase in ratio causes higher alignment of bound filaments through more frequent interactions with the track edge. Filaments near track edges also demonstrated a bias in alignment, regardless of the track width. This is supported by the conclusion that the probability of an actin filament rebinding once crossing the track edge was dependent on the angle with which the filament crossed the edge. No filaments elongating passed the edge at angles greater than 60° realigned.

These results indicate that microcontact printing NEM-myosin is a viable method for the creation of filament-binding tracks on glass surfaces. One downfall included the diffusion of NEM-myosin molecules from the tracks to the passivated regions, which most likely occurred because the NEM-myosin is adsorbed to the surface, not covalently attached (82). Although this did not seem to affect the final results, some weak binding (to one or a few NEM-myosin molecules only) occurred in the BSA regions of the surface. Another problem was that deformations of the stamp occurred, creating tracks of varying sizes when stamped with the PDMS pattern, as well as some tracks without center regions (120).

The proposed mechanism for the alignment of filaments was supported through simulations, which used the bending energy of the filament to determine filament shapes and behavior (108). The simulations predicted the same effects of track width, myosin concentration and rebinding probability on alignment of filaments as were found experimentally in Chapter 2. Experimental variations that may account for differences between simulations and experiments include variations in surface density and filament-binding activity of the substratum. We also looked at the effect of persistence length on the filaments, finding that the persistence length

does play an important role in the rebinding of the filaments. Because our proposed mechanism requires bending of filaments, the persistence length was expected to play a key role in the filament alignment. The simulations will allow for the future exploration of the effect of various conditions, including different shaped tracks (21).

6.2 Actin-Based Motility

We have reproduced previous methods that use the surface protein, ActA, to induce actin-based motility by forming actin rocket tails that propel *Listeria* and particles *in vitro*. NEM-myosin was used to confine actin rocket tails to glass surfaces and subsequently, contain the path of the motile object near the surface without affecting the velocity. The binding of the actin rocket tails to the surface may be a result of both the surface and the structural features of the rocket tail. Specifically, the rocket tails contain single actin filaments (or small bundles) protruding from the sides of the tail, presumably produced by Arp2/3. The NEM-myosin molecules may bind to these filaments in addition to the exterior filaments in the rocket tail bundle.

The ability of the surface to contain these large structures and reduce fluctuations in their paths is a significant step toward the use of the ActA/VASP complex and end-tracking motors in bionanodevices. Elucidating the mechanism by which binding occurs may help to optimize the system for applications. We attempted to guide particle propulsion further with the use of channels on glass surfaces. The channel design requires features such as width, material used and height to sufficiently prevent the actin rocket tail and attached object from escaping, an important property for transporting particles in devices. Further optimization of the channel design is needed to determine the effectiveness of this system for applications.

We expect that this system can be applied to small particles with single filaments attached. Single filament propulsion is difficult to achieve but extremely useful for bionanodevices. We

have successfully attached ActA-coated beads to surfaces and observed single actin filament growth from these beads, although the work presented here does not conclusively confirm the mechanism by which the filaments are attached. We have shown the difficulties in visualizing and confining single actin filaments to beads in a cell extract on NEM-myosin surfaces. Difficulties include a high density of filaments (not produced by ActA/VASP) and imaging a fluctuating bead, both inhibiting the ability to definitively observe a motile bead attached to an elongating single filament.

6.3 Recommendation for Future Work

6.3.1 Filament-Binding Tracks

The effect of microcontact-printed tracks on the alignment of elongating actin filaments has been characterized in the presented work. Further work should be aimed towards the optimization of the microcontact printing of NEM-myosin. The technique of patterning proteins is complicated in that the activity of the protein, which may be dependent on the structure and position of the protein, must be conserved. Optimization of microcontact printing may provide a way to ensure the position of NEM-myosin is at its most effective, therefore, increasing the binding activity and maintaining the integrity of the pattern (20).

Modifications that could be explored include covalently binding NEM-myosin to an APES-treated surface stamped with gluteraldehyde, ensuring that the myosin heads are exposed. In addition, it may be beneficial to work with heavy-meromyosin, a smaller, still active part of the myosin molecule. The smaller molecule may make it easier to maintain activity and structural integrity, especially if the myosin is covalently bound to a surface (18). Another possibility is to exploit biotin-streptavidin interactions, which are commonly used in microcontact printing and easily attached to proteins (18, 24). These techniques may reduce the diffusion of myosin from the tracks to the passivated regions while making the protein more

effective. Stamp deformation, another problem associated with microcontact printing, may be reduced by optimizing and standardizing the pressure applied to the stamp during the transfer of the proteins.

Other work should be focused towards varying the shape of the filament-binding regions to include curves and corners to determine the effect on the alignment of filaments. In addition, controlling density of the filaments may help to optimize alignment and elongation. We have already determined that profilin lowers the density on the surface. Other proteins that may have an effect on the density or actin network include capping protein, which increases the (+)-end critical concentration to maintain filament lengths, Arp2/3, which increases nucleation and also produces branching for networking, and α -actinin, which cross-links filaments into a continuous network (39). All of these proteins provide advantages to immobilized filament assays by controlling the characteristics of the filaments on the surface, including the potential for lengthening the path for myosin-based transport.

6.3.2 Three-Dimensional Surfaces for Larger Structures

Further investigation into the effect of microcontact printing on actin rocket tails propelling *Listeria* and larger beads *in vitro* is recommended. However, it is unlikely that microcontact printing alone will help to align actin rocket tails, which consist of thousands of filaments. Three-dimensional devices in combination with NEM-myosin surfaces are expected to be more apt to guide particle propulsion. These types of devices, with modified surfaces and topographical features, have been most successful at the guidance of sliding microtubules compared to systems using only one of the two features (16, 105). Further work on the optimization of these devices would likely provide the means to guide elongation of actin rocket tails and their attached particles. The height of the topography, as indicated by our experiments, is an important parameter to be optimized so that the particles do not climb over the walls, but

rather turn at the walls, following the designated path. Undercuts on the top of the channel walls may further ensure that beads remain near the surface (17). In addition, devices may need less exposed glass than those shown in Chapter 4, creating longer channels that span the entire flow-cell. This design should increase the chances that tails bind to surfaces inside channels.

6.3.2 Use of End-Tracking Motors

To obtain more control over the biochemistry involved in the ActA/VASP and end-tracking motor systems, it is necessary to test pure component systems, which have previously been reported to sustain actin-based motility (115). This is particularly important for the single-filament processive motors, which produced more filaments than just those from the ActA-coated beads (due to a high actin concentration). Observation of single-filament elongation is important not only for biodevices, but also for the elucidation of the mechanism by which ActA/VASP produces force. Although this mechanism is still under debate, it remains that the force generated can be advantageous for *in vitro* applications. The Brownian Ratchet model allows for the release of energy of monomer addition (2 kT) (86). The actoclampin mechanism allows for the energy released from ATP hydrolysis to also be used, which would provide 16 kT of accessible energy and a corresponding opposing force of 12 pN (26).

Since formins produce a single, unbranched filament, they provide a simpler system for the use of end-tracking motors, and should be considered for applications in bionanotechnology. In previous reports, the stall force and buckling force for single actin filaments were measured by tethering the filament (+)-ends to formins and attaching another point of the filament to the surface with NEM-myosin. The buckling force of the filaments is proportional to its stiffness and inversely proportional to its length. Therefore, the shortest filament formed (0.75 μm), produced a force of 1.3 pN (94). The forces from formins, ActA/VASP and other end-tracking motors can provide many advantageous to micro- and nano-scale applications. *In vivo*, motors

are efficient and essential to many cellular processes, making them optimal for engineering future bionanodevices.

APPENDIX MATLAB CODE

This program simulates the elongation of actin filaments on patterned, filament-binding surfaces. This program is designed to run multiple filaments in a loop, with one filament elongating per iteration. We first looked at the effect of the filament probability of rebinding when leaving the surface by setting the initial position to $4.99\ \mu\text{m}$ with the track edge located at $5\ \mu\text{m}$. We then varied the number of modes, the binding probability constant, the persistence length, the final total length of the filaments, and the step size, ds . We also looked at the alignment of filaments as a function of track width, where the initial position and initial angle of the filaments were randomly selected. We varied the binding probability constant, the number of modes, and the persistence length. Lengths and parameters were estimated and varied based on experimental values.

```
%This program simulates the elongation of filaments on patterned,  
%filament-binding surfaces  
  
clear all  
  
rand('seed', sum(clock)); %Seeds random number generators in MATLAB  
randn('seed', sum(clock));  
  
%Number of Runs  
ns = 20; %Number of filaments per run  
nt = 15*100 %Maximum length per filament * Number of steps per filament  
nsnt = ns*nt; %Number of maximum possible iterations  
  
%Set Initial Matrices  
x=zeros(1,nsnt); %Initial x, y matrices that determine final filament shape  
y=x;  
xcross=zeros(1,nsnt); %Initial x, y matrices that determine  
ycross=x; %Instantaneous position of elongating filament end  
  
xcross2 = x; %Second to last instantaneous position of filament end  
ycross2 = y;  
xb=zeros(1,nsnt); %Initial x, y matrices at which binding occurs  
yb=xb;  
thend = zeros(1,nsnt); %Initial theta matrix at which binding occurs  
ibin=xb; %Iteration at which binding occurs  
 %mostly for troubleshooting purposes  
Lbind = xb; %Length of filament binding
```

```

ibind=1 %Set initial iteration at which binding occurs
k = 1;

%Determine Length of Filament 1
fillen = (15*rand(1,1))+1 %Select random length less than
                        %15 microns of first filament
nx=round(fillen*100)    %Number of steps for initial filament

%Repeat Loop for Each Filament
for count = 1:ns %For filament 1 through filament ns
dt=1;          %Time increment (seconds)
ds=.01;       %Change in length (microns)

%Generate random number matrices for filament count
rnd = rand(1,nx); % Rnd(x) is used to test the probability of binding
rndn=randn(1,nx);

%Input Variables
nmod = 2 % Number of modes
kp=0.01 % Binding probability scaled to kb^-1 (microns^-1*seconds^-1)
width = 8; % Input track width
space = 20; % Input space between tracks
lam = 10; % Persistence length (microns)
v=0.01; %Elongation rate of filaments (microns/sec)

%Randomize initial starting point and theta, initial binding point
x(k) = 0; %Initial x position is 0
y(k)= (width-.01)*rand-(width/2); % Initial y position is randomly chosen
yb(k)=y(k); %Binding occurs in the initial position
xb(k)= x(k); %xb = x(0) and yb = y(0)
thend(k) = ((90*pi/180))*rand); % Direction of filament at time = 0
L = 0; % Length of unbound region initially
xcross(k) = 0; %Binding occurs in the initial position
ycross(k)= y(k); %xcross(0) = x(0) and ycross(0) = y(0)
xcross2(k) = 0;
ycross2(k)= y(k);
initial_position = y(k); %Print initial position in command window
initial_angle = thend(k); %Print initial angle in command window

%Loop Increases Free Filament Length
for i=k:nx %k = initial iteration of filament
    %Filament 1 starts at k =1, nx = filament length
    rnds=randn(1,nmod); %Random variable selected for each mode
    L=L+v*dt; %Length is increased by ds = v * dt

%Determine if Binding Occurs
    if rnd(i) < kp*dt*L %Check if binding can occur based on
                        %Filament length and probability constant
                        %Equal probability along length
        Lbin = rand(1,1)*L; %Determine random position on
                            %unbound length that binding occurs

        if Lbin > ds %Make sure that Lbin is larger than ds
            %program can not continue (matrix can not be formed)

```

```

s=0:ds:L; %Create matrix of all positions, s, along free filament
sbind = 0:ds:Lbin; %Create matrix of all positions, sbind,
                %along portion of filament that is about to bind

%Calculate maximum amplitudes for each mode
sign = sqrt (2*L./(((0:(nmod-1))+0.5).^2)/lam/pi^2);
modes = sign.*rands; %Calculate actual amplitudes using
                    %random numbers less than 1
theta=0*s; %Create initial matrix theta(s)

for im=1:nmod %Calculate theta for every point, s
    theta = theta + modes(im)*sin((im-1+0.5)*pi*s/L); %theta(1) = 0
                                                    %Sum all modes
end

%Determine x and y points of filament from theta and s
xp=zeros(1, length(s)-1); %Set initial matrices for xp and yp
yp=xp;
for j=2:length(s) %j starting at 2 eliminates the point 0,0 from xp
    %Trapezoid rule used to integrate
    xp(j-1)=(ds/2)*sum((cos(theta(1:(j-1))))+(cos(theta(2:j))));
    yp(j-1)=(ds/2)*sum((sin(theta(1:(j-1))))+(sin(theta(2:j))));
end

%Determine positions with rotation of axis rotated
%with respect to the initial theta (binding position of filament)
%x(1) and y(1) are already set to 0
x(ibind+1:ibind+(length(xp)))=x(ibind)+xp*cos(thend(i))-
yp*sin(thend(i));
y(ibind+1:ibind+(length(xp)))=y(ibind)+xp*sin(thend(i))+yp*cos(thend(i));

%Check if binding (Lbind) occurs within track
%Create wave function to allow for the case of multiple tracks
if cos((y(ibind+length(sbind))-1)/((width+space)/2))*pi)-
cos(((width)/(width+space))*pi)>0

    %Record filament end positions
    ycross(i)=y(ibind + length(xp));
    xcross(i)= x(ibind + length(xp));
    ycross2(i)=y(ibind-1 + length(xp));
    xcross2(i)= x(ibind-1 + length(xp));

    ibind=ibind+length(sbind)-1 %Increase ibind (iteration number
                                %that binding occurs)to new binding position
    ibin(i)=ibind;%Create matrix of iterations for trouble-shooting
    xb(i)=x(ibind); %Place x, y position of binding in xb and yb
    yb(i)=y(ibind);
    Lbind(i)= Lbin; %Record the length of filament that binds
    %Calculate angle of the filament segment at position of binding
    thbind(i)= thend(i)+ theta(length(sbind)-1);
    L= L-Lbin %Update length of unbound region
    thend(i+1) = thbind(i); %Update angle at which binding occurs
                            %Free filament will now undulate around

```

```

else %If filament binding is NOT within track, no binding occurs
    ibind=ibind %Ibind remains the same if no binding occurs
    thend(i+1) = thend(i); %Thend remains the same
        % (binding angle of last binding spot)
    %Record filament end positions
    ycross(i)=y(ibind + length(xp));
    xcross(i)= x(ibind + length(xp));
    ycross2(i)=y(ibind-1 + length(xp));
    xcross2(i)= x(ibind-1 + length(xp));
end

else %If Lbind < ds (not enough binding length)
    %Repeat calculation of filament shape (Lines 80, 83-97)
    s=0:ds:L;
    sign = sqrt (2*L./(((0:(nmod-1))+0.5).^2)/lam/pi^2);
    modes = sign.*rnds;
    theta=0*s;
    for im=1:nmod
        theta = theta + modes(im)*sin((im-1+.5)*pi*s/L);
    end
    %Determine x and y points of filament from theta and s
    xp=zeros(1,length(s)-1);
    yp=xp;
    for j=2:length(s)
        xp(j-1)=(ds/2)*sum((cos(theta(1:(j-1))))+(cos(theta(2:j))));
        yp(j-1)=(ds/2)*sum((sin(theta(1:(j-1))))+(sin(theta(2:j))));
    end
    % Calculate positions with rotation
    x(ibind+1:ibind+(length(xp)))=x(ibind)+xp*cos(thend(i))-
yp*sin(thend(i));

y(ibind+1:ibind+(length(xp)))=y(ibind)+xp*sin(thend(i))+yp*cos(thend(i));

        thend(i+1) = thend(i); %Thend remains the same
    %Record filament end positions
    ycross(i)=y(ibind + length(xp));
    xcross(i)= x(ibind + length(xp));
    ycross2(i)=y(ibind-1 + length(xp));
    xcross2(i)= x(ibind-1 + length(xp));
end

else %If binding probability is less than the random number generator
    %Repeat calculation of filament shape (Lines 80, 83-97)
    s=0:ds:L;
    sign = sqrt (2*L./(((0:(nmod-1))+0.5).^2)/lam/pi^2);
    modes = sign.*rnds;
    theta=0*s;
    for im=1:nmod
        theta = theta + modes(im)*sin((im-1+0.5)*pi*s/L);
    end
    %Determine x and y points of filament from theta and s
    xp=zeros(1,length(s)-1);
    yp=xp;
    for j=2:length(s)
        xp(j-1)=(ds/2)*sum((cos(theta(1:(j-1))))+(cos(theta(2:j))));
        yp(j-1)=(ds/2)*sum((sin(theta(1:(j-1))))+(sin(theta(2:j))));

```

```

        end
        % Calculate positions with rotation
        x(ibind+1:ibind+(length(xp)))=x(ibind)+xp*cos(thend(i))-
yp*sin(thend(i));

y(ibind+1:ibind+(length(xp)))=y(ibind)+xp*sin(thend(i))+yp*cos(thend(i));

        thend(i+1) = thend(i); %Thend remains the same
        %Record filament end positions
        ycross(i)=y(ibind + length(xp));
        xcross(i)= x(ibind + length(xp));
        ycross2(i)=y(ibind-1 + length(xp));
        xcross2(i)= x(ibind-1 + length(xp));
    end
    k = k+1; %Increase k (iteration number for entire simulation

end %End elongation of one filament

ibind = k; %New filament binds at the first iteration of k
fillen = (15*rand(1,1))+1 %Set length of new filament
nx=round(fillen*100) % Set number of iterations for new filament
nx = k + nx; % Increase total number of iterations
end

xprint = x(1:10:nsnt); %Create matrix of final x and y coordinates and theta
yprint = y(1:10:nsnt);
thendi = thend(1:nsnt);

%Create Excel spreadsheets
matrixcross = [thendi', xcross', ycross', xcross2', ycross2', ibin', thbind',
xb', yb', Lbind' ];
matrix2 = [xprint', yprint'];

xlswrite('80ct1_C', matrix2, '6'); %Send final positions of filament
xlswrite('80ct1_PC', matrixcross, '6'); %Send instantaneous positions of
%filaments and binding information

```

LIST OF REFERENCES

1. Howard, J. 2001. *Mechanics of motor proteins and the cytoskeleton*. Sinauer, Sunderland, MA.
2. Bachand, G. D., S. B. Rivera, A. K. Boal, J. Gaudio, J. Liu, and B. C. Bunker. 2004. Assembly and transport of nanocrystal CdSe quantum dot nanocomposites using microtubules and kinesin motor proteins. *Nano Lett.* 4:817-821.
3. Bohm, K. J., R. Stracke, P. Muhlig, and E. Unger. 2001. Motor protein-driven unidirectional transport of micrometer-sized cargoes across isopolar microtubule arrays. *Nanotechnology*. 12:238-244.
4. Mansson, A., M. Sundberg, M. Balaz, R. Bunk, I. A. Nicholls, P. Omling, S. Tagerud, and L. Montelius. 2004. *In vitro* sliding of actin filaments labelled with single quantum dots. *Biochem. Biophys. Res. Commun.* 314:529-534.
5. Muthukrishnan, G., B. M. Hutchins, M. E. Williams, and W. O. Hancock. 2006. Transport of semiconductor nanocrystals by kinesin molecular motors. *Small*. 2:626-630.
6. Suda, H., and A. Ishikawa. 1997. Accelerative sliding of myosin-coated glass-beads under suspended condition from actin paracrystal. *Biochem. Biophys. Res. Commun.* 237:427-431.
7. Suzuki, N., H. Miyata, S. Ishiwata, and K. Kinosita, Jr. 1996. Preparation of bead-tailed actin filaments: Estimation of the torque produced by the sliding force in an *in vitro* motility assay. *Biophys. J.* 70:401-408.
8. Bunk, R., J. Klinth, L. Montelius, I. A. Nicholls, P. Omling, S. Tagerud, and A. Mansson. 2003. Actomyosin motility on nanostructured surfaces. *Biochem. Biophys. Res. Commun.* 301:783-788.
9. Hess, H. 2006. Materials science. Toward devices powered by biomolecular motors. *Science*. 312:860-861.
10. Hess, H., G. D. Bachand, and V. Vogel. 2004. Powering nanodevices with biomolecular motors. *Chemistry*. 10:2110-2116.
11. Hess, H., J. Clemmens, C. Brunner, R. Doot, S. Luna, K. H. Ernst, and V. Vogel. 2005. Molecular self-assembly of "nanowires" and "nanospools" using active transport. *Nano Lett.* 5:629-633.
12. Jia, L., S. G. Moorjani, T. N. Jackson, and W. O. Hancock. 2004. Microscale transport and sorting by kinesin molecular motors. *Biomed. Microdevices*. 6:67-74.
13. Lin, C. T., M. T. Kao, K. Kurabayashi, and E. Meyhofer. 2006. Efficient designs for powering microscale devices with nanoscale biomolecular motors. *Small*. 2:281-287.

14. Ramachandran, S., K. H. Ernst, G. D. Bachand, V. Vogel, and H. Hess. 2006. Selective loading of kinesin-powered molecular shuttles with protein cargo and its application to biosensing. *Small*. 2:330-334.
15. Sundberg, M., R. Bunk, N. Albet-Torres, A. Kvennefors, F. Persson, L. Montelius, I. A. Nicholls, S. Ghatnekar-Nilsson, P. Omling, S. Tagerud, and A. Mansson. 2006. Actin filament guidance on a chip: Toward high-throughput assays and lab-on-a-chip applications. *Langmuir*. 22:7286-7295.
16. Clemmens, J., H. Hess, R. Doot, C. M. Matzke, G. D. Bachand, and V. Vogel. 2004. Motor-protein "Roundabouts": Microtubules moving on kinesin-coated tracks through engineered networks. *Lab Chip*. 4:83-86.
17. Hess, H., C. M. Matzke, R. K. Doot, J. Clemmens, G. D. Bachand, B. C. Bunker, and V. Vogel. 2003. Molecular shuttles operating undercover: A new photolithographic approach for the fabrication of structured surfaces supporting directed motility. *Nano Lett*. 3:1651-1655.
18. Manandhar, P., L. Huang, J. R. Grubich, J. W. Hutchinson, P. B. Chase, and S. Hong. 2005. Highly selective directed assembly of functional actomyosin on Au surfaces. *Langmuir*. 21:3213-3216.
19. Nicolau, D. V., H. Suzuki, S. Mashiko, T. Taguchi, and S. Yoshikawa. 1999. Actin motion on microlithographically functionalized myosin surfaces and tracks. *Biophys. J*. 77:1126-1134.
20. Sundberg, M., M. Balaz, R. Bunk, J. P. Rosengren-Holmberg, L. Montelius, I. A. Nicholls, P. Omling, S. Tagerud, and A. Mansson. 2006. Selective spatial localization of actomyosin motor function by chemical surface patterning. *Langmuir*. 22:7302-7312.
21. Suzuki, H., A. Yamada, K. Oiwa, H. Nakayama, and S. Mashiko. 1997. Control of actin moving trajectory by patterned poly(methylmethacrylate) tracks. *Biophys. J*. 72:1997-2001.
22. Reuther, C., L. Hajdo, R. Tucker, A. A. Kasprzak, and S. Diez. 2006. Biotemplated nanopatterning of planar surfaces with molecular motors. *Nano Lett*. 6:2177-2183.
23. Asokan, S. B., L. Jawerth, R. L. Carroll, R. E. Cheney, S. Washburn, and R. Superfine. 2003. Two-dimensional manipulation and orientation of actin-myosin systems with dielectrophoresis. *Nano Lett*. 3:431-437.
24. Huang, L., P. Manandhar, K. E. Byun, P. B. Chase, and S. Hong. 2006. Selective assembly and alignment of actin filaments with desired polarity on solid substrates. *Langmuir*. 22:8635-8638.
25. Dickinson, R. B., L. Caro, and D. L. Purich. 2004. Force generation by cytoskeletal filament end-tracking proteins. *Biophys. J*. 87:2838-2854.

26. Dickinson, R. B., and D. L. Purich. 2002. Clamped-filament elongation model for actin-based motors. *Biophys. J.* 82:605-617.
27. Romero, S., C. Le Clainche, D. Didry, C. Egile, D. Pantaloni, and M. F. Carlier. 2004. Formin is a processive motor that requires profilin to accelerate actin assembly and associated ATP hydrolysis. *Cell.* 119:419-429.
28. Dabiri, G. A., J. M. Sanger, D. A. Portnoy, and F. S. Southwick. 1990. *Listeria monocytogenes* moves rapidly through the host-cell cytoplasm by inducing directional actin assembly. *Proc. Natl. Acad. Sci. U.S.A.* 87:6068-6072.
29. Tilney, L. G., and D. A. Portnoy. 1989. Actin filaments and the growth, movement, and spread of the intracellular bacterial parasite, *Listeria monocytogenes*. *J. Cell Biol.* 109:1597-1608.
30. Tirnauer, J. S., J. C. Canman, E. D. Salmon, and T. J. Mitchison. 2002. Eb1 targets to kinetochores with attached, polymerizing microtubules. *Mol. Biol. Cell.* 13:4308-4316.
31. Hess, H., and V. Vogel. 2001. Molecular shuttles made from motor proteins: Active transport in non-biological environments. *Reviews in Molecular Biotechnology.* 82:67-85.
32. Bakewell, D. J. G., and D. V. Nicolau. 2007. Protein linear molecular motor-powered nanodevices. *Aust. J. Chem.* 60:314-332.
33. Hess, H., J. Clemmens, J. Howard, and V. Vogel. 2002. Surface imaging by self-propelled nanoscale probes. *Nano Lett.* 2:113-116.
34. Laki, K., W. J. Bowen, and A. Clark. 1950. The polymerization of proteins; adenosine triphosphate and the polymerization of actin. *J. Gen. Physiol.* 33:437-443.
35. Mommaerts, W. F. 1951. Reversible polymerization and ultracentrifugal purification of actin. *J. Biol. Chem.* 188:559-565.
36. Otterbein, L. R., P. Graceffa, and R. Dominguez. 2001. The crystal structure of uncomplexed actin in the ADP state. *Science.* 293:708-711.
37. Straub, F. B., and G. Feurer. 1950. Adenosinetriphosphate the functional group of actin. *Biochim. Biophys. Acta.* 4:455-470.
38. Straub, F. B. 1942. Actin. *Stud. Inst. Med. Chem. Univ. Szeged.* 2:1-15.
39. Southwick, F. S., and D. L. Purich. 2000. Actin filaments: Self-assembly and regulatory interactions. In *Cellular Microbiology*. P. Cossart, P. Boquet, S. Normark, and R. Rappuoli, editors. ASM Press, Washington, D.C. 153-170.
40. Schafer, D. A., M. D. Welch, L. M. Machesky, P. C. Bridgman, S. M. Meyer, and J. A. Cooper. 1998. Visualization and molecular analysis of actin assembly in living cells. *J. Cell Biol.* 143:1919-1930.

41. Wear, M. A., D. A. Schafer, and J. A. Cooper. 2000. Actin dynamics: Assembly and disassembly of actin networks. *Curr. Biol.* 10:891-895.
42. Kelleher, J. F., S. J. Atkinson, and T. D. Pollard. 1995. Sequences, structural models, and cellular localization of the actin-related proteins arp2 and arp3 from *acanthamoeba*. *J. Cell Biol.* 131:385-397.
43. Alberts, B., A. Johnson, J. Lewis, M. Raff, K. Roberts, and P. Walter. 2002. *Molecular biology of the cell*. Garland Science, New York.
44. Kirschner, M. W. 1980. Implications of treadmilling for the stability and polarity of actin and tubulin polymers *in vivo*. *J. Cell Biol.* 86:330-334.
45. Neuhaus, J. M., M. Wanger, T. Keiser, and A. Wegner. 1983. Treadmilling of actin. *J. Muscle Res. Cell. Motil.* 4:507-527.
46. Wegner, A. 1976. Head to tail polymerization of actin. *J. Mol. Biol.* 108:139-150.
47. Kaufmann, S., J. Kas, W. H. Goldmann, E. Sackmann, and G. Isenberg. 1992. Talin anchors and nucleates actin filaments at lipid membranes. A direct demonstration. *FEBS Lett.* 314:203-205.
48. Isambert, H., P. Venier, A. C. Maggs, A. Fattoum, R. Kassab, D. Pantaloni, and M. F. Carlier. 1995. Flexibility of actin filaments derived from thermal fluctuations. Effect of bound nucleotide phalloidin and muscle regulatory proteins. *J. Biol. Chem.* 270:11437-11444.
49. Kas, J., H. Strey, J. X. Tang, D. Finger, R. Ezzell, E. Sackmann, and P. A. Janmey. 1996. F-actin, a model polymer for semiflexible chains in dilute, semidilute, and liquid crystalline solutions. *Biophys. J.* 70:609-625.
50. Sugimoto, Y., M. Tokunaga, Y. Takezawa, M. Ikebe, and K. Wakabayashi. 1995. Conformational changes of the myosin heads during hydrolysis of ATP as analyzed by x-ray solution scattering. *Biophys. J.* 68:29S-33S; discussion 33S-34S.
51. Lynn, R. W., and E. W. Taylor. 1971. Mechanism of adenosine triphosphate hydrolysis by actomyosin. *Biochemistry.* 10:4617-4624.
52. Rayment, I., H. M. Holden, M. Whittaker, C. B. Yohn, M. Lorenz, K. C. Holmes, and R. A. Milligan. 1993. Structure of the actin-myosin complex and its implications for muscle contraction. *Science.* 261:58-65.
53. Stossel, T. P. 1993. On the crawling of animal cells. *Science.* 260:1086-1094.
54. Cassimeris, L., D. Safer, V. T. Nachmias, and S. H. Zigmond. 1992. Thymosin beta 4 sequesters the majority of G-actin in resting human polymorphonuclear leukocytes. *J. Cell Biol.* 119:1261-1270.

55. Southwick, F. S., and C. L. Young. 1990. The actin released from profilin-actin complexes is insufficient to account for the increase in f-actin in chemoattractant-stimulated polymorphonuclear leukocytes. *J. Cell Biol.* 110:1965-1973.
56. Kang, F., D. L. Purich, and F. S. Southwick. 1999. Profilin promotes barbed-end actin filament assembly without lowering the critical concentration. *J. Biol. Chem.* 274:36963-36972.
57. Paavilainen, V. O., E. Bertling, S. Falck, and P. Lappalainen. 2004. Regulation of cytoskeletal dynamics by actin-monomer-binding proteins. *Trends Cell Biol.* 14:386-394.
58. Mullins, R. D., J. A. Heuser, and T. D. Pollard. 1998. The interaction of arp2/3 complex with actin: Nucleation, high affinity pointed end capping, and formation of branching networks of filaments. *Proc. Natl. Acad. Sci. U.S.A.* 95:6181-6186.
59. McGough, A. 1998. F-actin-binding proteins. *Curr. Opin. Struct. Biol.* 8:166-176.
60. Carrier, M. F., V. Laurent, J. Santolini, R. Melki, D. Didry, G. X. Xia, Y. Hong, N. H. Chua, and D. Pantaloni. 1997. Actin depolymerizing factor (adf/cofilin) enhances the rate of filament turnover: Implication in actin-based motility. *J. Cell Biol.* 136:1307-1322.
61. Casella, J. F., D. J. Maack, and S. Lin. 1986. Purification and initial characterization of a protein from skeletal muscle that caps the barbed ends of actin filaments. *J. Biol. Chem.* 261:10915-10921.
62. Cooper, J. A., and T. D. Pollard. 1982. Methods to measure actin polymerization. *Methods Enzymol.* 85:182-211.
63. Blanchoin, L., K. J. Amann, H. N. Higgs, J. B. Marchand, D. A. Kaiser, and T. D. Pollard. 2000. Direct observation of dendritic actin filament networks nucleated by arp2/3 complex and wasp/scar proteins. *Nature.* 404:1007-1011.
64. Pollard, T. D., and M. S. Mooseker. 1981. Direct measurement of actin polymerization rate constants by electron microscopy of actin filaments nucleated by isolated microvillus cores. *J. Cell Biol.* 88:654-659.
65. Burlacu, S., P. A. Janmey, and J. Borejdo. 1992. Distribution of actin filament lengths measured by fluorescence microscopy. *Am. J. Physiol.* 262:C569-577.
66. Xu, J., J. F. Casella, and T. D. Pollard. 1999. Effect of capping protein, capz, on the length of actin filaments and mechanical properties of actin filament networks. *Cell Motil. Cytoskeleton.* 42:73-81.
67. Yanagida, T., M. Nakase, K. Nishiyama, and F. Oosawa. 1984. Direct observation of motion of single F-actin filaments in the presence of myosin. *Nature.* 307:58-60.
68. Axelrod, D. 2001. Total internal reflection fluorescence microscopy in cell biology. *Traffic.* 2:764-774.

69. Amann, K. J., and T. D. Pollard. 2001. Direct real-time observation of actin filament branching mediated by arp2/3 complex using total internal reflection fluorescence microscopy. *Proc. Natl. Acad. Sci. U.S.A.* 98:15009-15013.
70. Kuhn, J. R., and T. D. Pollard. 2005. Real-time measurements of actin filament polymerization by total internal reflection fluorescence microscopy. *Biophys. J.* 88:1387-1402.
71. Atkinson, M. A., P. K. Lambooy, and E. D. Korn. 1989. Cooperative dependence of the actin-activated Mg²⁺-ATPase activity of *Acanthamoeba* myosin II on the extent of filament phosphorylation. *J. Biol. Chem.* 264:4127-4132.
72. Pemrick, S., and A. Weber. 1976. Mechanism of inhibition of relaxation by n-ethylmaleimide treatment of myosin. *Biochemistry.* 15:5193-5198.
73. Amann, K. J., and T. D. Pollard. 2001. The arp2/3 complex nucleates actin filament branches from the sides of pre-existing filaments. *Nat. Cell Biol.* 3:306-310.
74. Xia, Y., and G. M. Whitesides. 1998. Soft lithography. *Annual Review of Materials Science.* 28:153-184.
75. Kumar, A., and G. M. Whitesides. 1993. Features of gold having micrometer to centimeter dimensions can be formed through a combination of stamping with an elastomeric stamp and an alkanethiol "ink" followed by chemical etching. *Appl. Phys. Lett.* 63:2002-2004.
76. Kind, H., M. Geissler, H. Schmid, B. Michel, K. Kern, and E. Delamarche. 2000. Patterned electroless deposition of copper by microcontact printing palladium(ii) complexes on titanium-covered surfaces. *Langmuir.* 16:6367-6373.
77. Nikitov, S. A., L. Presmanes, P. Tailhades, and D. E. Balabanov. 2002. Magnetic duplication and contact printing method. *Journal of Magnetism and Magnetic Materials.* 241:124-130.
78. Presmanes, L., and P. Tailhades. 2002. Field assisted magnetic contact printing with soft magnetic patterned thin films. *Journal of Magnetism and Magnetic Materials.* 242-245:499-504.
79. Renault, J. P., A. Bernard, A. Bietsch, B. Michel, H. R. Bosshard, E. Delamarche, M. Krieter, B. Hecht, and U. P. Wild. 2003. Fabricating arrays of single protein molecules on glass using microcontact printing. *J. Phys. Chem.* 107:703-711.
80. Xu, L., L. Robert, Q. Ouyang, F. Taddei, Y. Chen, A. B. Lindner, and D. Baigl. 2007. Microcontact printing of living bacteria arrays with cellular resolution. *Nano Lett.* 7:2068-2072.
81. Rozkiewicz, D. I., Y. Kraan, M. W. Werten, F. A. de Wolf, V. Subramaniam, B. J. Ravoo, and D. N. Reinhoudt. 2006. Covalent microcontact printing of proteins for cell patterning. *Chemistry.* 12:6290-6297.

82. Quist, A. P., E. Pavlovic, and S. Oscarsson. 2005. Recent advances in microcontact printing. *Anal. Bioanal. Chem.* 381:591-600.
83. Theriot, J. A., J. Rosenblatt, D. A. Portnoy, P. J. Goldschmidt-Clermont, and T. J. Mitchison. 1994. Involvement of profilin in the actin-based motility of *L. monocytogenes* in cells and in cell-free extracts. *Cell.* 76:505-517.
84. Zeile, W. L., D. L. Purich, and F. S. Southwick. 1996. Recognition of two classes of oligoproline sequences in profilin-mediated acceleration of actin-based *Shigella* motility. *J. Cell Biol.* 133:49-59.
85. Briehner, W. M., M. Coughlin, and T. J. Mitchison. 2004. Fascin-mediated propulsion of *Listeria monocytogenes* independent of frequent nucleation by the arp2/3 complex. *J. Cell Biol.* 165:233-242.
86. Mogilner, A., and G. Oster. 2003. Force generation by actin polymerization II: The elastic ratchet and tethered filaments. *Biophys. J.* 84:1591-1605.
87. Kocks, C., E. Gouin, M. Tabouret, P. Berche, H. Ohayon, and P. Cossart. 1992. *L. monocytogenes*-induced actin assembly requires the ActA gene product, a surface protein. *Cell.* 68:521-531.
88. Cameron, L. A., P. A. Giardini, F. S. Soo, and J. A. Theriot. 2000. Secrets of actin-based motility revealed by a bacterial pathogen. *Nat. Rev. Mol. Cell Biol.* 1:110-119.
89. Cameron, L. A., T. M. Svitkina, D. Vignjevic, J. A. Theriot, and G. G. Borisy. 2001. Dendritic organization of actin comet tails. *Curr. Biol.* 11:130-135.
90. Cameron, L. A., M. J. Footer, A. van Oudenaarden, and J. A. Theriot. 1999. Motility of ActA protein-coated microspheres driven by actin polymerization. *Proc. Natl. Acad. Sci. U.S.A.* 96:4908-4913.
91. Kuo, S. C., and J. L. McGrath. 2000. Steps and fluctuations of *Listeria monocytogenes* during actin-based motility. *Nature.* 407:1026-1029.
92. Upadhyaya, A., J. R. Chabot, A. Andreeva, A. Samadani, and A. van Oudenaarden. 2003. Probing polymerization forces by using actin-propelled lipid vesicles. *Proc. Natl. Acad. Sci. U.S.A.* 100:4521-4526.
93. Chang, F., D. Drubin, and P. Nurse. 1997. Cdc12p, a protein required for cytokinesis in fission yeast, is a component of the cell division ring and interacts with profilin. *J. Cell Biol.* 137:169-182.
94. Kovar, D. R., and T. D. Pollard. 2004. Insertional assembly of actin filament barbed ends in association with formins produces piconewton forces. *Proc. Natl. Acad. Sci. U.S.A.* 101:14725-14730.

95. Pruyne, D., M. Evangelista, C. Yang, E. Bi, S. Zigmund, A. Bretscher, and C. Boone. 2002. Role of formins in actin assembly: Nucleation and barbed-end association. *Science*. 297:612-615.
96. Zigmund, S. H., M. Evangelista, C. Boone, C. Yang, A. C. Dar, F. Sicheri, J. Forkey, and M. Pring. 2003. Formin leaky cap allows elongation in the presence of tight capping proteins. *Curr. Biol.* 13:1820-1823.
97. Mogilner, A., and G. Oster. 1996. Cell motility driven by actin polymerization. *Biophys. J.* 71:3030-3045.
98. Peskin, C. S., G. M. Odell, and G. F. Oster. 1993. Cellular motions and thermal fluctuations: The Brownian ratchet. *Biophys. J.* 65:316-324.
99. Hill, T. L. 1981. Microfilament or microtubule assembly or disassembly against a force. *Proc. Natl. Acad. Sci. U.S.A.* 78:5613-5617.
100. Abraham, V. C., V. Krishnamurthi, D. L. Taylor, and F. Lanni. 1999. The actin-based nanomachine at the leading edge of migrating cells. *Biophys. J.* 77:1721-1732.
101. Kovar, D. R., J. Q. Wu, and T. D. Pollard. 2005. Profilin-mediated competition between capping protein and formin cdc12p during cytokinesis in fission yeast. *Mol. Biol. Cell.* 16:2313-2324.
102. Romero, S., D. Didry, E. Larquet, N. Boisset, D. Pantaloni, and M. F. Carlier. 2007. How ATP hydrolysis controls filament assembly from profilin-actin: Implication for formin processivity. *J. Biol. Chem.* 282:8435-8445.
103. Kwiatkowski, A. V., F. B. Gertler, and J. J. Loureiro. 2003. Function and regulation of Ena/VASP proteins. *Trends Cell Biol.* 13:386-392.
104. Geese, M., K. Schluter, M. Rothkegel, B. M. Jockusch, J. Wehland, and A. S. Sechi. 2000. Accumulation of profilin II at the surface of *Listeria* is concomitant with the onset of motility and correlates with bacterial speed. *J. Cell Sci.* 113 (Pt 8):1415-1426.
105. Clemmens, J., H. Hess, R. Lipscomb, Y. Hanein, K. F. Bohringer, C. M. Matzke, G. D. Bachand, B. C. Bunker, and V. Vogel. 2003. Mechanisms of microtubule guiding on microfabricated kinesin-coated surfaces: Chemical and topographic surface patterns. *Langmuir.* 19:10967-10974.
106. Pardee, J. D., and J. A. Spudich. 1982. Purification of muscle actin. *Methods Enzymol.* 85 Pt B:164-181.
107. Bernard, A., E. Delamarche, H. Schmid, B. Michel, H. R. Bosshard, and H. Biebuyk. 1998. Printing patterns of proteins. *Langmuir.* 14:2225-2229.
108. Landau, L. D., and E. M. Lifshitz. 1986. Theory of elasticity. Reed Educational and Professional Publishing Ltd., New York.

109. Ostap, E. M., T. Yanagida, and D. D. Thomas. 1992. Orientational distribution of spin-labeled actin oriented by flow. *Biophys. J.* 63:966-975.
110. Lee, C. S., S. H. Lee, S. S. Park, Y. K. Kim, and B. G. Kim. 2003. Protein patterning on silicon-based surface using background hydrophobic thin film. *Biosens. Bioelectron.* 18:437-444.
111. Welch, M. D., J. Rosenblatt, J. Skoble, D. A. Portnoy, and T. J. Mitchison. 1998. Interaction of human arp2/3 complex and the *Listeria monocytogenes* ActA protein in actin filament nucleation. *Science.* 281:105-108.
112. Plastino, J., I. Lelidis, J. Prost, and C. Sykes. 2004. The effect of diffusion, depolymerization and nucleation promoting factors on actin gel growth. *Eur. Biophys. J.* 33:310-320.
113. Zeile, W. L., F. Zhang, R. B. Dickinson, and D. L. Purich. 2005. *Listeria's* right-handed helical rocket-tail trajectories: Mechanistic implications for force generation in actin-based motility. *Cell Motil. Cytoskeleton.* 60:121-128.
114. Welch, M. D., A. Iwamatsu, and T. J. Mitchison. 1997. Actin polymerization is induced by arp2/3 protein complex at the surface of *Listeria monocytogenes*. *Nature.* 385:265-269.
115. Loisel, T. P., R. Boujemaa, D. Pantaloni, and M. F. Carlier. 1999. Reconstitution of actin-based motility of *Listeria* and *Shigella* using pure proteins. *Nature.* 401:613-616.
116. Cameron, L. A., J. R. Robbins, M. J. Footer, and J. A. Theriot. 2004. Biophysical parameters influence actin-based movement, trajectory, and initiation in a cell-free system. *Mol. Biol. Cell.* 15:2312-2323.
117. Oudenaarden, A., and J. A. Theriot. 1999. Cooperative symmetry-breaking by actin polymerization in a model for cell motility. *Nat. Cell Biol.* 1:493-499.
118. Brown, S. S., and J. A. Spudich. 1979. Nucleation of polar actin filament assembly by a positively charged surface. *J. Cell Biol.* 80:499-504.
119. Vignjevic, D., D. Yarar, M. D. Welch, J. Peloquin, T. Svitkina, and G. G. Borisy. 2003. Formation of filopodia-like bundles in vitro from a dendritic network. *J. Cell Biol.* 160:951-962.
120. Rogers, J. A., K. E. Paul, and G. M. Whitesides. 1998. Quantifying distortions in soft lithography. *Journal of Vacuum Science and Technology B.* 16:88-97.

BIOGRAPHICAL SKETCH

Kimberly A. Interliggi was born and raised in Canton, Ohio. She graduated from Jackson High School in 2000 and attended Ohio University on a full-tuition scholarship. She received her BSChE (magna cum laude) in June 2003. In August 2003, she enrolled in the PhD program in the Department of Chemical Engineering at the University of Florida. She began working for Dr. Richard Dickinson in January 2004 and received her doctorate in December 2007.